

POLITECNICO DI TORINO

MASTER OF SCIENCE IN ELECTRICAL  
ENGINEERING

MASTER'S DEGREE THESIS

**Design and analysis of different rotor  
configurations for wound field  
synchronous machines**



*Candidate:*  
Federica GRAFFEO

*Academic Supervisors:*  
Ing. Silvio VASHETTO  
Prof. Andrea CAVAGNINO  
Prof. Edson Da Costa BORTONI  
Ing. Marco COSSALE

A.Y. 2019/2020

*"Our greatest weakness lies in giving up. The most certain  
way to succeed is always to try just one more time"*  
*Thomas Edison*

# Contents

<b>Abstract</b>	<b>iii</b>
<b>List of Figures</b>	<b>iv</b>
<b>List of Tables</b>	<b>vii</b>
<b>1 Introduction</b>	<b>1</b>
1.1 State of the Art	1
1.2 Wound Field Synchronous Motors	5
1.2.1 Salient Pole Rotor vs Cylindrical Rotor	5
1.2.2 How to bring current to the rotor	7
1.3 Thesis Goal	10
<b>2 Salient Pole Machine</b>	<b>11</b>
2.1 Available Data of the Salient Pole Machine	11
2.1.1 Data extrapolated from the PhD thesis	12
2.1.2 Data provided by the company	16
2.2 Analytical computation of the No-Load Characteristic	19
2.3 FEM Model	26
2.3.1 The stator	26
2.3.2 The air gap	27
2.3.3 The rotor	28
2.3.4 The circuit	32
2.4 No-Load Characteristic	33
2.5 Simulations at Load	35
2.6 Main Parameters Computation	41
2.6.1 Analytical Computation	41
2.6.2 Computation by Simulation of the Inductances	47
2.7 Losses and Efficiencies	49
<b>3 Cylindrical Machine</b>	<b>56</b>
3.1 Design Procedure	56
3.1.1 Check of Mechanical Stress	62
3.2 FEM Model	65
3.3 No-Load Characteristic	66
3.4 Simulations at Load	68
3.5 Main Parameters Computation	70
3.5.1 Analytical Computation	70
3.5.2 Computation by Simulation of the Inductances	71

3.6	Losses and Efficiencies	74
<b>4</b>	<b>Comparison</b>	<b>77</b>
4.1	Comparison at No-Load	77
4.2	Parameters Comparison	81
4.3	Comparison at Load	82
4.3.1	Cross Saturation Effect	83
4.3.2	Torques Comparison	86
4.4	Losses and Efficiencies Comparison	89
<b>5</b>	<b>Conclusions and Future Work</b>	<b>91</b>
5.1	Conclusions	91
5.2	Future Work	92
	<b>Bibliography</b>	<b>94</b>

# Abstract

Lately, the wound rotor synchronous motor (WRSM) has been receiving an increasing interest as suitable alternative to the dominant technologies in electric vehicle (EV) applications. The WRSM does not have any permanent magnet inside. Its rotor hosts a winding for the injection of a continuous current, allowing to create the excitation field. It can generate high torque at low speed by overloading both the stator and the rotor, avoiding an unnecessary oversizing of the inverter. Furthermore, WRSMs usually allow achieving extended constant power speed ranges compared to other synchronous machine structures. Wound rotor synchronous machines come in two possible configurations depending on the rotor construction: Salient Pole (SP) motor and Cylindrical Rotor (CR) motor. In high speed applications, the conductors of the excitation winding in WRSM are subjected to large centrifugal forces. These cause dangerous mechanical vibrations that could lead to the deterioration of the insulation and therefore undesired interturn short circuit faults. As some automotive suppliers have faced this problem when employing SP motors, the CR solution is currently under investigation as a possible way to overcome the issue. Indeed, the CR has historically been employed as alternator in high speed applications where it is convenient to distribute the winding over the rotor surface to guarantee a better mechanical resistance to centrifugal forces. Moreover, the better enclosure of the rotor conductors allows to reduce their mechanical vibration. Hence, the CR could offer some advantages over its counterpart SP. In this thesis, an already existing SP motor prototype for electric traction has been used as the baseline of the study. A preliminary sizing of the CR machine has been accomplished, by keeping the same stator of the SP machine and respecting electromagnetic constraints. Finally, a comparison in terms of performances of the SP motor and the CR motor has been carried out by means of finite element analysis (FEA). Results have shown that the SP motor seems to achieve slightly better performances, especially for low values of the excitation current. This is due to the lack of anisotropy and a more marked cross effect saturation of the CR with respect to the SP. On the contrary, as the excitation current increases the gap tends to be less pronounced. Considering that the design of the cylindrical rotor is not optimized, better performances with respect to the SP might be accomplished with further improvements. Moreover, a bigger torque ripple can be found in the CR and to eventually skew the machine could be part of future works. In conclusion, if the CR represents an undeniable beneficial choice from a mechanical point of view, deeper investigation is needed to make it electromagnetically competitive with its counterpart SP. It is worthy to remind that the design of the cylindrical rotor machine presented in this work is not optimized. Hence, there may still be additional room for improvement.

# List of Figures

1.1	Ideal Torque-Speed characteristic for electric vehicles. . . . .	2
1.2	Salient Pole Machine (a) and Cylindrical Rotor Machine (b). . . . .	6
1.3	Rotating transformer scheme. . . . .	8
2.1	System architecture of the salient pole prototype . . . . .	12
2.2	Dimensions in millimeters of the salient pole prototype . . . . .	14
2.3	Magnetization curve of the material M270-35A used in the salient pole prototype. . . . .	16
2.4	Measured voltages at no-load on the salient pole prototype. . . . .	16
2.5	Comparison of the no-load characteristic obtained by the company by means of FEM simulations and the measured one for $n = 2000$ rpm. . . . .	17
2.6	Vector diagram at no-load of the salient pole rotor. . . . .	19
2.7	Magnetic circuit of the d-axis used for the computation of the no-load characteristic. . . . .	20
2.8	Explanation chart of the analytical computation of the no-load characteristic. . . . .	20
2.9	Division of the stator tooth into two pieces for the computation of the ampere turns . . . . .	23
2.10	Comparison of the computed no-load characteristic and that obtained by the company by means of FEM simulations for $n = 2000$ rpm . . . . .	25
2.11	FEM model of the stator. . . . .	27
2.12	FEM model of the air gap. . . . .	28
2.13	FEM model of the rotor of the salient pole machine. . . . .	29
2.14	Effect of the rotor pole shape on the no-load voltage. . . . .	30
2.15	Reference angle for designing the rotor pole. . . . .	30
2.16	New rotor pole shape of the salient pole machine. . . . .	31
2.17	Voltage at no-load obtained with the new rotor pole shape. . . . .	31
2.18	Equivalent circuit used for FEM simulations. . . . .	32
2.19	Equivalent circuit used for FEM simulations at no-load. . . . .	33
2.20	Comparison of the no-load characteristic obtained via FEM simulations and that obtained via FEM simulations by the company. . . . .	34
2.21	Magnetic flux density in the air gap obtained via FEM simulations for the salient pole machine. . . . .	34
2.22	Vector diagram at load of the salient pole machine. . . . .	35
2.23	Equivalent circuit used for FEM simulations at load. . . . .	36
2.24	Back electromotive force and phase current for a stator current only in q-direction before the adjustment (a) and after (b). . . . .	38
2.25	Electro-magnetic torque WP1 . . . . .	39
2.26	Torques for WP1 (a) WP2 (b) and WP3 (c). . . . .	40

2.27	Magnetic flux density map for WP2 simulated and from thesis . . . . .	40
2.28	Lateral view of the machine (left) and reference for the computation of the end windings length (right). . . . .	42
2.29	Reference for the computation of the end rotor winding length for the salient pole machine. . . . .	43
2.30	Reference for the leakage inductance computation. . . . .	44
2.31	Magnetic flux density for a stator current vector of 30 A placed in d-axis (a) and q-axis (b). . . . .	47
2.32	Supplying tables of the salient pole machine . . . . .	50
2.33	Salient pole machine efficiency map . . . . .	51
2.34	New excitation current values adapted for the considered number of rotor turns. . . . .	51
2.35	Selected working points to be simulated for the salient pole machine. . . . .	52
2.36	Results obtained from FEM simulation for each selected working point of the salient pole machine. . . . .	52
2.37	Obtained efficiencies of the six simulated working points of the salient pole machine. . . . .	55
2.38	Comparison of the obtained efficiencies from FEM simulations to those reported in the PhD thesis . . . . .	55
3.1	Usual design of the large tooth dimension for the cylindrical rotor machine. . . . .	57
3.2	Design of the rotor slots of the cylindrical rotor machine. . . . .	58
3.3	Selection of the working point of the salient pole machine used as a reference for the design of the cylindrical rotor machine. . . . .	59
3.4	Final cylindrical rotor geometry. . . . .	60
3.5	Centrifugal forces acting on the base of the tooth. . . . .	62
3.6	FEM model of the cylindrical rotor machine. . . . .	65
3.7	Vector diagram at no-load of the cylindrical rotor machine. . . . .	66
3.8	Voltage at no-load for $n = 2000$ rpm, $I_{exc} = 1$ A. . . . .	67
3.9	No-load characteristic obtained via FEM simulations for $n = 2000$ rpm for the cylindrical rotor machine. . . . .	67
3.10	Vector diagram at load for working point 1 . . . . .	68
3.11	Obtained torque from FEM simulations for the working point 1. . . . .	69
3.12	Magnetic flux density color shade chart of the cylindrical rotor for the working point 1. . . . .	69
3.13	Magnetic flux density for a stator current vector of 30 A placed in d-axis (a) and q-axis (b) . . . . .	72
3.14	Vector diagram at load of the cylindrical rotor machine. . . . .	74
3.15	Supplying conditions for WPC in the cylindrical motor. . . . .	75
3.16	Obtained results for WPC in the cylindrical rotor machine. . . . .	75
4.1	No-load characteristics comparison of the salient pole machine and the cylindrical rotor machine for $n = 2000$ rpm. . . . .	77
4.2	Magnetic flux density at no load comparison at 2000 rpm and $I_{exc} = 1$ A: (a) salient pole and (b) cylindrical rotor. . . . .	78
4.3	No-load voltages for $I_{exc} = 0.2$ A (a) and for $I_{exc} = 1.6$ A (b) for the salient pole machine and the cylindrical rotor machine. . . . .	78

4.4	Spectrum of the magnetic flux density in the air gap for the salient pole machine and the cylindrical rotor machine for different excitation currents and at a speed of 2000 rpm. . . . .	79
4.5	Fundamentals of the magnetic flux density in the air gap for the salient pole machine and the cylindrical rotor machine for different excitation currents and at a speed of 2000 rpm. . . . .	80
4.6	Torque comparison for $I_{exc} = 1$ A, $I_q = 246$ A and $I_d = 0$ A of the salient pole machine (a) and of the cylindrical rotor machine (b). . . . .	83
4.7	Linkage fluxes in salient pole (a) and cylindrical rotor (b). . . . .	83
4.8	Magnetic field lines with stator current in d- and q-axis in salient pole respectively (a) and (b) and in cylindrical rotor (c) and (d). . . . .	85
4.9	Reference for the angle $\beta$ for the torque comparison. . . . .	86
4.10	Salient pole machine and cylindrical rotor output torque obtained by FEM in functions of the stator current vector angle and amplitude for different excitation currents. . . . .	88
4.11	Comparison of the magnetic flux density f the salient pole machine and the cylindrical rotor machine for working point C of Figure 2.35. . . . .	90
5.1	Comparison of the torque of the original cylindrical machine with a possible skewed machine. . . . .	93

# List of Tables

1.1	Different motor types used in commercial vehicles . . . . .	4
1.2	Differences between Salient Pole Machine and Cylindrical Rotor Machine .	7
2.1	Main specifications of the salient pole prototype. . . . .	13
2.2	Main geometric data of the salient pole prototype. . . . .	13
2.3	Extrapolated data of the stator winding. . . . .	14
2.4	Extrapolated Data of the rotor winding of the salient pole prototype. . . . .	15
2.5	Working points suggested by the company to calibrate the FEM model. . . .	17
2.6	Working points . . . . .	39
2.7	Values of fundamentals of the magnetic flux density in the air gap for different stator currents in the salient pole machine. . . . .	47
3.1	Values of fundamentals of the magnetic flux density in the air gap for different stator currents in the cylindrical rotor machine. . . . .	72
4.1	Parameters Comparison . . . . .	81
4.2	Linkage fluxes in (d,q) frame for the salient pole motor and cylindrical rotor motor . . . . .	84
4.3	Supplying conditions of the salient pole machine and the cylindrical rotor machine for working point C of Figure 2.35. . . . .	89
4.4	Obtained results of the salient pole machine and the cylindrical rotor machine for working point C of Figure 2.35. . . . .	89

# Nomenclature

$\alpha$	Temperature coefficient of copper at 20 °C
$\beta$	Angle between the stator current vector and the q-axis
$\Delta T$	Difference of the reference temperature of $\alpha$ and the considered one
$\delta$	Air gap length in function of the angle $\theta$
$\delta$	Load angle between the back electromotive force vector and voltage vector
$\delta_d$	Equivalent air gap length considered for the computation of the inductance in the d-axis
$\delta_q$	Equivalent air gap length considered for the computation of the inductance in the q-axis
$\delta_0$	Minimum air gap length
$\eta$	Efficiency
$\lambda$	Permeance factor
$\lambda_d$	Component of the linkage flux in the d-axis
$\lambda_q$	Component of the linkage flux in the q-axis
$\mu_0$	Vacuum magnetic permeability
$\omega_r$	Rotational speed of the rotor in rad/s
$\Phi_{exc}$	Flux per pole at no load
$\Phi_t$	Magnetic flux in the stator tooth of the salient pole machine
$\rho$	Copper resistivity
$\tau$	Pole pitch
$\tau_p$	Non-slotted rotor pole pitch for the cylindrical rotor machine
$\tau_s$	Slotted rotor pole pitch for the cylindrical rotor machine
$\tau_s$	Stator slot pitch
$\tau_{rs}$	Rotor slot pitch of the cylindrical rotor machine

$\theta_e$	Electric angle
$\theta_m$	Mechanical angle
$\varphi$	Angle between the stator current vector and the stator voltage vector
$a$	Number of parallel windings
$A_g$	Ampere turns necessary to magnetize the air gap of the salient pole machine
$A_p$	Ampere turns necessary to magnetize the pole of the salient pole machine
$A_{ry}$	Ampere turns necessary to magnetize the rotor yoke of the salient pole machine
$A_{sy}$	Ampere turns necessary to magnetize the stator yoke of the salient pole machine
$A_{tot}$	Total ampere turns
$A_{WP1}$	Ampere turns of the working point 1
$A_{t_i}$	Ampere turns necessary to magnetize the stator tooth
$B_d$	Magnetic flux density obtained for a stator current vector in the d-axis
$B_{1d}$	Fundamental of the magnetic flux density obtained for a stator current vector in the d-axis
$B_{g,max}$	Magnetic flux density in the air gap of the salient pole machine
$B_p$	Magnetic flux density in the pole of the salient pole machine
$B_{ry}$	Magnetic flux density in the rotor yoke of the salient pole machine
$B_{st1}, B_{st2}$	Magnetic flux density piece 1 and 2 of the stator tooth
$B_{sy}$	Magnetic flux density in the pole of the stator yoke of the salient pole machine
$D_r$	Diameter of rotor conductor of the cylindrical rotor machine
$d_{cu}$	Copper mass density
$d_{fe}$	Iron mass density
$D_{si}$	Stator inner diameter
$D_{so}$	Stator outer diameter
$D_s$	Shaft diameter
$f$	Frequency
$F_c$	Centrifugal force acting on one rotor tooth
$h$	Ratio between the short slot height and long slot height of the cylindrical rotor machine
$H_{g,max}$	Magnetic field in the air gap of the salient pole machine

$H_{psy}$	Magnetic field in stator yoke of the salient pole machine
$H_p$	Magnetic field in the pole of the salient pole machine
$h_p$	Pole height of the salient pole machine
$H_{ry}$	Magnetic field in the rotor yoke of the salient pole machine
$h_{ry}$	Rotor yoke height of the salient pole machine
$H_{st1}, H_{st2}$	Magnetic field of piece 1 and 2 of the stator tooth
$h_{st1}, h_{st2}$	Heights of piece 1 and 2 of the stator tooth
$h_{sy}$	Stator yoke of the salient pole machine
$i_\alpha, i_\beta$	Instantaneous values of the currents in $(\alpha, \beta)$ frame
$i_a, i_b, i_c$	Instantaneous values of the currents in the three phases
$I_d$	Value of the d-component of the stator current
$I_q$	Value of the q-component of the stator current
$i_d, i_q$	Instantaneous values of the currents in (d, q) frame
$I_{exc}$	Value of the excitation current
$I_{max}$	Maximum peak phase current
$J$	Current density
$k_c$	Carter factor
$k_d$	Distribution factor
$k_p$	Pitch factor
$k_w$	Winding factor
$k_{cr}$	Rotor Carter factor of the cylindrical rotor machine
$k_{f,r}$	Rotor filling factor
$k_{f,s}$	Stator filling factor
$k_{st}$	Stack factor
$L$	Active length of the machine
$L_\sigma$	Leakage inductance
$L_d$	Inductance in the d-axis
$L_m$	Magnetizing inductance of the cylindrical rotor machine
$L_q$	Inductance in the q-axis

$L_s$	Length of one stator turn
$L_\sigma$	Mechanical stress
$L_{ew,s}$	Length of the rotor end winding of the salient pole machine
$L_{ew,s}$	Length of the stator end winding
$L_e$	Effective length of the machine
$L_{md}$	Magnetizing inductance in the d-axis
$L_{mq}$	Magnetizing inductance in the d-axis
$L_r$	Total length of one turn of the rotor winding
$m$	Number of phases
$m_t$	Total mass considered for the computation of the centrifugal forces acting on one rotor tooth
$m_{cu,ew}$	Copper mass of the rotor end winding considered for the computation of the centrifugal forces on one rotor tooth
$m_{cu,s}$	Copper mass in the rotor slots considered for the computation of the centrifugal forces on one rotor tooth
$m_{fe}$	Iron mass considered for the computation of the centrifugal forces acting on one rotor tooth
$N_r$	Number of turns per pole of the salient pole machine
$N_r'$	Number of turns per pole of the cylindrical rotor machine
$n_{max}$	Maximum speed in rpm
$N_{r,ls}$	Number of turns per pole of the cylindrical rotor machine in the long slot
$N_{r,ss}$	Number of turns per pole of the cylindrical rotor machine in the short slot
$N_{rs}$	Number of rotor slots for the cylindrical rotor machine
$N_{ss}$	Number of stator slots
$N_s$	Number of turns in series per phase
$p$	Number of pole pairs
$P_{fe}$	Total iron losses
$P_{J,r}$	Rotor Joule losses
$P_{J,s}$	Stator Joule losses
$P_J$	Total Joule losses

$P_{max}$	Maximum power
$P_m$	Mechanical losses
$P_{out}$	Output mechanical power
$q$	Number of slots per pole and per phase
$S_c$	Cross section of stator conductors
$S_r$	Cross section of rotor conductor of the salient pole machine
$S'_r$	Cross section of rotor conductor of the cylindrical rotor machine
$S_s$	Stator slot surface
$S_t$	Total coil area in the rotor of the salient pole machine
$SH$	Height of the long slot of the cylindrical rotor
$sh$	Height of the short slot of the cylindrical rotor
$SH_{tot}$	Total slot height of the cylindrical rotor machine
$SW$	Slot width of the cylindrical rotor
$T$	Torque
$T_{max}$	Maximum torque
$V_{DC}$	Battery voltage
$V_{max}$	Maximum peak phase voltage
$w_{ps}$	Preslot width
$w_p$	Pole width of the salient pole machine
$w_{ry}$	Rotor yoke width of the salient pole machine
$w_{st1}, w_{st2}$	Widths of piece 1 and 2 of the stator tooth
$w_{sy}$	Stator yoke width of the salient pole machine
$WDG$	Rotor wedges height of the cylindrical rotor machine
$X_d$	Reactance in the d-axis
$X_q$	Reactance in the q-axis
$X_s$	Synchronous reactance of the cylindrical rotor machine
$Z$	Number of conductors per slot
$Z_c$	Number of equivalent series conductors

# Chapter 1

## Introduction

### 1.1 State of the Art

In the last three decades, automotive industry has seen many changes. The rise of fossil fuels price, and a more stringent regulation of pollution issue have driven to shift the attention from Internal Combustion Engine (ICE) to alternatives characterized by reduced consumption and emissions. This has led to an increasing interest in Electric Vehicles (EV) and Hybrid Electric Vehicles (HEV). Thus, efforts have been made in order to achieve high efficiencies of the entire EV traction line, both by optimizing the design of each component and better coordinating all its different parts. The electric motor is certainly one of the most important elements of the traction line. The required characteristics of the electric motor have been widely investigated in order to make EV competitive in the automotive market [1–3]. First of all, its torque-speed characteristic must be similar to the one represented in Figure 1.1. As the graph shows, the curve can be divided into two regions: the constant rated torque region and the constant power region. In the first one, the electric motor provides its maximum torque ( $T_m$ ) until the base speed ( $n_b$ ) is reached. At this speed, the motor is already at its maximum power, therefore the torque has to decrease in order to keep increasing the speed. This is the constant power region, that extends up to the maximum speed. While a conventional internal combustion engine needs a gearbox to fit the curve, an electric motor could beneficially satisfy this demand electronically.

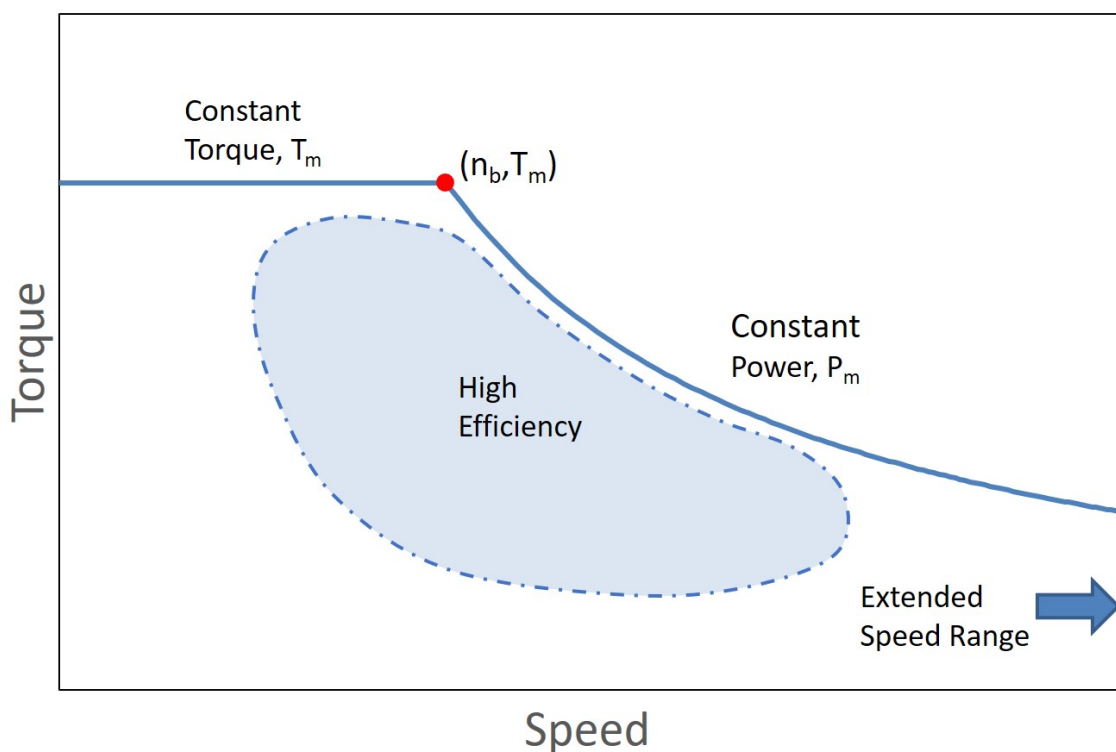


Figure 1.1: Ideal Torque-Speed characteristic for electric vehicles.

Moreover, general requirements have been pointed out in EV literature and some of them are reported below:

- High efficiencies, especially in the area showed in Figure 1.1;
- High power and torque densities;
- Extended speed range (Figure 1.1);
- Reliability and robustness;
- Low price;
- Minimized torque ripple and noises;

Despite the clarity about automotive requirements, the selection of the most suitable electric motor for this purpose is still an issue. At present, among the existing electric motors, four have been mostly investigated and employed [4], they are recollected in the following list.

- DC Motors;
- Induction Motor (IM);
- Permanent Magnet (PM) motor;
- Reluctance Motor (RM);

Currently, most of commercial electric vehicles are equipped with either an induction motor or a permanent magnet motor. DC motors were used in the first electric vehicles, but they are basically not employed anymore. Lately, the reluctance motor has gained the attention of investigation. Each of these motors has different characteristics and different reasons for being an appropriate choice for electric traction application. They will be briefly discussed one by one in the following sentences, highlighting their advantages and drawbacks [5–9].

#### ***-DC Motor***

DC motors are a well known technology, they are simple to construct and to control. Nevertheless, the presence of brushes and commutators has discouraged from using this kind of motor since they need a periodic maintenance.

#### ***-Induction Motor***

The induction (or asynchronous) motor has been widely employed in electric vehicles, since it has some appealing characteristics. First of all, it is an inexpensive and well-known technology. It does not need any permanent magnet or any mechanical contact to bring current to the rotor, which also make it reliable, free maintenance and cheap. The main drawbacks are: a reduced range of constant power, a low power factor, low inverter-usage factor, high loss and low efficiency.

#### ***-PM Motor***

Along with the IM, the permanent magnet is highly dominant in automotive propulsion scenario. The reason for its spread is that most of the characteristics required by EV can be

easily found in this type of motor since it is torque-dense, very efficient, and easy to control. Moreover its noise and torque ripple are low. Nevertheless, the uncertainty about the availability of rare-earth magnets, their high price and the Chinese monopoly of them have discouraged some car manufacturers from employing them.

**-Reluctance Motor**

The investigation is now moving forward the reluctance motor with promising developments. In this type of motor, the torque is only produced by the different reluctance of the d-axis and the q-axis. It presents a very robust and cheap rotor due to the absence of both copper and iron. In addition, it can reach higher speeds and its torque-speed characteristic is suitable for electric vehicles application. Anyway they present also some disadvantages such as noise and vibrations, difficulty of manufacturing. It is worth to present some of the motors used in commercial electric cars [5, 6]:

<b>Motor</b>	<b>Electric Vehicle</b>	<b>Motor</b>	<b>Electric Vehicle</b>
<i>DC motor</i>	Fiat Panda Elettra (1990)	<i>Induction Motor</i>	Tesla Model S (2012)
<i>DC motor</i>	Conceptor G-Van (1990)	<i>Induction Motor</i>	Tesla Model X (2015)
<i>DC motor</i>	Citroen Berlingo (1998)	<i>PM motor</i>	Toyota Prius (1997)
<i>Induction Motor</i>	GM EV1 (1996)	<i>PM motor</i>	Honda Insight (2000)
<i>Induction Motor</i>	Tesla Roadster (2008)	<i>PM motor</i>	Mitsubishi-MiEV (2009)
<i>Induction Motor</i>	Ford Focus Electric (2011)	<i>PM motor</i>	Soul EV (2014)
<i>Induction Motor</i>	Fiat Doblò (2011)	<i>SR motor</i>	Chloride Lucas (1977)

Table 1.1: Different motor types used in commercial vehicles

As Table 1.1 shows, PM motors are predominantly employed by eastern car manufacturers because of the higher availability of permanent magnets there. On the contrary, western car manufacturers have preferred machines without permanent magnets, such as IM. Hence, as previously stated, even though PM motors seem to be the most promising technology, car manufacturers are still looking for a valid alternatives [10].

## 1.2 Wound Field Synchronous Motors

Presently, very few car manufacturers employ wound field synchronous machines (WFSM) as the motor of commercial electric vehicles. In 2013, two WFSMs have been used for the first time in automotive applications, and one of them can be found in the Renault Zoe EV [11]. The wound field synchronous machine is a well-known technology, since it has historically been used as the generator of most existing power plants. Nevertheless, the specific requirements of the electric traction open up new challenging goals in investigating this machine as a traction motor. As well as the reluctance motor, the wound field synchronous machine does not have any permanent magnet inside. Its rotor hosts a winding for the injection of a continuous current, allowing to create an excitation field. This results in performing the same task of permanent magnets in a PM motor. One of the drawbacks of the PM machine, is that the stator winding has to be overloaded in order to reach a very high torque. The possibility to do it mainly relies on the maximum current that can be provided by the inverter. As a consequence, if higher torque is desired, an oversizing of the inverter is needed. This leads to a higher cost of the whole traction line. The WFSM can be a possible solution to this problem, since it can generate high torque at low speed by overloading both the stator and the rotor and this allows to keep the stator current at lower values in comparison with a PM machine. Furthermore, as previously said, it is very important that the motor can guarantee a constant power for a wide speed range. The WFSM is the most appropriate for this purpose, considering that the excitation current can be varied as desired to have a constant power until theoretically unlimited speed. This is why WFSM has been receiving an increasing interest as suitable alternative to the dominant technologies in EV applications [12–17].

### 1.2.1 Salient Pole Rotor vs Cylindrical Rotor

The WFSM comes in two possible configurations depending on the rotor construction: salient pole machine, in which the field poles project, and non-salient pole machine (also known as "cylindrical rotor"), in which the field poles do not project. This difference is evident by looking at the simplified schemes showed in Figure 1.2.

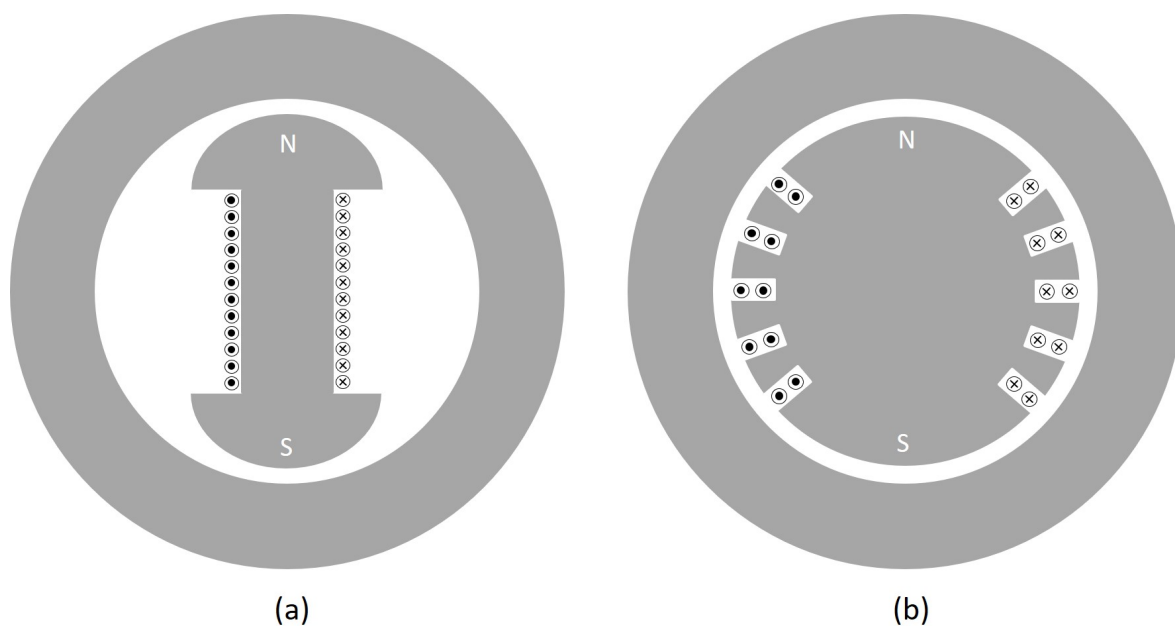


Figure 1.2: Salient Pole Machine (a) and Cylindrical Rotor Machine (b).

As Figure 1.2 depicts, the salient pole machine presents a variable air gap that causes strong anisotropies, while the cylindrical rotor machine can be considered as an isotropic geometry because of its cylindrical shape. Of the two solutions, the second one has generally been employed in high speed applications. Indeed, when the peripheral speed of the rotor is meant to be very high, it is convenient to distribute the winding over the rotor surface in order to guarantee sufficient mechanical resistance, as well as better arrangement and securing of excitation winding [18]. Moreover, the better enclosure of the rotor conductors allows to reduce their mechanical vibration, resulting in warding off the risk of insulation deterioration. Furthermore, to reduce the mechanical stress caused by centrifugal forces, cylindrical rotor alternators have generally smaller diameters if compared to salient pole machines, but also longer axial length. This means that the available space to fit the poles in the rotor is less than that on a salient pole machine and, consequently, the number of poles is usually smaller. Finally, cylindrical rotor machines generally allow to get a better distribution of magnetic flux density in the air gap, and consequently a better electromotive force. What stated so far is recollected in the following table.

<b>Salient Pole Machine</b>	<b>Cylindrical Rotor Machine</b>
Poles project from the surface	Cylindrical shape
Variable air gap	Constant air gap
High number of poles	2-4 poles
Less robust	More robust
Suitable for lower speeds	Suitable for higher speeds
Worse mechanical resistance	Better mechanical resistance
Worse emf waveform	Better emf waveform
Easier construction	More complex construction

Table 1.2: Differences between Salient Pole Machine and Cylindrical Rotor Machine

As previously mentioned, the WFSM has already been employed as the traction motor of commercial electric vehicles. In the best author's knowledge, of the two possible configurations, only the salient pole machine has been investigated and used for this purpose. Nevertheless, the cylindrical rotor machine presents some undeniable advantages from a mechanical point of view, especially when it comes to high speed applications, such as automotive applications. Therefore, it is worth asking if this kind of machine can be employed as the traction motor of electric vehicles. Indeed, in the automotive industry, the patent [19] published in 2018 by the car maker BMW represents one of the first investigation of a WFSM with cylindrical rotor as viable solution for traction applications.

### 1.2.2 How to bring current to the rotor

Since the WF-SM presents a lot of advantages, this prompts the question as to why it is not spread in EV applications. As stated in [11], the main potential of the WF-SM is also its main drawback: the current in the rotor. In order to supply the rotor, slip rings are usually used. They are electromechanical devices that allow transferring power from a static part to a rotating one with a mechanical contact of the two. Even though it is now a well known technology, producers prefer to avoid it when it comes to electric vehicles applications because of their concern about maintenance and reliability. Nevertheless, there are other methods to

achieve the goal. Some of them are presented below.

### Rotary Transformers

Rotary transformer is one of the most used technology when it comes to non-contact power transfer. It consists of two electronic systems and the transformer itself and it offers the advantage of reducing the cost of WF-SM in comparison with machines excited via slip rings and brushes. Since the power transfer in a transformer can be achieved only if the supply voltage is an AC input, the first electronic system must be a DC-AC converter. The output of the latter feeds the primary side of the transformer, which is static. The power is transferred to the secondary side, which is attached to the shaft and consequently it is rotating. Finally, by means of a rotating rectifier the output voltage is suitable to feed the rotor winding. The following scheme explains what stated before.

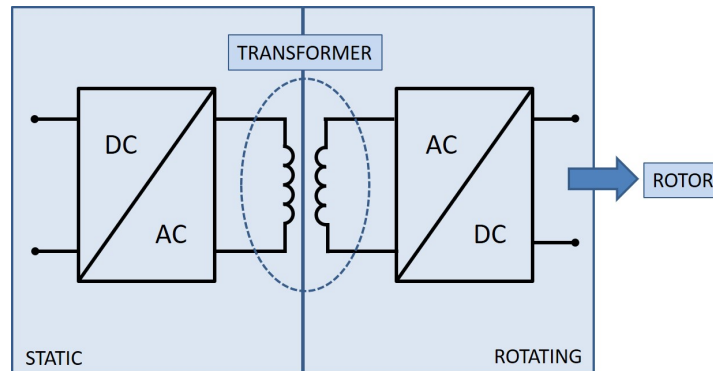


Figure 1.3: Rotating transformer scheme.

Lately, different rotary transformer solutions have proposed also for WR-SMs for automotive purposes [20, 21]. Despite this is a valid solution to slip rings issue, it has to be noticed that it also causes a rise in the motor weight and in the shaft length.

### Capacitive Power Transfer

Another non-contact solution for transferring power is the employment of a rotating capacitor [22]. The basic construction is that of a common capacitor: two conductive materials, separated by a dielectric. In this specific application, one of the two conductive material is rotating with respect to the other. These two can comes into two possible configurations:

concentric hoops or parallel plates. In any case, the impedance of the capacitor is inversely proportional to both the capacitance and the frequency. Thus, to have an optimal power transfer, both need to be maximized. For what concerns the capacitance, it can be computed as:

$$C = \frac{\varepsilon \cdot A}{\delta} \quad (1.1)$$

Where  $A$  is the surface of the plates and its expression depends on which of the two technologies is adopted,  $\varepsilon$  is the permittivity and  $\delta$  the air gap length. Therefore, this type of exciter generally requires large air gap surface and small air gap length, as well as high operating frequencies. Consequently, a rectifier has to be used to properly feed the rotor coil.

### **Harmonic Power Transfer**

Harmonic excitation mainly refers to third harmonic excitation systems. They have been employed for the first time in WR-SM generators. The first harmonic exciters used specific rotor shapes to enhance the third harmonic in the rotor magnetic field. The stator was equipped with a harmonic winding. When rotating, the rotor induced a third harmonic voltage in the harmonic stator winding, which supplied the rotor winding, by means of a rectifier and slip rings. To remove the latter ones, an additional AC rotor harmonic winding can be used. In this case, the stator harmonic winding fed the rotor harmonic winding without any mechanical contact, and again by means of a rectifier, the rotor harmonic winding supplied the main rotor winding. Nevertheless, this makes the structure more complicated. An other possible solution is proposed in [23], in which the brushless exciter technology can be simplified by generating the spatial third harmonic MMF from the stator instead of the rotor. However, all these technologies can only be used in generator applications, since it is mandatory the the rotor is moving to feed it. In the work proposed in [24], a double third harmonic current excitation is used to overcome this issue. Here, the stator is equipped with two windings. The two stator currents consist of a fundamental current and a third harmonic current. Both these two currents can generate a rotating magnetic field in the air gap and induce EMF in the harmonic rotor winding. By means of a rotating rectifier, the latter supplies the main rotor winding. When the phase of the two third harmonics current are orthogonal, the generated

harmonic magnetic field can be controlled in its spatial position and amplitude. This allows to excite the rotor either if it is moving or it is stationary.

### **1.3 Thesis Goal**

Accordingly to what said so far, it is evident that the wound field synchronous machine is a promising technology in automotive field. In high speed applications, the conductors of the excitation winding in wound field synchronous machine are subjected to large centrifugal forces, causing dangerous mechanical vibrations that could lead to the deterioration of conductor's insulation. This issue has been encountered in electric vehicles equipped with a salient pole synchronous motor. Hence, some car manufacturers are investigating the non-salient cylindrical rotor as a possible alternative, since it can guarantee a better enclosure of the rotor conductors and better mechanical resistance. This thesis aims to carry out a comparative analysis of the salient pole and the cylindrical rotor solutions in terms of performances. An already existing salient pole prototype for electric traction is used as the baseline of the study. Its main characteristics are reported in in the previously published PhD thesis [25]. The aim of Chapter 2 is to extrapolate all the necessary data, and to create a reliable finite element model of the existing salient pole machine, by using information provided by both the PhD thesis and the owner company. By means of FEM simulations analytical computations the machine parameters, and torques, efficiencies and losses are computed in some operating points. In Chapter 3, a preliminary sizing of the cylindrical rotor machine is accomplished, by keeping the same stator and respecting electromagnetic constraints. Subsequently, a consistent finite element model of the new machine is created and simulated. The comparison in terms of performances of the two machines is achieved in Chapter 4, by means of analytical and finite element analysis. Finally, in Chapter 5 some conclusions are drawn and some possible future works are suggested.

# Chapter 2

## Salient Pole Machine

### 2.1 Available Data of the Salient Pole Machine

As stated in Chapter 1, the goal of the thesis is to perform a comparative analysis of two different rotor configurations for a wound field synchronous motor for electric traction application, by maintaining the same stator. An already existing salient pole prototype for electric traction is used as the baseline of the study. The comparison between the salient pole machine and the cylindrical rotor machine is carried out by means of analytical computations and numerical simulations, using the software Flux2D. Hence, the first step of the investigation is to recollect all the needed data about the salient pole motor, in order to create a reliable model of the latter that can be used for the comparison.

Most of the information about the machine can be found in the PhD thesis [25], whose main purposes are: to develop a rotor current controller for rotor excitation through brushes; to design a new version of motor without brushes using a rotary transformer; to propose some improvements of the machine (such as rising the filling factor and adding head barrier or permanent magnets in the rotor poles). The second goal confirms that for this kind of machines it is essential to find a way to transfer power to the rotor without any mechanical contact, as outlined in the introduction. By the way, as the reference thesis aims to improve the original prototype, several prototypes of the same machine have been built and tested and their data reported. For information referred to different prototypes or for missing data, the owner

company provided what needed. Thus, in the following section the main characteristics of the salient pole machine are recollected and other deducted.

### 2.1.1 Data extrapolated from the PhD thesis

Figure 2.1 shows the system architecture for the salient pole motor. A high battery voltage supplies the inverter, which is connected to the three phases of the stator. This is the typical system architecture of a classical motor for electric traction that does not need to supply the rotor, such as an induction motor or a permanent magnet motor. Here, two additional elements are necessary to inject current in the rotor winding: a rotor current controller and an energy transfer system (brushes, rotary transformer and so on).

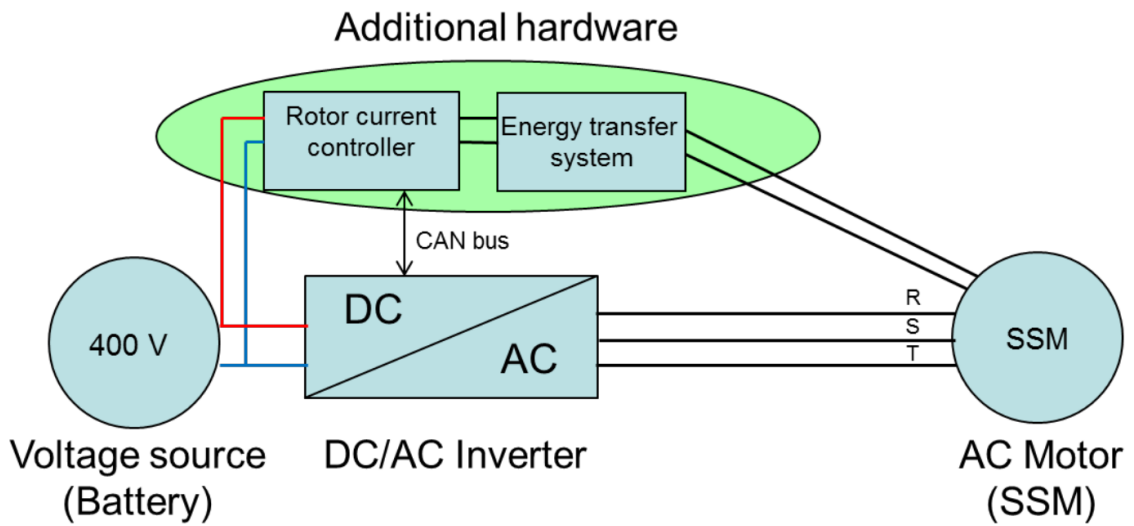


Figure 2.1: System architecture of the salient pole prototype [25].

Therefore, the first information about the voltage limits can be deducted. As the supply voltage from the battery is 400V, the value of the maximum peak phase voltage can be obtained as shown from equation (2.1).

$$V_{max} = \frac{V_{DC}}{\sqrt{3}} \approx 230 \text{ V} \quad (2.1)$$

Furthermore, the maximum current has been provided by the company and its peak value is:

$$I_{max} = 636 \text{ A} \quad (2.2)$$

As reported in the thesis [25], the machine is a three-phase, 6-poles motor, whose main specifications are recollected in the following table.

Variable	Value
<i>Maximum Power (<math>P_{max}</math>)</i>	130 kW
<i>Maximum Torque (<math>T_{max}</math>)</i>	240 Nm
<i>Maximum Speed (<math>n_{max}</math>)</i>	12 000 rpm

Table 2.1: Main specifications of the salient pole prototype.

The machine has an active length of 123mm, an active diameter of 240mm, a rotor inner diameter of 84mm. All the geometric information found is showed in Table 2.2.

Variable	Value
<i>Number of Poles Pairs (<math>p</math>)</i>	3
<i>Number of Phases (<math>m</math>)</i>	3
<i>Active Length (<math>L</math>)</i>	123 mm
<i>Stator inner diameter (<math>D_{si}</math>)</i>	165 mm
<i>Stator outer diameter (<math>D_{so}</math>)</i>	240 mm
<i>Shaft diameter (<math>D_s</math>)</i>	85 mm
<i>Minimum Air Gap (<math>\delta_0</math>)</i>	0.5 mm

Table 2.2: Main geometric data of the salient pole prototype.

The following step is to extrapolate the whole geometry of the machine. For this purpose, a 2D section of the motor model is used. Knowing both the shaft diameter and the stator internal diameter has allowed to verify that figures reported in the PhD thesis were correctly scaled. Thus, the main dimensions have been easily obtained, as showed in Figure 2.2.

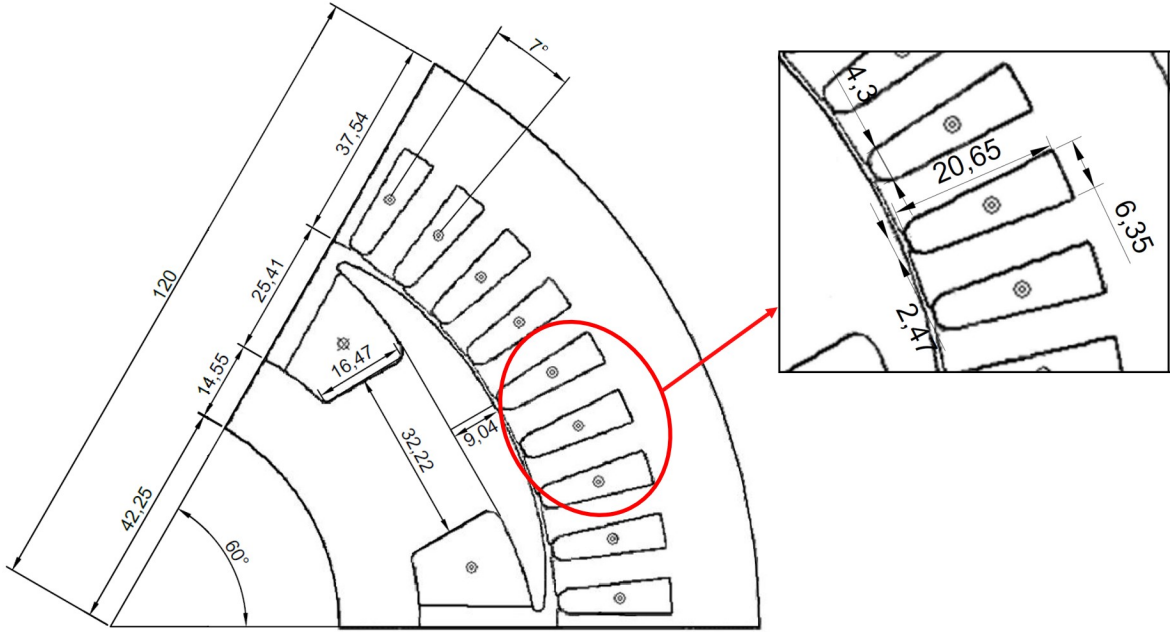


Figure 2.2: Dimensions in millimeters of the salient pole prototype

Once the geometry is known, the stator and rotor winding arrangements must be figured out. For what concerns the stator winding, the deduced information, from the PhD thesis, is recollected in Table 2.3.

Variable	Value
<i>Number of stator slots (<math>N_{ss}</math>)</i>	54
<i>Number of turns in series per phase (<math>N_s</math>)</i>	21
<i>Number of parallel windings (<math>a</math>)</i>	3
<i>Stator filling factor (<math>k_{f,s}</math>)</i>	0.5

Table 2.3: Extrapolated data of the stator winding.

It is a single layer winding, with a number of slots per pole and per phase equals to:

$$q = \frac{N_{ss}}{m \cdot 2p} = 3 \quad (2.3)$$

Since the number of parallel windings is 3, and the numbers of turns in series per phase is 21, the number of conductors in one slot is:

$$Z = \frac{N_{ss}}{q} = 7 \quad (2.4)$$

The pole pitch can be easily computed as:

$$\tau = \frac{D_{si} - \delta_0}{2 \cdot p} \cdot \pi = 0.086 \text{ m} \quad (2.5)$$

For what concerns the winding factor, it is the product of the distribution factor and the pitch factor ( $k_p$ ), which is equals to one since the winding is a single layer. While the distribution factor is computed as follows.

$$k_d = \frac{1}{2 \cdot q \cdot \sin\left(\frac{\pi}{6q}\right)} = 0.96 \quad (2.6)$$

Finally, the winding factor is:

$$k_w = k_d \cdot k_p = 0.96 \quad (2.7)$$

Regarding the rotor winding, it is mentioned in the thesis the the number of turns per pole is 400. Nevertheless, the company suggested to change this value to 843, which means that subsequent adaptations are needed when using any PhD thesis data related to the rotor winding. All that is known about the rotor winding is then showed in the following table.

Variable	Value
<i>Number of turns per pole (<math>N_r</math>)</i>	843
<i>Rotor filling factor (<math>k_{f,r}</math>)</i>	0.45

Table 2.4: Extrapolated Data of the rotor winding of the salient pole prototype.

All the data showed in the previous tables are essential for creating a reliable baseline not only for the comparison of the two machines but also for the design of the new cylindrical rotor solution.

### 2.1.2 Data provided by the company

The PhD thesis [25] mentions that the material used for both the rotor and the stator is an M270-35A, whose magnetization curve was experimentally measured, and the data have been made available by the owner company, such as the value of the stack factor ( $k_{st} = 0.97$ ). The magnetization curve of the material is shown in Figure 2.3.

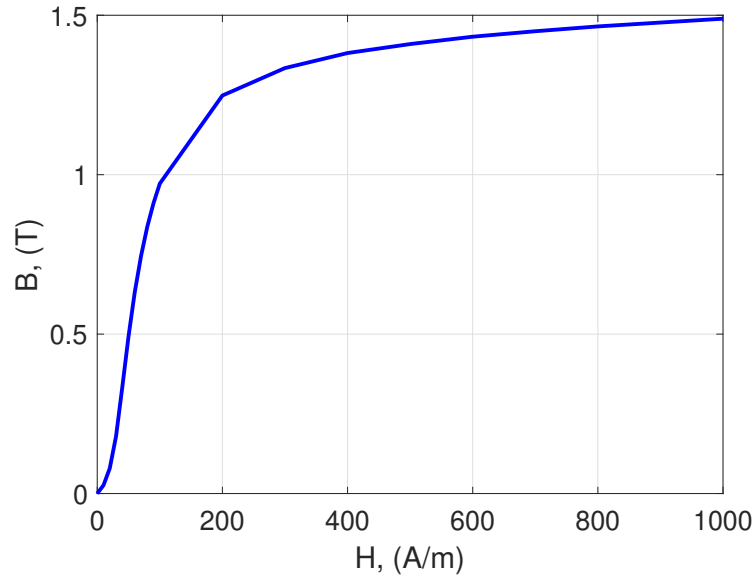


Figure 2.3: Magnetization curve of the material M270-35A used in the salient pole prototype.

Some tests at no-load have been performed on the motor. In particular, the voltages at no-load, at a speed of 2000 rpm and for different excitation currents have been measured. Four of them have been shared and showed in Figure 2.4.

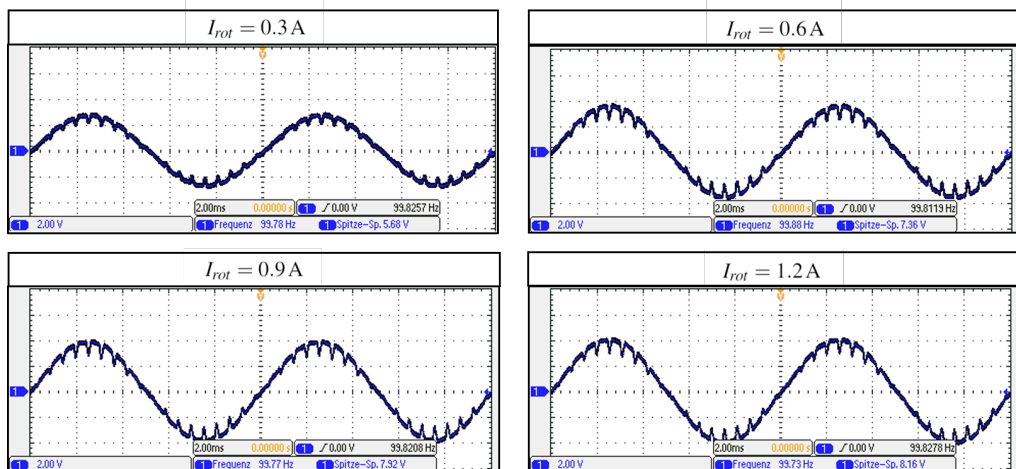


Figure 2.4: Measured voltages at no-load on the salient pole prototype.

By means of these measurements, the company has drawn out the no-load characteristic of the motor. Moreover, the no-load characteristic has been computed also by means of their Flux2D model. In Figure 2.5 the curve obtained via FEM simulations and via measurements are shown in the same graph. As illustrated, there are some differences between the two, especially in the linear part.

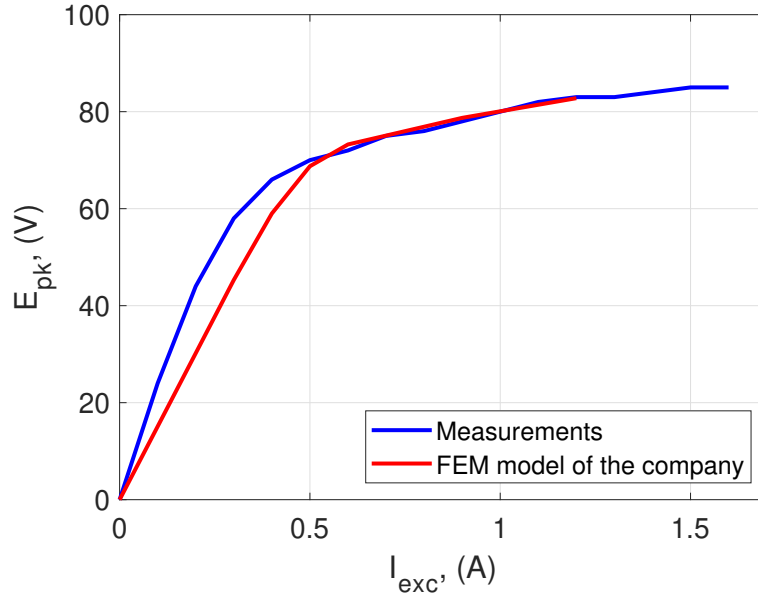


Figure 2.5: Comparison of the no-load characteristic obtained by the company by means of FEM simulations and the measured one for  $n = 2000$ rpm.

The company stated that there are some uncertainties on how the measurements have been carried out and suggested to consider the FEM results more reliable than the measurements. By the way, the goal is not to build the model of the salient pole machine, but to create a baseline for the comparison. Following the suggestions, the FEM simulations are taken as a reference when creating the Flux2D model of the salient pole machine.

	WP1	WP2	WP3
$I_d$ , (A)	0	0	0
$I_q$ , (A)	246	636	636
$I_{exc}$ , (A)	1	2	3.5
$T_{avg}$ , (Nm)	110	225	350

Table 2.5: Working points suggested by the company to calibrate the FEM model.

Furthermore, three different working points have been simulated by the company and provided as a reference for the calibration of the FEM model. These are obtained by injecting a stator current vector only in the q-axis. The supplying conditions and the expected output torques are shown in [2.5](#).

## 2.2 Analytical computation of the No-Load Characteristic

The no-load characteristic of the salient pole machine is analytically computed and compared to the one provided by the company, in order to verify that the geometric dimensions (obtained as stated above) are consistent with the real ones. First of all, it is assumed that the machine is working at no-load, which means that the rotor is powered and it is rotating, while the stator circuit is left open. In this condition the magnetic field is only created by the excitation current. The current vector and its correspondent magnetic flux rotate together with the rotor. The rotation of the continuous magnetic field causes the induction of three sinusoidal emf on the stator winding. Since the emf is the derivative of the flux, then the emf vector is displaced of  $90^\circ$  with respect to the excitation current and excitation field. This situation is showed in the following figure.

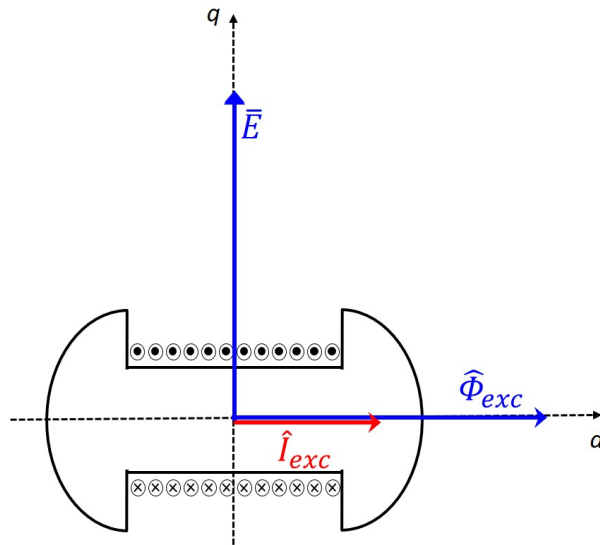


Figure 2.6: Vector diagram at no-load of the salient pole rotor.

By measuring the voltage in the stator coil for different values of the excitation current, for a certain rotational speed, and by plotting the function  $E(I_{exc})$ , the no-load characteristic is obtained. Here, the no-load characteristic of the motor has been given by the company and it is used to calibrate the motor model. An analytical computation of the no-load characteristic is proposed below, and the results are compared to the provided curve. To reach the goal, the magnetic circuit of the d-axis is divided into branches, as Figure 2.7 shows.

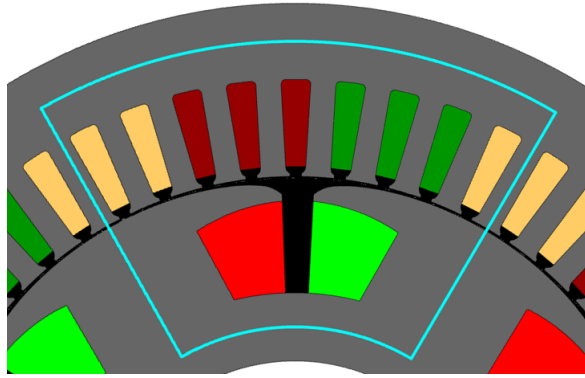


Figure 2.7: Magnetic circuit of the d-axis used for the computation of the no-load characteristic.

The goal is to find the couples  $(I_{exc}, E)$ . To reach it, a value of the phase voltage at no-load  $E$  is chosen and the corresponding excitation current is found as schematically explained by the chart in Figure 2.8.

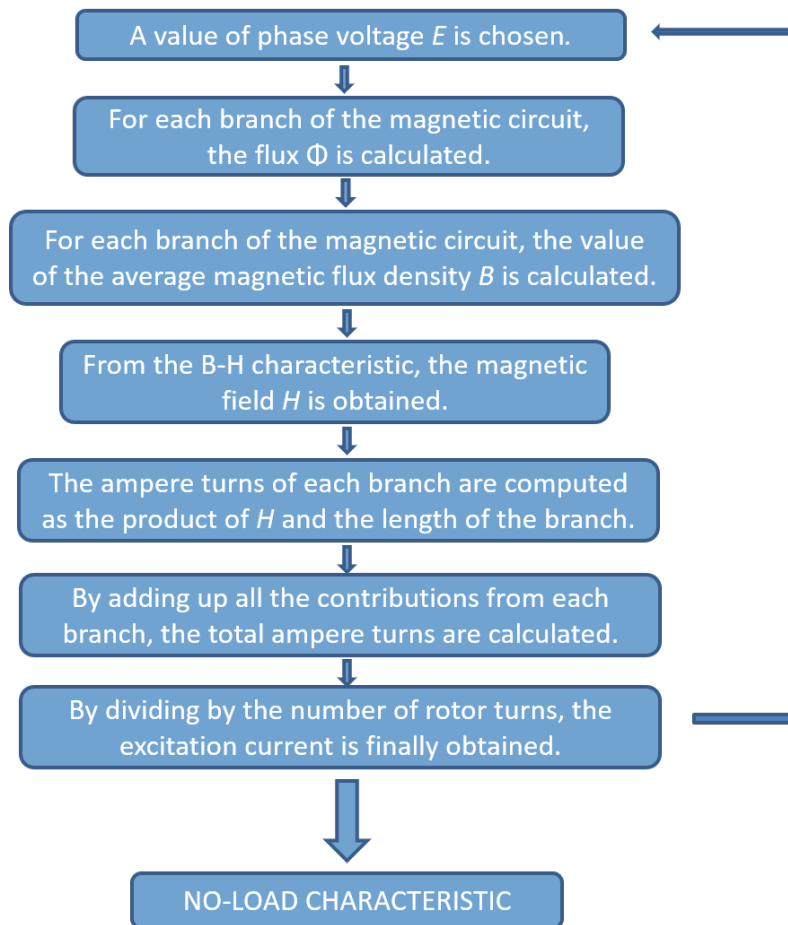


Figure 2.8: Explanation chart of the analytical computation of the no-load characteristic.

The flux mentioned in the second step is flux per pole at no-load and it can be found as follows:

$$\Phi_{exc} = \frac{E}{4.44 \cdot N_s \cdot f \cdot k_w} \quad (2.8)$$

Where  $f$  is the electrical frequency. Since the provided no-load characteristic is obtained for a speed of 2000 rpm, it means the the frequency has to be set as:

$$f = \frac{n \cdot p}{60} = 100 \text{ Hz} \quad (2.9)$$

Below, the ampere turns required to magnetize each branch of the magnetic circuit in the d-axis are computed.

### **Ampere turns required to magnetize the rotor yoke**

The magnetic flux density in the rotor yoke can be obtained as follows:

$$B_{ry} = \frac{\Phi_{exc}}{w_{ry} \cdot L_e} \quad (2.10)$$

Where:

- $w_{ry}$  is the rotor yoke width;
- $L_e$  if the effective length of the machine, computed as the product of  $k_{st}$  and  $L$ .

The magnetic flux density is used as input in the BH curve of the material in order to get the value of the magnetic field in the rotor yoke ( $H_{ry}$ ).

As a consequence, it is possible to find the corresponding ampere turns by multiplying by the rotor yoke height ( $h_{ry}$ ).

$$A_{ry} = H_{ry} \cdot h_{ry} \quad (2.11)$$

### **Ampere turns required to magnetize the pole**

The average magnetic flux density in the rotor pole can be obtained as:

$$B_p = \frac{\Phi_{exc}}{w_p \cdot L_e} \quad (2.12)$$

Where  $w_p$  is the pole width. The average magnetic flux density is used as input in the BH curve of the material in order to get the average value of the magnetic field in the pole ( $H_p$ ). As a consequence, it is possible to find the ampere turns in the pole by multiplying by the pole height ( $h_p$ ).

$$A_p = H_p \cdot h_p \quad (2.13)$$

### Ampere turns required to magnetize the air gap

The maximum flux density in the air gap corresponding to the flux  $\Phi_{exc}$  can be obtained as follows:

$$B_{g,max} = \frac{\Phi_{exc}}{\frac{2}{\pi} \cdot \tau \cdot L} \cdot k_c \quad (2.14)$$

Where  $k_c$  is the Carter factor, that can be computed with the following formula.

$$k_c = \frac{\frac{\tau_s}{w_{ps}}}{\frac{\tau_s}{w_{ps}} - \frac{\frac{\delta_0}{5 + \frac{w_{ps}}{\delta_0}}}{\delta_0}} = 1.15 \quad (2.15)$$

Being  $\tau_s$  the stator slot pitch and  $w_{ps}$  the preslot width.

In the air the relationship between the magnetic flux density and the magnetic field is linear, thus the magnetic field can be obtained by dividing the magnetic flux density by the vacuum magnetic permeability.

$$H_{g,max} = \frac{B_{g,max}}{\mu_0} \quad (2.16)$$

Therefore the required ampere turns in the air gap are:

$$A_g = H_{g,max} \cdot \delta_0 \quad (2.17)$$

### Ampere turns required to magnetize the tooth

Assuming that the flux in each tooth is constant along the radial coordinate, the value of the magnetic flux density has to change whenever the tooth width changes. Therefore the tooth is divided in two pieces whose widths are assumed to be constant, in order to reach a better approximation of the value of the magnetic flux density.

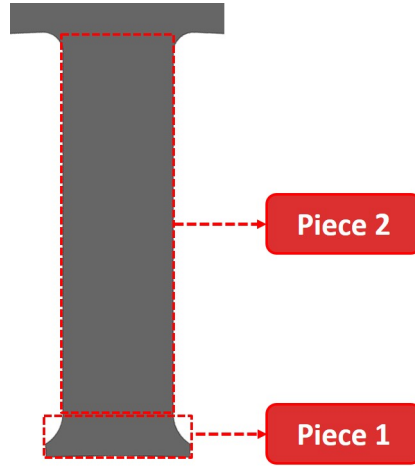


Figure 2.9: Division of the stator tooth into two pieces for the computation of the ampere turns

Knowing the value of the magnetic flux density in the air gap from 2.14, the flux in one tooth can be easily found as:

$$\Phi_t = B_{g,max} \cdot w_{st1} \cdot L_e \quad (2.18)$$

Where  $w_{st1}$  is the width of piece 1 of the tooth, showed in Figure 2.9. In piece 1 the value of the magnetic flux density corresponds to  $B_{g,max}$ , while in piece 2 is:

$$B_{t2} = \frac{\Phi_t}{w_{st2} \cdot L_e} \quad (2.19)$$

Where  $w_{st2}$  is the width of piece 2 of the tooth, showed in Figure 2.9. Again, from the BH curve the corresponding values of the magnetic field for each piece ( $H_{t1}$  and  $H_{t2}$ ) can be obtained. Finally, the ampere turns required to magnetize the whole tooth are:

$$A_t = H_{t1} \cdot h_{t1} + H_{t2} \cdot h_{t2} \quad (2.20)$$

Where  $h_{t1}$  and  $h_{t2}$  are the heights of piece 1 and piece 2 of the tooth, respectively.

### Ampere turns required to magnetize the stator yoke

The average magnetic flux density in the rotor yoke can be approximated as follows:

$$B_{sy} = 0.85 \cdot \frac{\Phi_{exc}/2}{h_{sy} \cdot L_e} \quad (2.21)$$

The average magnetic flux density is used as input in the BH curve of the material in order to get the average value of the magnetic field in the stator yoke ( $H_{sy}$ ).

As a consequence, it is possible to find the required ampere turns by multiplying the magnetic field by  $w_{sy}$ , where  $w_{sy}$  is the arc whose center is the center of the machine, it goes from one pole to the next one and it's collocated in the middle of the stator yoke.

$$A_{sy} = H_{sy} \cdot h_{sy} \quad (2.22)$$

### Total ampere turns and excitation current

After having computed all the contributions of the ampere turns necessary to magnetize the machine in the direct direction, the total ampere turns that each pole has to support can be obtained as expressed by the following formula.

$$A_{tot} = 0.5 \cdot A_{ry} + A_p + A_g + A_t + 0.5 \cdot A_{sy} \quad (2.23)$$

Finally, knowing the rotor turns and also the ampere turns that have to be generated, the excitation current can simply computed dividing the ampere turns by the rotor turns.

$$I_{exc} = \frac{A_{tot}}{N_r} \quad (2.24)$$

This is the value of the excitation current needed to create the no-load voltage  $E$ . By changing the required no-load voltage, a different value of the excitation current is derived. Consequently, by varying the input value  $E$  of the procedure, the no-load characteristic can be obtained.

### Obtained Results and Comparison

Then, this procedure is implemented by using MATLAB. A vector of the peak voltage at no-load is created, whose values go from 0 up to  $V_{max}$ . Following the procedure mentioned above, and using the magnetizing curve of the material provided by the company, the corresponding vector of the excitation current is obtained. Hence, the no-load characteristic is analytically computed.

By plotting on the same graph the no-load characteristic provided by the company and the computed one (Figure 2.10), it can be seen that the results obtained are very similar to curve provided by the company. This suggests that the extrapolated geometric dimensions reliable.

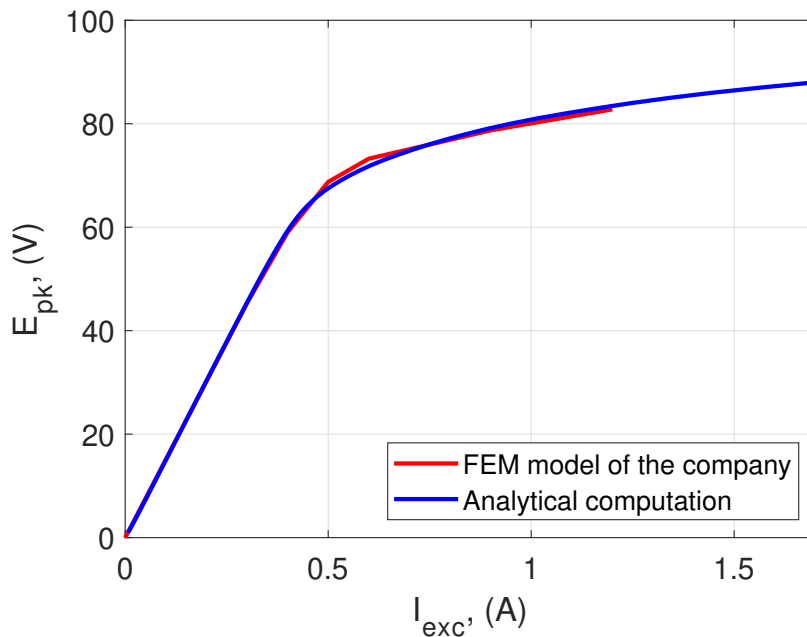


Figure 2.10: Comparison of the computed no-load characteristic and that obtained by the company by means of FEM simulations for  $n = 2000\text{rpm}$ .

At this point of the investigation there is no reason to believe that the extrapolated model differs from the real motor. By the way, there are other checks that need to be done in order to confirm the reliability of the model. Hence, at first the finite element analysis is used to keep on adjusting the model and once all the results are considered satisfactory, the FEM model is employed for the comparison.

## 2.3 FEM Model

Once the model has been confirmed by the correspondence of the no-load characteristics, it can be implemented on the software Flux. A first sketch of the machine is created, drawing the geometry of the motor. In order to make the simulations faster, the periodicity of the machine is exploited and consequently only one-sixth of the whole machine is modeled. All the simulations are intended to be transient magnetic 2D simulations. Below a brief description of the implementation of the machine's model is presented, by subdividing it into four different parts: the stator, the air gap, the rotor and the circuit. The structure description does not correspond to the order used to create the model in the software.

### 2.3.1 The stator

In the section "Geometry" of the software, some parameters are defined (such as the outer diameter of the stator, the dimensions of slots and teeth and so on) and based on these, the stator is designed and all the faces built. In section "Mesh" some mesh points and mesh lines are defined in order to get a denser mesh in correspondence of the teeth. In section "Physics" two materials are created: copper and the iron provided by the company. The first one is used for the winding, while the second one for the stator itself. The same materials will be used in the rotor. As seen in 2.1.1, the number of stator slots is 54 and, since only one-sixth of the machine is designed, the number of visible slots in the model is, therefore, 9 (three per each phase). This means that instead of having six different regions for the winding (three phases, positive and negative), only three are needed. The sequence chosen to be represented is "AAAcccBBB", where capitol letters stand for positive orientation of the current in the region, while lowercase letters for negative. Based on what explained so far, six face regions are created in the software. The first one is the stator itself, named "STATOR" and set as laminated iron, by means of the created iron material. Here is is also required the thickness of the sheet iron (0.35 mm) and the stack factor (0.97). Then the three regions related to the winding are created by using the copper material. These are: "PHASE\_C\_N", "PHASE\_A\_P", "PHASE\_B\_P". Finally, a fifth region is needed for the wedges of the slots

("WEDGE") and a sixth one for the preslots ("PRESLOT"). These last two regions are set as "Air or vacuum region". Moreover, for what concerns the three coils, they need to be linked to a circuit, which is described below. Finally, each region has to be correctly assigned to the faces. The final result is shown in Figure 2.11.

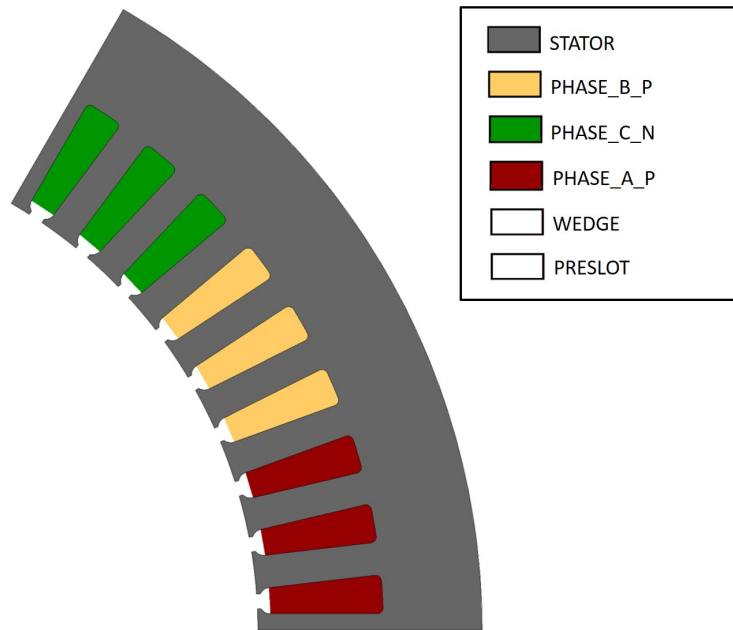


Figure 2.11: FEM model of the stator.

All the regions showed in this figure are considered part of the stator, hence their movement is forbidden. As a consequence, for each region the mechanical set has to be static.

### 2.3.2 The air gap

Since most of the magnetic energy is stored in the air gap of the machine and important torque calculations are related to the air-gap field solution, it is essential to correctly mesh this part of the model. A common approach is to divide the air gap into three different parts, with the aim of getting a denser mesh in that area. Hence two circumferences are drawn between the rotor and the stator. Of these three air gap sections, two are decided to be fixed with the stator, one rotates with the rotor. Therefore other two face regions have been created and assigned: "AIR\_ROTATOR" and "AIR\_STATOR". Both of these types of region are set

to "Air or vacuum region" and specific mesh points and lines are created specifically for the lines in the air gap and the elements close to it too.

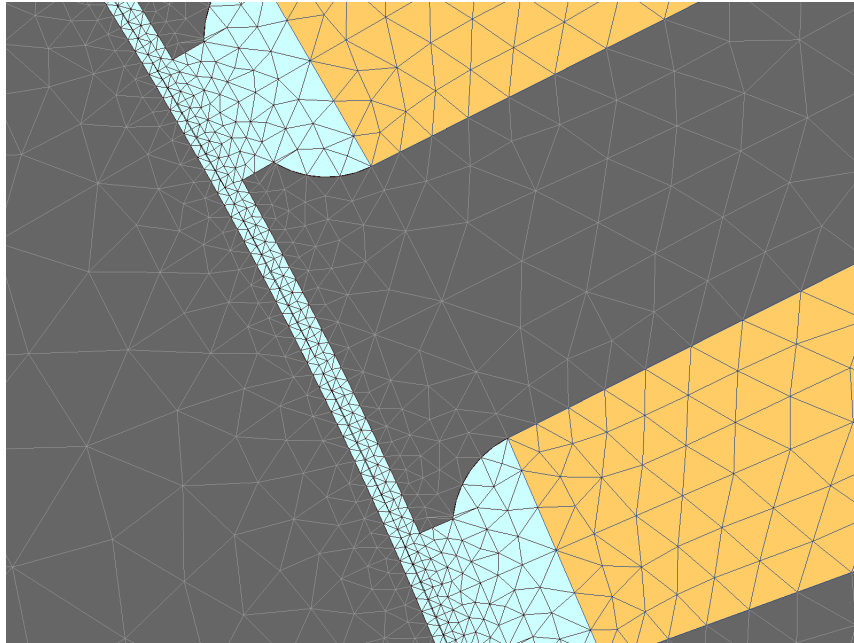


Figure 2.12: FEM model of the air gap.

As it can be seen from Figure 2.12, the results show a dense mesh in the correspondence of the of the air gap region.

### 2.3.3 The rotor

As for the stator, the rotor is modeled by using the dimensions showed in Figure 2.2. The geometry is drawn by means of the definition of new parameters, which are also correlated to the parameters already defined for the stator. Once the geometry is set, the faces are built and meshed. In section "Physics" other three face regions are created: "ROTOR", "FIELD\_P", "FIELD\_N". The region "ROTOR" does not differ from the face region "STATOR", except for the mechanical setting, that must be "rotating". The face regions "FIELD\_P" and "FIELD\_N" are related to the excitation winding, and they represent the conductors with respectively positive and negative orientation of the current in the region. Again, these two regions must be assigned to a coil of the circuit, described later. In Figure 2.13, the finite element model of the rotor is shown. In designing the rotor pole, a first attempt is made by

assuming its shape to be an arc of circumference (whose center does not correspond to the center of the machine).

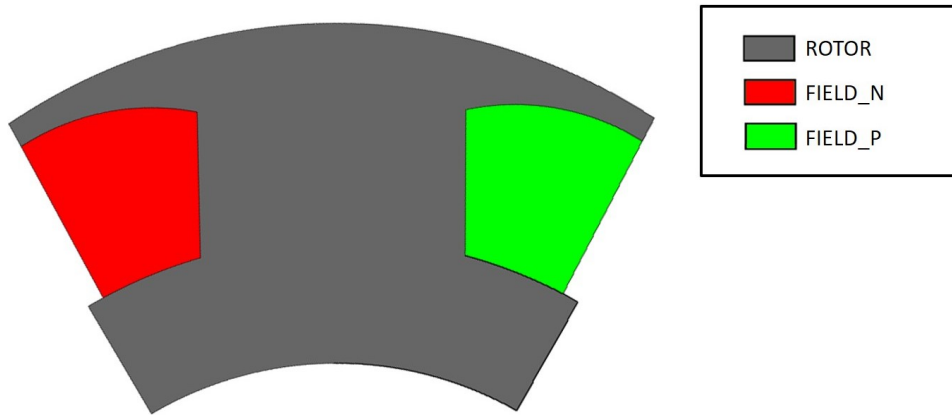


Figure 2.13: FEM model of the rotor of the salient pole machine.

At this point, the model is completed and the first simulation can be run. Firstly, a simulation at no-load is made and this allows to further confirm the model through a comparison of the simulated no-load voltage with the provided one. Results show that the no-load voltage shape is different from the measured one. Indeed, as it can be seen from Figure 2.4, it is clear that the measured voltages at no-load are very close to sinusoidal curves. The reason of this difference can be found in the uncertainty about the length of the air gap in the edge of the pole. Indeed, even though the minimum air gap is known to be 0.5 mm, it is not easy to extrapolate from Figure 2.2 the exact value of the edge air gap. Some simulations at no-load for different values of the latter, for one excitation current and at a certain speed are run in order to have a no-load voltage as closer as possible to the provided one. The parameter sweep is shown in Figure 2.14. The value of the edge air gap length equals to 0.5 mm corresponds to a constant value of the air gap length, or equivalently that the center of the pole periphery circumference coincides with the machine center. In this condition, the voltage at no-load is more affected by the presence of the stator slots. As the edge air gap length rises, the disturb is less visible.

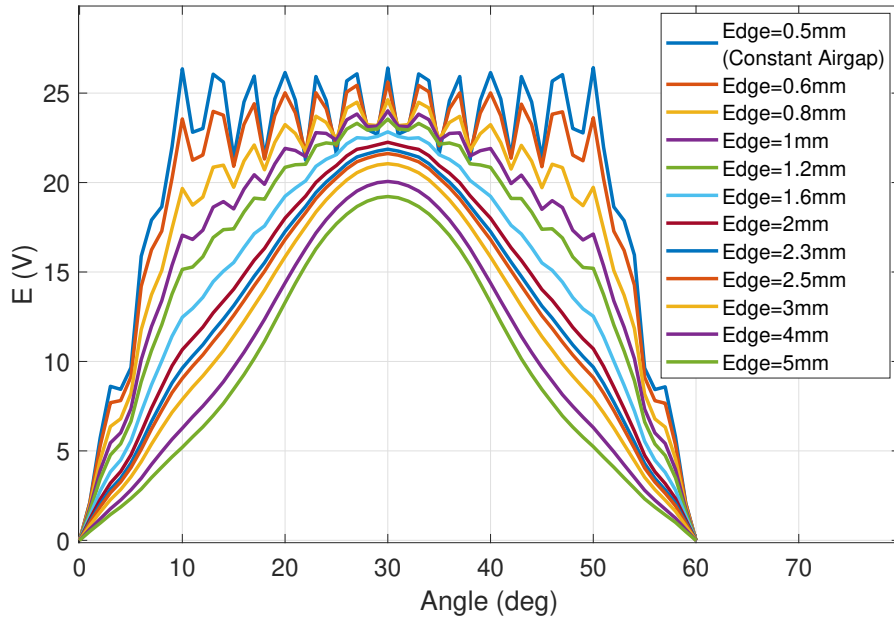


Figure 2.14: Effect of the rotor pole shape on the no-load voltage.

In any case, since none of the curves seems to resemble a sine, another shape of rotor pole is assumed. As most of the synchronous machine design books state [26], it is very common to design the pole shape as the inverse of the cosine function of the electric angle. The angle is taken as in Figure 2.15, which means from the axis of symmetry of the pole, referred to the center of the machine.

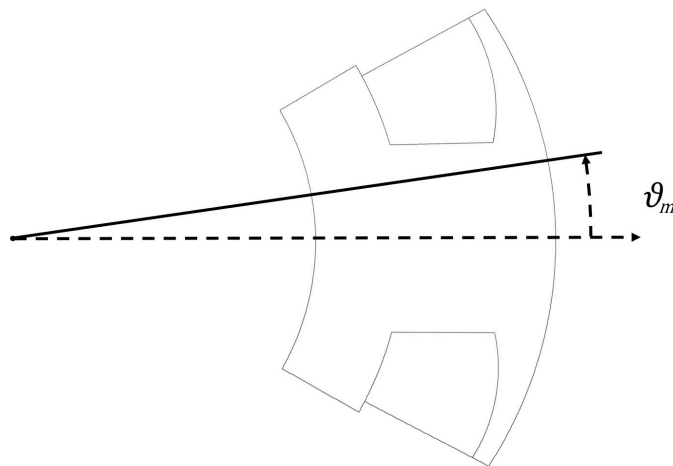


Figure 2.15: Reference angle for designing the rotor pole.

Thus, the air gap can be expressed as a function of this angle:

$$\delta = \frac{\delta_0}{\cos(\theta_e)} \quad (2.25)$$

Where  $\delta_0$  is the minimum air gap, and  $\theta_e = \theta_m \cdot p$ . Based on this construction, a new rotor shape is obtained and showed in Figure 2.16.

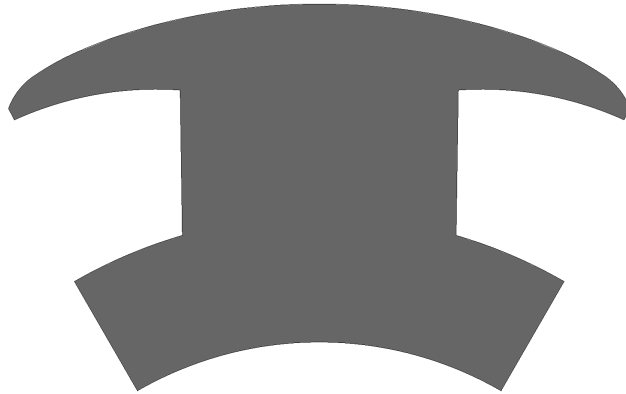


Figure 2.16: New rotor pole shape of the salient pole machine.

At this point, another simulation is run and the resulting no-load voltage is showed in Figure 2.17. Since the results are satisfactory, it is assumed the second option to be the final shape of the rotor pole.

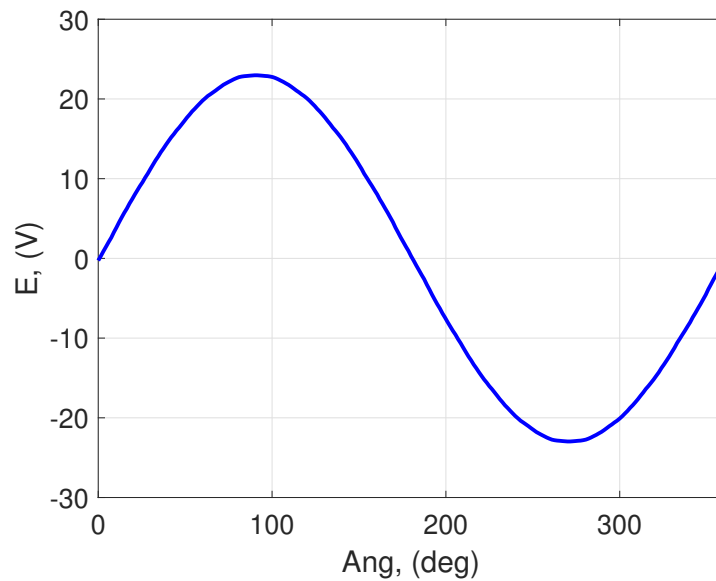


Figure 2.17: Voltage at no-load obtained with the new rotor pole shape.

### 2.3.4 The circuit

In transient magnetic simulations, an electric circuit describing the power supply of the machine is coupled with the actual field solution. Therefore, all the face regions that represent a coil need to be coupled with the circuit. For this purpose, four coil conductors (three for the stator and one for the rotor) are created in section "circuit".

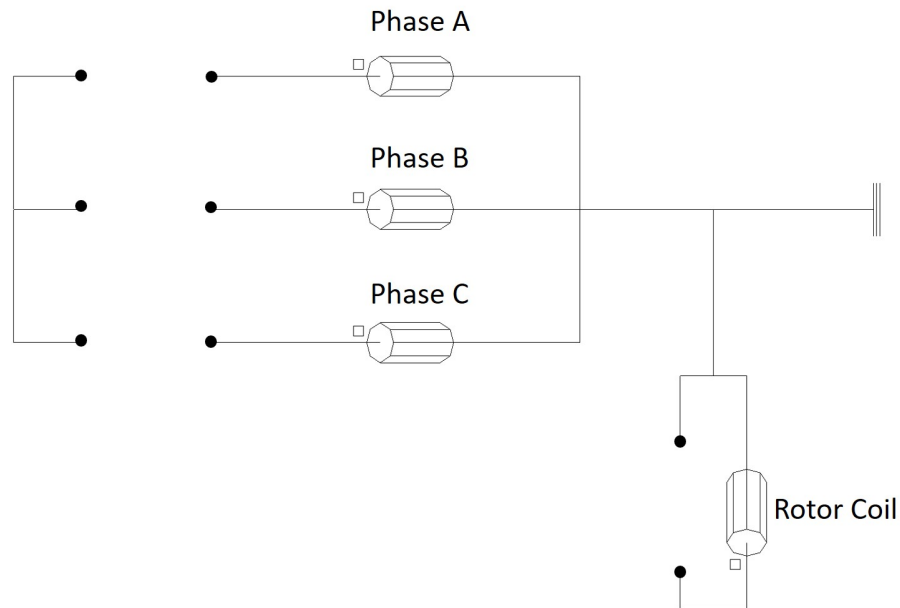


Figure 2.18: Equivalent circuit used for FEM simulations.

All the information required about the winding are inserted in the correspondent face region in section "coil conductor region component". For example, in face region "PHASE\_A\_P", this is set to "COIL\_A", which is the coil "Phase A" showed in Figure 2.18. Moreover, always in the face region the number of turns of the conductors (21), the filling factor (0.5) and the number of circuits in parallel (3) are inserted. However, no simulation can be run unless the circuit showed in figure is closed. When there is the need to supply the stator (or the rotor), it is common not to use voltage generators, but current generators. This is convenient because it is possible to avoid for the transient to end, and to directly feed the motor in steady state. In addition, the information on how to feed the machine is usually given by current references.

## 2.4 No-Load Characteristic

Once the model is completed, the no-load characteristic can be obtained via finite element simulations. This is important because the geometry of the model was assumed to be correct based on the matching of the computed no-load curve and the one provided by the company. To confirm that, an appropriate setting of simulation is prepared. First of all, the circuit needs to be modified in order to replicate the no-load scenario. For this purpose, three big resistances are put in series with the coils. The value of each one of them is  $10^{12}\Omega$ , that is high enough to consider as if the winding is left open. For what concerns the rotor, it is supplied through a current generator as previously suggested. The value of the current on the generator is set to be parametric. What said is shown in the following figure.

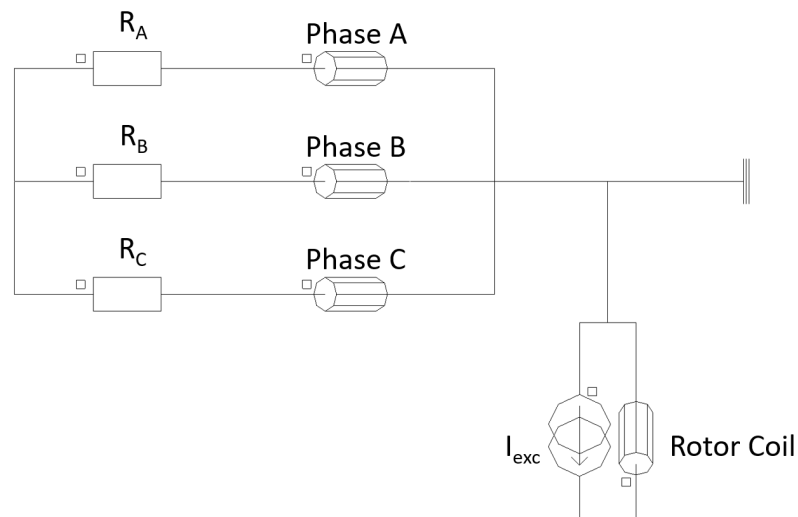


Figure 2.19: Equivalent circuit used for FEM simulations at no-load.

The speed is set to 2000 rpm, in order to make a consistent comparison with the no-load characteristic of Figure 2.5. Finally, in section "Solver" of the software an appropriate scenario of simulation is created. There, the mechanical final position has to be chosen, as well as the number of the steps desired to reach it. Moreover, the software allows to control other parameters. Hence, the excitation current in the rotor is controlled to vary from 0.1 A

to 1.6 A with a step of 0.1 A. For each excitation current the phase voltage is plotted and his spectrum computed. Finally, 16 couples  $(I_{exc}, E_{pk})$  are obtained and plotted in the following figure together with the no-load characteristic provided from the company. As it ca be seen, the curves are very similar to each other.

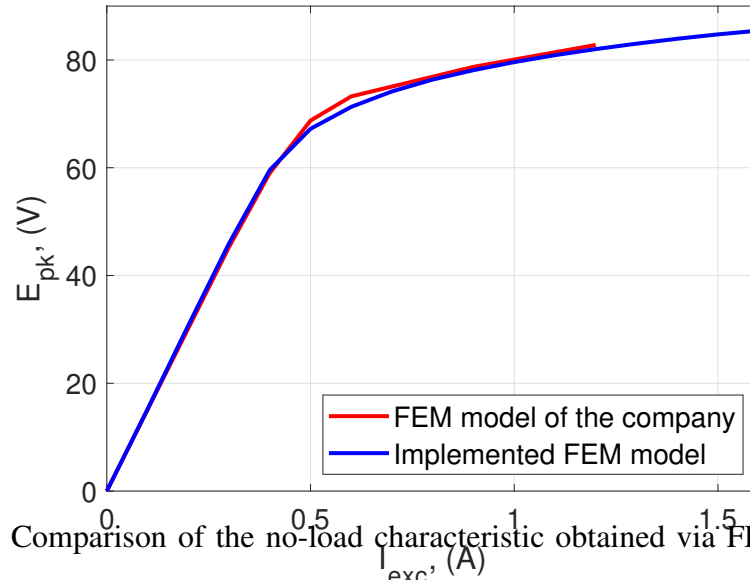


Figure 2.20: Comparison of the no-load characteristic obtained via FEM simulations and that obtained via FEM simulations by the company.

Finally the obtained magnetic flux density in the air gap at no-load is showed in the following figure.

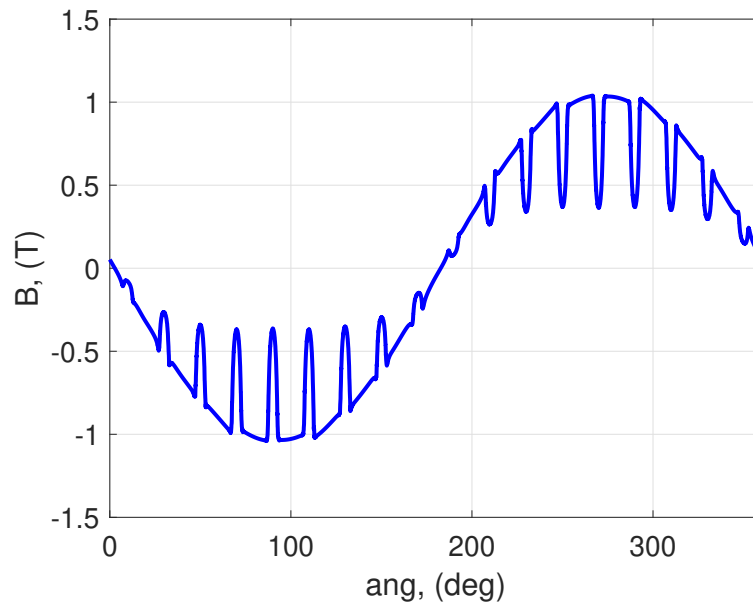


Figure 2.21: Magnetic flux density in the air gap obtained via FEM simulations for the salient pole machine.

## 2.5 Simulations at Load

Based on the information provided by the company, three working points are known with their respective torques. Again, to check the reliability of the model, these three working points are simulated. Generally speaking, a synchronous machine is working at load when both stator and rotor are fed and the rotor is rotating. In passing from a no-load condition to a load condition, i.e. supplying the stator, three currents start to flow in the stator windings. These three currents generate a rotating magnetic field. All the phenomena that come from the interaction between this magnetic field and the excitation magnetic field are generally called "armature reaction". In this condition, the voltage in the stator coils depends on the total flux, which can be strongly different in its phase and amplitude from the excitation field. It can be proved that, as long as the no-load voltage vector is behind the stator current vector (with motor references), the overall effect of the armature reaction is a demagnetization of the machine. The extent of the demagnetization depends on the displacement between the two vectors. The vector diagram of the condition mentioned above is showed in Figure 2.22.

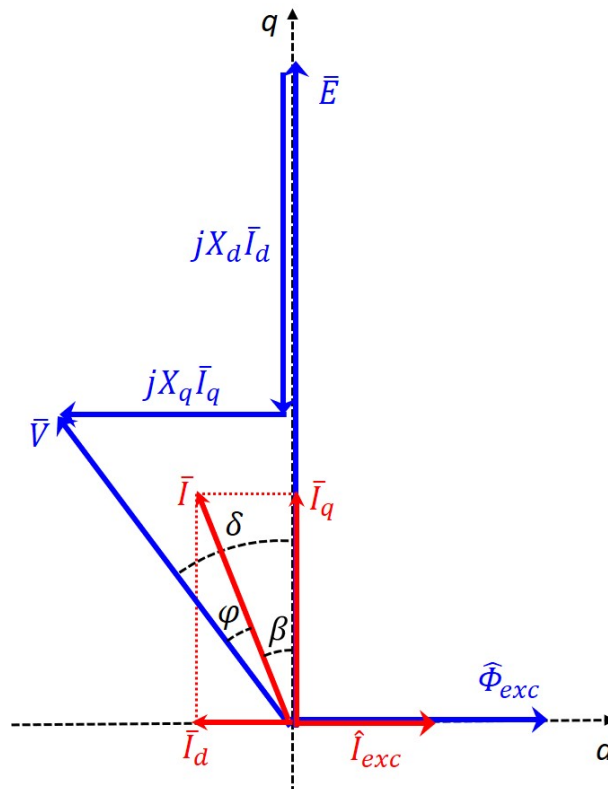


Figure 2.22: Vector diagram at load of the salient pole machine.

At load and in steady state conditions, the motor delivers an electromagnetic torque that can be computed by means of the following formula.

$$T = \frac{1}{\omega_r} \left[ \frac{E \cdot V \cdot \sin \delta}{X_d} + \frac{1}{2} \frac{X_d - X_q}{X_d \cdot X_q} V^2 \sin 2\delta \right] \quad (2.26)$$

Hence, the resulting couple depends on the displacement between the no-load voltage and the voltage at load, as well as their magnitudes and the machine parameters. In order to simulate the motor at load, again the circuit in Figure 2.18 needs to be modified. In order to supply power to the stator, current generators are used. For what concerns the rotor winding nothing changes with respect to no-load simulations. To reach the purpose, it is convenient not to feed the stator with three current generators, because there is the risk of causing numerical errors by imposing the currents in three coils in star connection. Indeed the third current will be automatically computed by means of the other two.

$$i_c = -(i_a + i_b) \quad (2.27)$$

Then, the used circuit can be seen in Figure 2.23.

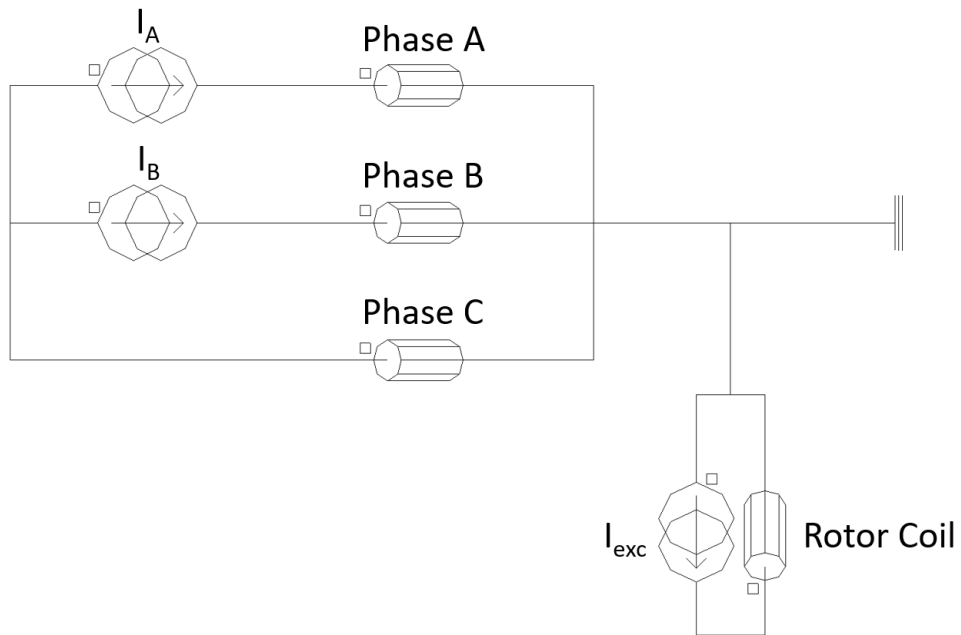


Figure 2.23: Equivalent circuit used for FEM simulations at load.

It is decided to supply the stator by means of the currents in (d,q) frame. Therefore, two new parameters are created "I\_D" and "I\_Q". Since the power supply can only happen in the (a,b,c) frame, then a way to pass from dq components to abc components must be implemented in the software. To reach the goal, the parameters "I\_ALPHA" and "I\_BETA" are created. Their values are computed by means of the inverse Park transformation, in which the modules of the vectors do not change because of the transformation. The angle needed for the transformation is the electric angle, which is obtained in the software by multiplying the variable "ROTATING", which represents the rotor position, by the number of pole pairs.

$$\begin{bmatrix} i_\alpha \\ i_\beta \end{bmatrix} = \begin{bmatrix} \cos \theta_e & -\sin \theta_e \\ \sin \theta_e & \cos \theta_e \end{bmatrix} \cdot \begin{bmatrix} i_d \\ i_q \end{bmatrix} \quad (2.28)$$

At this point, it is necessary to obtain the values of the currents in (a,b,c) frame, based on the computed values of  $i_\alpha$  and  $i_\beta$ . Here the inverse Clarke transform is used.

$$\begin{bmatrix} i_a \\ i_b \\ i_c \end{bmatrix} = \begin{bmatrix} 1 & 0 & \frac{1}{3} \\ -\frac{1}{2} & \frac{\sqrt{3}}{2} & \frac{1}{3} \\ -\frac{1}{2} & -\frac{\sqrt{3}}{2} & \frac{1}{3} \end{bmatrix} \cdot \begin{bmatrix} i_\alpha \\ i_\beta \\ i_o \end{bmatrix} \quad (2.29)$$

Assuming that the homopolar component of the current is equals to zero ( $i_a + i_b + i_c = 0$ ) and remembering that only two current generators are used to feed the stator, then these are:

$$\begin{cases} I_A = I\_ALPHA \\ I_B = -\frac{1}{2} \cdot I\_ALPHA + \frac{\sqrt{3}}{2} \cdot I\_BETA \end{cases} \quad (2.30)$$

The position of dq axes must be correctly identified. The direction of the d-axis corresponds to the direction of the field created only by the rotor winding, while the q-axis is displaced of  $90^\circ$ . This means that the no-load voltage lies on the q-axis, since it is the derivative of flux when the stator is not powered. Thus, a simulation at no-load is run and one at load keeping the same excitation current too. The latter is made by putting the  $I_d$  current equals to zero and supplying only with  $I_q$ . The no-load voltage and the  $I_q$  are not in phase, which also

means that is incorrect to call the current  $I_q$ . Hence to fix the problem or the initial position of the rotor is changed in order to put move the no-load voltage vector either the variable "ROTATING" is adjusted in the transform by adding an offset. The latter is chosen as the solution to the issue. The displacement angle is computed, since both the no-load voltage vector and the current vector are known and inserted in the rotation matrix.

$$\begin{bmatrix} i_\alpha \\ i_\beta \end{bmatrix} = \begin{bmatrix} \cos(\theta_e + \theta_i) & -\sin(\theta_e + \theta_i) \\ \sin(\theta_e + \theta_i) & \cos(\theta_e + \theta_i) \end{bmatrix} \cdot \begin{bmatrix} i_d \\ i_q \end{bmatrix} \quad (2.31)$$

Where the value of the angle needed is  $\theta_i$ , and it is equals to:

$$\theta_i = -30^\circ \quad (2.32)$$

In Figure 2.24 the no-load voltage and the phase current are plotted before inserting  $\theta_i$  (a) and after (b). As it can be seen in the second situation the two variables are in phase.

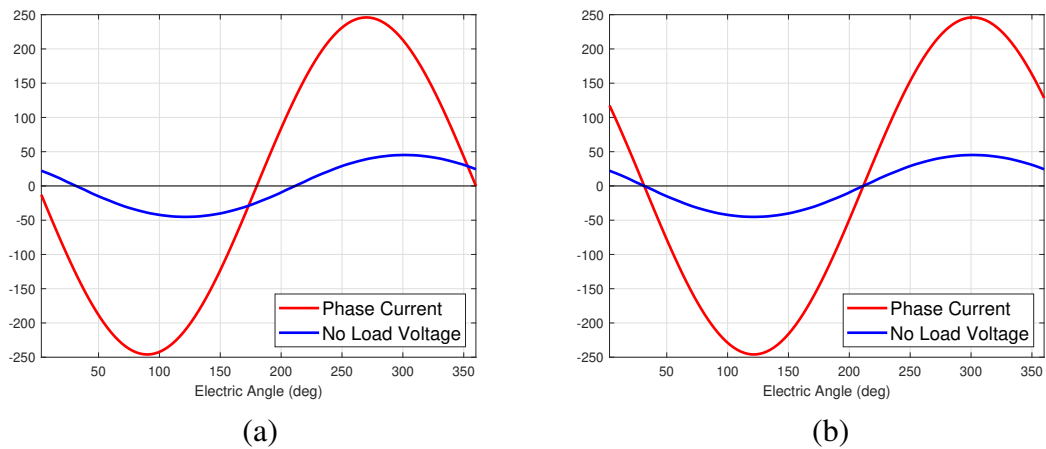


Figure 2.24: Back electromotive force and phase current for a stator current only in q-direction before the adjustment (a) and after (b).

Now, the model is ready to be simulated at load. The three working points are simulated and reported below.

**Working points**

The three working points provided by the company are all with a value of the current in the direct axis equals to zero. This means that the vector diagram for each of these working point can be qualitatively explained by the following figure.

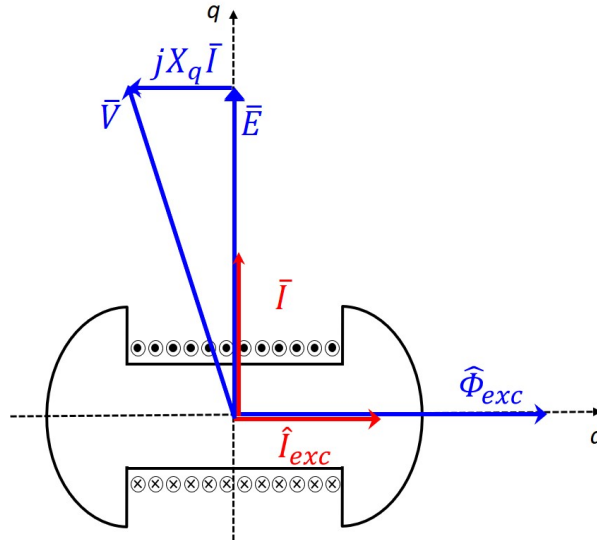


Figure 2.25: Electro-magnetic torque WP1

The current vector is placed on the q-axis. By supplying the motor as suggested from Table 2.5, the torques are obtained and compared to the expected values. The results are shown in Figure 2.26, while the values of the average obtained torques and the expected ones are shown in the following table.

	WP1	WP2	WP3
$T_{FEM}, (\text{Nm})$	112.4	253.6	367.9
$T_{Expected}, (\text{Nm})$	110	225	350

Table 2.6: Working points

As it can be seen, there is a slight difference between the two values. Again, it is essential to bear in mind that the goal of this thesis is not to build the model of the salient pole machine, but to have a basic and reasonable model for the comparison.

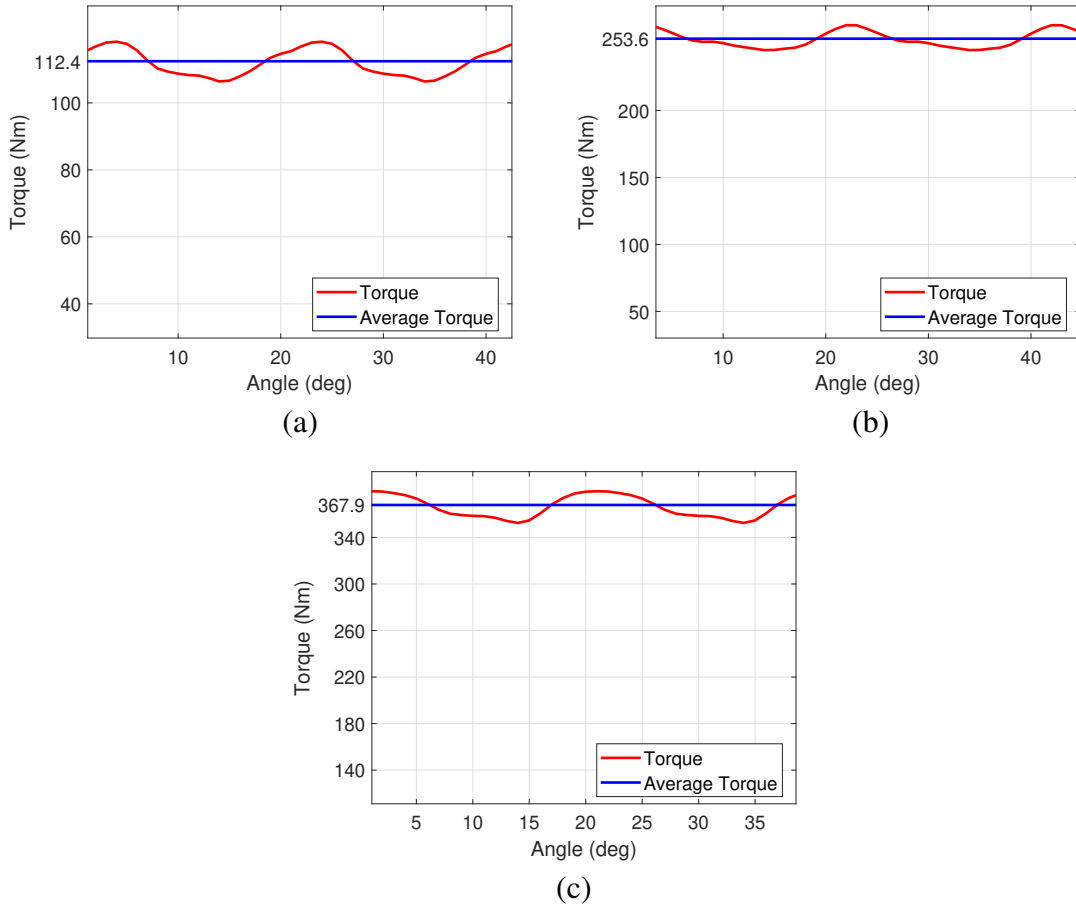


Figure 2.26: Torques for WP1 (a) WP2 (b) and WP3 (c)

Further, a color shaded magnetic flux density map has been found in the thesis. This is obtained by feeding the machine as proposed in WP2. Again, the reliability of the model is confirmed. A little difference can be seen in the area in which the armature reaction causes a rise on the magnetic flux density in the pole. This is probably due to the mesh of the machine in that area, since in the model of this thesis the corner between the pole head and the pole core is not filleted, while in the thesis [25] a smoother angle is used.

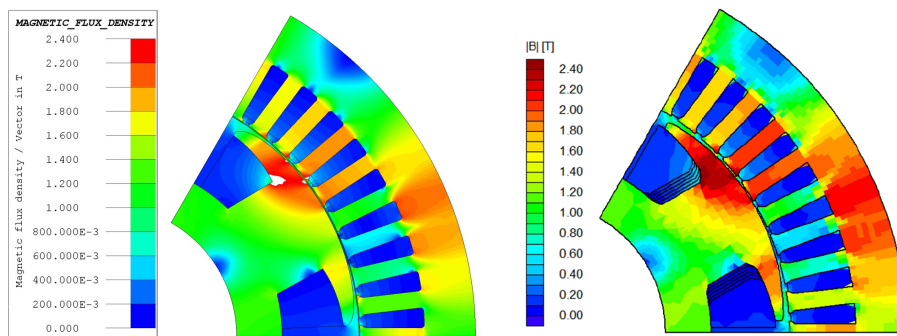


Figure 2.27: Magnetic flux density map for WP2 simulated (left) and from thesis [25] (right).

## 2.6 Main Parameters Computation

In this chapter the main parameters of the salient pole motor are computed. The values of both rotor and stator resistances are needed in order to make an analytical evaluation of the Joule losses and to be set in the FEM software if a correct value of the phase voltage is desired. Moreover, also the inductances are computed in order to make a comparison with the parameters of the cylindrical rotor. Indeed, it is expected an evident difference on the magnetizing inductance of the q-axis, as the salient pole is an anisotropic machine and the cylindrical rotor an isotropic one. The values of the inductances are confirmed by FEM simulations.

### 2.6.1 Analytical Computation

#### Stator Resistance

The stator winding DC resistance can be computed as:

$$R_s = N_s \cdot \rho \cdot \frac{L_s}{N_p \cdot S_c} \quad (2.33)$$

Where  $L_s$  is the total length of one turn of the stator coil,  $S_c$  its cross-sectional surface and  $\rho$  its resistivity ( $0.017 \frac{\Omega \text{mm}^2}{\text{m}}$  @20°C).

Since it is known the stator filling factor and the area of the stator slot, the area occupied only by copper can be obtained simply by multiplying these two values. Further, it is also known the number of conductors per slot ( $Z$ ). Then, the surface of each conductor can be computed as follows:

$$S_c = \frac{S_s \cdot k_{fs}}{Z} \quad (2.34)$$

The length  $L_s$  of each turn is considered twice of the sum of the axial length of the machine and the end winding length, as it can be seen in Figure 2.28.

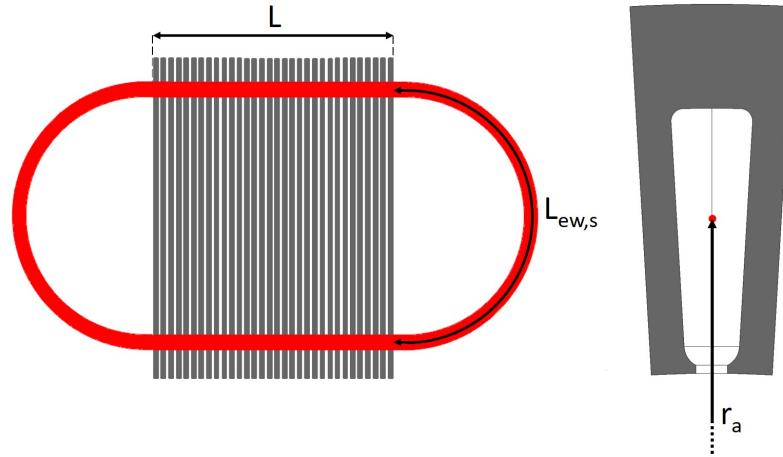


Figure 2.28: Lateral view of the machine (left) and reference for the computation of the end windings length (right).

Hence:

$$L_s = 2(L + L_{ew,s}) \quad (2.35)$$

Where  $L_{ew}$  is the end winding length that can be computed as explained below, referring to Figure 2.28.

$$L_{ew,s} = k_{ew} \cdot \frac{\pi \cdot r_a}{p} \quad (2.36)$$

Being  $r_a$  the distance between the center of the machine and the center of the stator slot, and  $k_{ew}$  a factor that takes into account the shape of the end winding. The latter can vary between 1.45 and 1.7. Here it has been chosen a value of 1.6 which is almost equals to  $\pi/2$ , that means to consider a circular shape. Finally, by means of equation (2.33), the stator phase resistance is computed.

$$R_s = 9.2 \text{ m}\Omega \quad (2.37)$$

### Rotor Resistance

A similar procedure is adopted to compute the rotor resistance. For each pole, the total coil area is known, as well as the filling factor. Dividing the total copper area by the number of

rotor turns, the surface of each conductor is obtained.

$$S_r = \frac{S_t \cdot k_{fr}}{N_r} \quad (2.38)$$

The length of the end winding is obtained by referring to Figure 2.29.

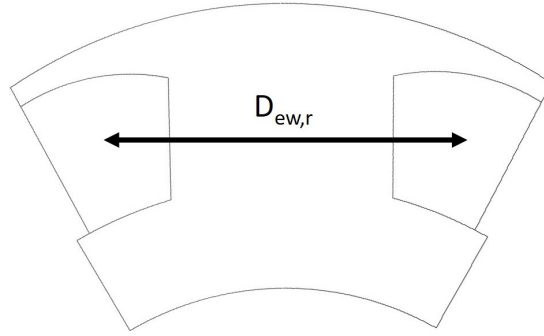


Figure 2.29: Reference for the computation of the end rotor winding length for the salient pole machine.

Again by means of the factor  $k_{ew}$ , which is chosen to be the same of that used for the stator winding, the end winding length is computed.

$$L_{ew,r} = k_{ew} \cdot D_{ew,r} \quad (2.39)$$

The total length is the double of the sum of the active length of the machine and the previously computed end winding's length. Thus the rotor resistance is obtained.

$$R_r = 2p \cdot N_r \cdot \rho \cdot \frac{L_r}{S_r} = 142 \Omega \quad (2.40)$$

### Leakage Inductance

The component of the magnetic flux that does not take part in the electro-mechanical power transformation is called leakage flux. It can be caused by different reasons and one of them is the slot leakage flux. This is due to all the lines of the magnetic field the cross the slot. In this work, only this kind of leakage flux is considered. The slot leakage inductance ( $L_\sigma$ ) is the parameter that allows to take into account this phenomenon. It mainly depends on the

slot shape and on the winding arrangement. Its analytical formulation is presented below.

$$L_{\sigma} = \mu_0 \cdot L_p \frac{N_{ss}}{m} \cdot \left(\frac{Z}{a}\right)^2 \cdot \lambda \quad (2.41)$$

Here  $\lambda$  is the permeance factor and it only depends on the shape of the slot. To compute  $\lambda$ , the stator slot shape has been approximated as showed in the following figure.

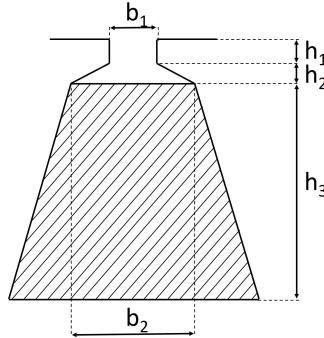


Figure 2.30: Reference for the leakage inductance computation.

The permeance factor can be obtained as follows.

$$\lambda = \frac{h_3}{3 \cdot b_2} + \frac{h_1}{b_1} + \frac{h_2}{b_2 - b_1} \cdot \log \frac{b_2}{b_1} \quad (2.42)$$

Finally, this value is incremented by a factor of 1.1, in order to partially overcome the underestimation of the leakage inductance.

$$L_{\sigma} = 34.5 \mu\text{H} \quad (2.43)$$

### Magnetizing Inductances

The air gap of a salient pole synchronous motor varies along the circumferential coordinate. In particular, the biggest difference can be found between the air gap in the direct and quadrature directions. As a consequence, the inductances in d-axis and in q-axis are expected to be different. In this perspective, two different equivalent air gaps can be defined: one used to compute the d-axis inductance ( $L_d$ ) and the other used to compute the q-axis inductance ( $L_q$ ).

As it can be seen from equation (2.25), the function of the air gap length behaves as the inverse of cosine function. To be more accurate, also the Carter factor must be included in this evaluation. Assuming to supply the stator with a peak current  $\hat{I}$  in the d-axis, the resulting mmf is:

$$\hat{A} = \frac{3}{\pi} \cdot q \cdot Z_c \cdot \hat{I} \quad (2.44)$$

Therefore, the magnetic flux density at the electric position  $\theta_e$  (indicated in Figure 2.15) is:

$$B_d(\theta) = \frac{\mu_0}{\frac{\delta_0}{\cos(\theta_e)} \cdot k_c} \cdot \hat{A} \cdot \cos(\theta_e) = \frac{\mu_0}{\delta_0 \cdot k_c} \cdot \hat{A} \cdot \cos^2(\theta_e) \quad (2.45)$$

Assuming:

$$\hat{B} = \frac{\mu_0}{\delta_0 \cdot k_c} \cdot \hat{A} = \frac{\mu_0}{\delta_0 \cdot k_c} \cdot \frac{3}{\pi} \cdot q \cdot Z_c \cdot \hat{I} \quad (2.46)$$

By substituting in equation (2.45):

$$B_d(\theta_e) = \hat{B} \cdot \cos^2(\theta_e) \quad (2.47)$$

Therefore the air gap flux density is proportional to the square of the cosine, when the ampere turns created by the stator are in the d-axis. To obtain the inductance on the d-axis of the fundamental, a cosine function of an equivalent flux can be found if the following constrain is respected.

$$\hat{B} \int_{-\pi/2}^{\pi/2} \cos^2(\theta_e) d\theta = \hat{B}_{1d} \int_{-\pi/2}^{\pi/2} \cos(\theta_e) d\theta \quad (2.48)$$

In this way, the factor of the fundamental of the Fourier series can be obtained. Indeed:

$$\hat{B}_{1d} = \frac{\pi}{4} \cdot \hat{B} = \frac{\pi}{4} \cdot \frac{\mu_0}{\delta_0 \cdot k_c} \cdot \hat{A} \quad (2.49)$$

Finally, the required equivalent air gap in the d-axis can be found as:

$$\delta_d = \frac{4}{\pi} \cdot \delta_0 \cdot k_c \quad (2.50)$$

Referring to [27], the direct axis magnetizing inductance can be computed as:

$$L_{md} = \frac{m}{2} \cdot \frac{2}{\pi} \cdot \mu_0 \cdot \frac{1}{2p} \cdot \frac{4}{\pi} \cdot \frac{\tau}{\delta_d} \cdot L_p \cdot (k_w \cdot N_s)^2 \quad (2.51)$$

The obtained value is:

$$L_{md} = 1.45 \text{ mH} \quad (2.52)$$

Therefore, the total inductance in the d direction can be found as the sum of the leakage inductance and the magnetizing one.

$$L_d = L_{md} + L_\sigma = 1.49 \text{ mH} \quad (2.53)$$

For what concerns the inductance in q-direction, a similar procedure can be applied with the assumption to supply the stator with the current in the q-axis. Nevertheless, the air gap in q-direction is more complicated to compute, since the law of variation of the air gap length is not as well defined as in the d-axis. Anyway, according to [27], it varies typically between  $(1.5 - 2 - 3) \cdot \delta_d$ . So it is assumed that:

$$\delta_q = \frac{\delta_d}{2} \quad (2.54)$$

The analytical computation of the quadrature axis magnetizing inductance is now exactly the same of that of the direct axis, with the only exception that  $\delta_d$  has to be replaced with  $\delta_q$ .

$$L_{mq} = 0.73 \text{ mH} \quad (2.55)$$

Again the total inductance in the q direction can be found by summing the magnetizing inductance and the leakage inductance.

$$L_q = L_{mq} + L_\sigma = 0.76 \text{ mH} \quad (2.56)$$

## 2.6.2 Computation by Simulation of the Inductances

The values of the inductances can be beneficially confirmed by some simulations. To reach the goal, the stator is supplied with different current values ( $\hat{I}$ ), once in the direct direction and once in the quadrature direction. The chosen values of the current must avoid to cause the saturation of the machine, since the value of the unsaturated inductance  $L_d$  would be compromised. They are chosen from 0 up to 70 A, with a step value of 5 A. For each one, the values of the flux density in d- and q-direction are obtained.

$\hat{I}$ , (A)	10	20	30	40	50	60	70
$\hat{B}_d$ , (T)	0.11	0.23	0.35	0.46	0.58	0.68	0.77
$\hat{B}_q$ , (T)	0.06	0.12	0.18	0.25	0.31	0.37	0.43
$\hat{B}_q/\hat{B}_d$	0.54	0.54	0.53	0.53	0.53	0.54	0.56

Table 2.7: Values of fundamentals of the magnetic flux density in the air gap for different stator currents in the salient pole machine.

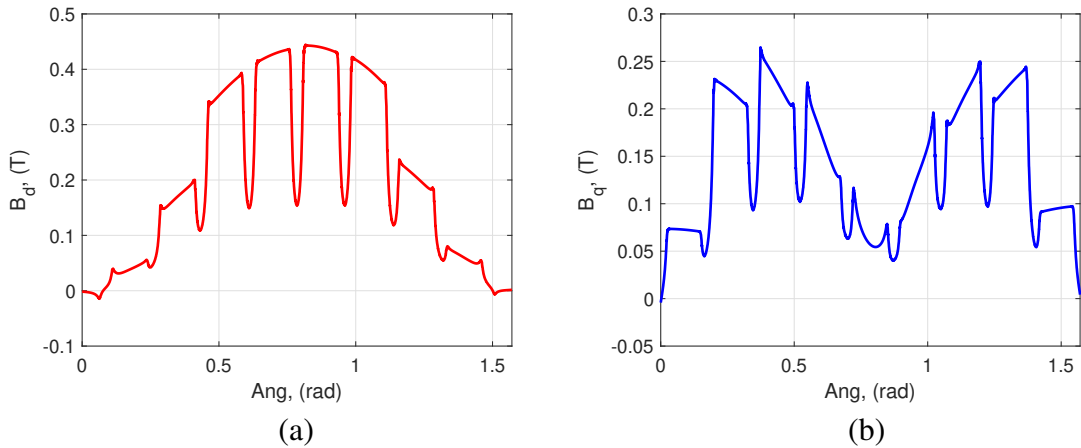


Figure 2.31: Magnetic flux density for a stator current vector of 30 A placed in d-axis (a) and q-axis (b).

Therefore, the inductances in the two axes for each current can be easily extrapolated as follows:

$$L_d = \frac{2}{\pi} \cdot \frac{k_w \cdot N_s \cdot \tau \cdot L_p \cdot \hat{B}_d}{\hat{I}} \quad (2.57)$$

$$L_q = \frac{2}{\pi} \cdot \frac{k_w \cdot N_s \cdot \tau \cdot L_p \cdot \hat{B}_q}{\hat{I}} \quad (2.58)$$

By averaging the values obtained for each current, the two inductances are:

$$L_d = 1.51 \text{ mH} \quad (2.59)$$

$$L_q = 0.81 \text{ mH} \quad (2.60)$$

As it can be seen the ratio between the two value is not that far from the hypothesized one from equation (2.54).

## 2.7 Losses and Efficiencies

As emphasized in Chapter 1, a great advantage of the WFSM is the possibility to control the excitation field, by controlling the current in the rotor. Hence, a third variable is available, in addition to the two degrees of freedom of the stator current components in d- and q-direction (or equivalently the magnitude and phase of the stator current vector). Finding the optimal combination of  $I_d$ ,  $I_q$  and  $I_{exc}$  of this kind of motor is, therefore, not elementary and in any case it exceeds the purpose of this thesis. However, in the doctoral thesis [25], this topic has been studied and the combinations of the current triplets for each torque and speed have been obtained. This allows to run some simulations by means of the information on the currents provided by the thesis with two different aims: to further confirm the salient pole model by comparing torques and efficiencies with the doctoral thesis ones, and to have a base for the future comparison with the cylindrical rotor machine. To unequivocally determine these three variables, three equations are needed. The first one comes from the desired torque constraint, which can be obtained from the following formula.

$$T = \frac{3}{2} \cdot p \cdot (\lambda_d \cdot i_q - \lambda_q \cdot i_d) \quad (2.61)$$

Obviously equation (2.61) is equivalent to (2.26) in steady state. The second condition is given by the flux. Indeed, it is convenient to maximize it as long as the maximum voltage is reached. Then it has to be decreased proportionally with the speed. These two conditions represent the usual constraints used to control a PM motor. The presence of the variable  $I_{exc}$  allows to introduce an additional constraint that can be arbitrarily chosen. The proposed approach by the reference thesis, that can also be found in literature [12], is to control the power factor. This results from a trade-off between reducing the current in the stator and in the inverter by keeping the power factor as high as possible and minimizing the rotor Joule losses. Indeed, in order to increase the power factor, more current has to be injected in the rotor winding. Thus, it is stated that the triplets have been chosen in order to "maximize the efficiency of the whole system, that is from the battery to the motor shaft". These values are reported in the following tables, which are taken from the thesis and rearranged. The sign

convention of the currents is the same adopted in Figure 2.22.

		$I_q, (A)$												
TORQUE, (Nm)	240	390	390	390	390									
	220	383	383	383	380	320								
	200	383	383	383	383	310								
	180	345	345	345	345	290	257							
	160	308	308	308	308	290	242							
	140	270	270	270	270	255	220	200						
	120	231	231	231	231	220	200	180	175	163				
	100	193	193	193	193	193	185	165	150	145	140			
	80	155	155	155	155	155	145	145	134	125	118	113	105	
	60	120	120	120	120	120	120	115	110	100	93	90	87	
	40	85	85	85	85	85	85	85	85	85	75	65	65	60
	20	45	45	45	45	45	45	45	45	45	45	45	45	45
	10	30	30	30	25	25	25	25	25	25	25	25	25	25
		1000	2000	3000	4000	5000	6000	7000	8000	9000	10000	11000	12000	
		SPEED, (rpm)												

		$I_d, (A)$											
TORQUE, (Nm)	240	-130	-130	-130	-130								
	220	-90	-90	-90	-90	-250							
	200	-35	-35	-35	-35	-220							
	180	-35	-35	-35	-35	-170	-300						
	160	-34	-34	-34	-34	-140	-270						
	140	-30	-30	-30	-30	-100	-220	-290					
	120	-28	-28	-28	-28	-70	-190	-240	-300	-360			
	100	-25	-25	-25	-25	-40	-130	-190	-240	-300	-360		
	80	-20	-20	-20	-20	-20	-90	-150	-193	-240	-280	-320	-360
	60	-10	-30	-40	-50	-70	-80	-100	-135	-165	-200	-240	-260
	40	-10	-10	-20	-30	-40	-50	-60	-80	-110	-130	-150	-170
	20	-10	-30	-40	-50	-50	-60	-60	-60	-60	-60	-80	-80
	10	-10	-20	-30	-40	-50	-50	-50	-50	-50	-50	-50	-50
		1000	2000	3000	4000	5000	6000	7000	8000	9000	10000	11000	12000
		SPEED, (rpm)											

		$I_{exc}, (A)$												
TORQUE, (Nm)	240	6.3	6.3	6.3	6.3									
	220	5.4	5.4	5.4	5.4	6.3								
	200	4.6	4.6	4.6	4.6	5.6								
	180	4.2	4.2	4.2	4.2	4.9	6.2							
	160	3.8	3.8	3.8	3.8	4.1	5.3							
	140	3.5	3.5	3.5	3.5	3.55	4.5	5.5						
	120	3.2	3.2	3.2	3.2	3.2	3.9	4.6	5.2	6.2				
	100	2.8	2.8	2.8	2.8	2.8	3	3.6	4.3	5	5.7			
	80	2.4	2.4	2.4	2.4	2.4	2.5	2.9	3.3	3.8	4.3	4.9	5.5	
	60	1.9	1.9	1.9	2	2	2	2.2	2.4	2.8	3.2	3.7	4	
	40	1.4	1.5	1.5	1.5	1.5	1.5	1.5	1.6	1.9	2.2	2.4	2.6	
	20	1	1.1	1.1	1.1	1.1	1.1	1.1	1.1	1.1	1.1	1.1	1.2	1.2
	10	0.8	0.8	0.8	0.8	0.9	0.9	0.9	0.9	0.9	0.9	0.9	0.9	0.9
		1000	2000	3000	4000	5000	6000	7000	8000	9000	10000	11000	12000	
		SPEED, (rpm)												

Figure 2.32: Supplying tables of the salient pole machine from pag.51 of [25].

For these combinations of  $I_d$ ,  $I_q$  and  $I_{exc}$ , the following measured efficiency chart has been obtained, for a temperature of about 70 °C and a DC battery voltage of 400 V.

Torque, (Nm)	240	82.24	89.52	92.11	93.54								
	220	83.31	89.63	92.54	93.79	93.82							
	200	83.36	90.12	92.56	93.99	94.21							
	180	84.58	90.89	93.09	94.35	94.52							
	160	85.82	91.54	93.61	94.60	94.67	93.87						
	140	87.27	92.41	94.06	94.78	95.17	94.45						
	120	87.86	92.69	94.16	95.13	95.48	94.94	94.34	93.19				
	100	89.21	93.41	94.82	95.15	95.55	95.12	94.58	93.80	92.51	91.14		
	80	90.22	93.77	94.62	95.24	95.44	95.28	94.86	93.92	92.70	91.70	90.56	
	60	91.52	94.10	95.32	95.02	95.37	95.15	95.02	94.08	93.36	92.34	91.39	91.15
	40	92.35	94.03	94.66	95.41	94.89	94.69	94.60	93.91	93.16	92.81	91.77	90.68
	20	91.92	93.13	93.43	93.73	93.66	92.56	92.43	91.57	90.93	87.53	90.29	89.49
		1000	2000	3000	4000	5000	6000	7000	8000	9000	10000	11000	12000
Speed, (rpm)													

Figure 2.33: Salient pole machine efficiency map from pag.50 [25]

As stated in section 2.1.1, the salient pole motor analyzed in this work differs from the one presented in thesis [25] in the number of rotor turns. Therefore, to correctly supply the rotor, an adaptation of the  $I_{exc}$  currents showed in tables 2.32 needs to be done. To reach the scope, the ampere turns are kept the same when passing from one machine to the other. Hence, to get the correct values of the excitation currents, these are scaled as showed in equation (2.62).

$$I_{exc} = \frac{400}{843} \cdot I_{exc,t} \quad (2.62)$$

Where  $I_{exc,t}$  represents all the values of the excitation current reported in Figure 2.32, while  $I_{exc}$  represents the adapted values used to feed the rotor in the simulations and showed below.

I <sub>exc</sub> (A)													
TORQUE, (Nm)	240	2.99	2.99	2.99	2.99								
	220	2.56	2.56	2.56	2.56	2.99							
	200	2.18	2.18	2.18	2.18	2.66							
	180	1.99	1.99	1.99	1.99	2.33	2.94						
	160	1.80	1.80	1.80	1.80	1.95	2.51						
	140	1.66	1.66	1.66	1.66	1.68	2.14	2.61					
	120	1.52	1.52	1.52	1.52	1.52	1.85	2.18	2.47	2.94			
	100	1.33	1.33	1.33	1.33	1.33	1.42	1.71	2.04	2.37	2.70		
	80	1.14	1.14	1.14	1.14	1.14	1.19	1.38	1.57	1.80	2.04	2.33	2.61
	60	0.90	0.90	0.90	0.95	0.95	0.95	1.04	1.14	1.33	1.52	1.76	1.90
	40	0.66	0.71	0.71	0.71	0.71	0.71	0.71	0.76	0.90	1.04	1.14	1.23
	20	0.47	0.52	0.52	0.52	0.52	0.52	0.52	0.52	0.52	0.52	0.57	0.57
	10	0.38	0.38	0.38	0.38	0.43	0.43	0.43	0.43	0.43	0.43	0.43	0.43
	1000	2000	3000	4000	5000	6000	7000	8000	9000	10000	11000	12000	
SPEED, (rpm)													

Figure 2.34: New excitation current values adapted for the considered number of rotor turns.

Of all these operating points, six are selected in order to be simulated.

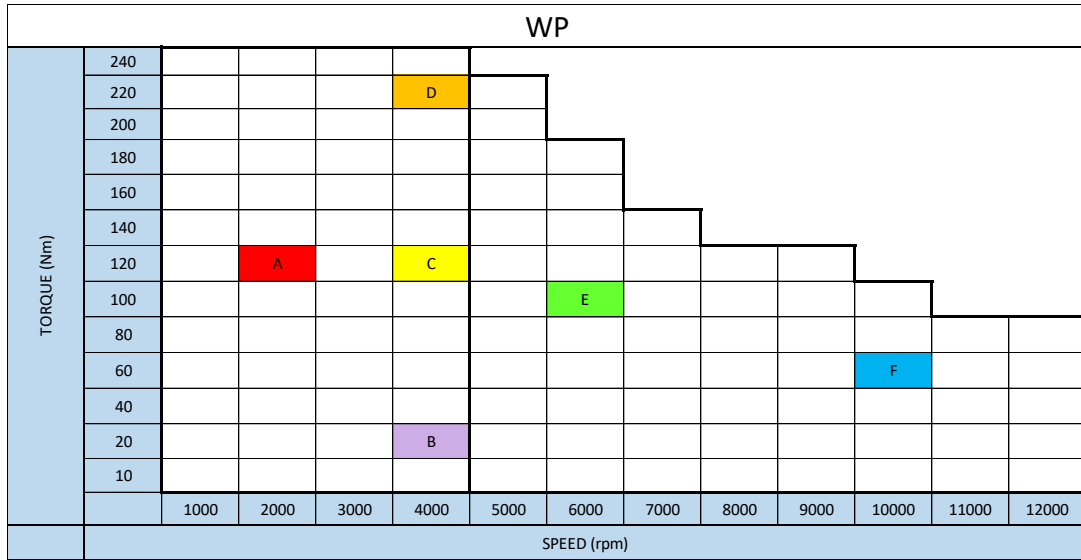


Figure 2.35: Selected working points to be simulated for the salient pole machine.

As it can be seen from Figure 2.35, four points are selected below the base speed, while the two belonging to the flux weakening region are chosen on the same constant power curve. For each selected working point the stator and the rotor are supplied as explained above and the torque is obtained. Moreover, since the control strategy adopted is to keep the power factor to high values, also the current and the phase voltage are plotted and, by means of a spectrum analysis, the power factor is computed from their first harmonic phase shift. Finally, also the value of the phase voltage peak is obtained, in order to verify not to exceed the voltage limits.

	WPA	WPB	WPC	WPD	WPE	WPF
TORQUE, (Nm)	134.1	18.2	134.1	241.9	108.8	59.1
EXPECTED TORQUE, (Nm)	120.0	20.0	120.0	220.0	100.0	60.0
TORQUE RIPPLE, (%)	7%	4%	7%	7%	5%	6%
PEAK VOLTAGE, (V)	93.1	77.0	183.5	198.1	213.5	189.9
$\cos(\phi)$	0.9	1.0	0.9	0.9	1.0	1.0

Figure 2.36: Results obtained from FEM simulation for each selected working point of the salient pole machine.

As it can be seen, a maximum error of about 10% can be found on the obtained torque. The results have been discussed with the company. Again, since there are uncertainties on which motor prototype has been tested and reported at page 50 of the thesis, the obtained values can be reasonably considered valid and consistent. Also, the obtained power factor is greater than 0.9 in all the simulated working points, which confirms the adopted supply strategy. Finally, the highest voltage respects the voltage limit (see equation (2.1)).

### Efficiencies Computation

The following step is to obtain the efficiency of the motor in each working point and to compare it to the ones in Table 2.33. The efficiency can be computed as follows:

$$\eta = \frac{P_{out}}{P_{out} + P_J + P_{fe} + P_m} \quad (2.63)$$

Where  $P_{out}$  is the mechanical output power, computed as:

$$P_{out} = T \cdot \omega_r \quad (2.64)$$

While  $P_J$ ,  $P_{fe}$  and  $P_m$  are respectively the Joule losses, the losses in iron mainly caused by hysteresis and eddy currents, and mechanical losses.

For what concerns the Joule losses, they can be divided into two contributes: one in the stator coil and one in the rotor coil.

$$P_J = P_{J,s} + P_{J,r} = 3 \cdot R_{s,70^\circ\text{C}} \cdot I^2 + R_{r,70^\circ\text{C}} \cdot I_{exc}^2 \quad (2.65)$$

Here, the current  $I$  is the rms value of the amplitude of the vector current obtained by knowing the two components  $I_d$  and  $I_q$ . While, the values of the resistances are obtained by adapting both resistances computed in 2.6.1 to the temperature declared in the caption of Table 2.33. This is made by means of the following law.

$$R_{s,70^\circ\text{C}} = R_s \cdot (1 + \alpha\Delta T) \quad (2.66)$$

Where  $\alpha$  is the temperature coefficient ( $0.0039\text{ }^{\circ}\text{C}^{-1}$ ) and  $\Delta T$  is the difference between  $70\text{ }^{\circ}\text{C}$  and  $20\text{ }^{\circ}\text{C}$ .

The iron losses can be computed by the software using the "Bertotti" method. According to this method, iron losses can be divided into three different parts: hysteresis losses, eddy current losses and excess losses. The Bertotti losses are explained in next equation:

$$P_{fe} = k_1 \cdot (B_{max}^{\alpha_1} \cdot f) + k_2 \cdot (B_{max} \cdot f)^{\alpha_2} + k_3 \cdot (B_{max} \cdot f)^{\alpha_3} \quad (2.67)$$

Where the first contribute represents the losses by hysteresis, the second the eddy current losses and the third the excess losses. The coefficient and the exponents are therefore:

- $k_1$  is the coefficient of losses by hysteresis;
- $k_2$  is the coefficient of eddy current losses;
- $k_3$  is the coefficient of losses in excess;
- $\alpha_1$  is the exponent of the classical losses;
- $\alpha_2$  is the exponent of the eddy current losses;
- $\alpha_3$  is the exponent of losses in excess;
- $f$  is the frequency;
- $B_{max}$  is the peak value of the magnetic flux density.

These values are obtained with the aim of minimizing the error between the iron losses curve provided by the data sheet of the material and the one resulting from Equation (2.67), for different frequencies. Once obtained, they are set in the software which will automatically compute the iron losses depending on the magnetic flux density and the frequency.

For what concerns the mechanical losses, the information is provided by the thesis itself. They are modelled using the following empirical expression:

$$P_m = a \cdot \omega + b \cdot \omega^2 + c \cdot \omega^3 \quad (2.68)$$

Where the three coefficients  $a$ ,  $b$  and  $c$  are reported in the thesis. Finally, this procedure is implemented for each working point and the obtained efficiencies are shown in the following table.

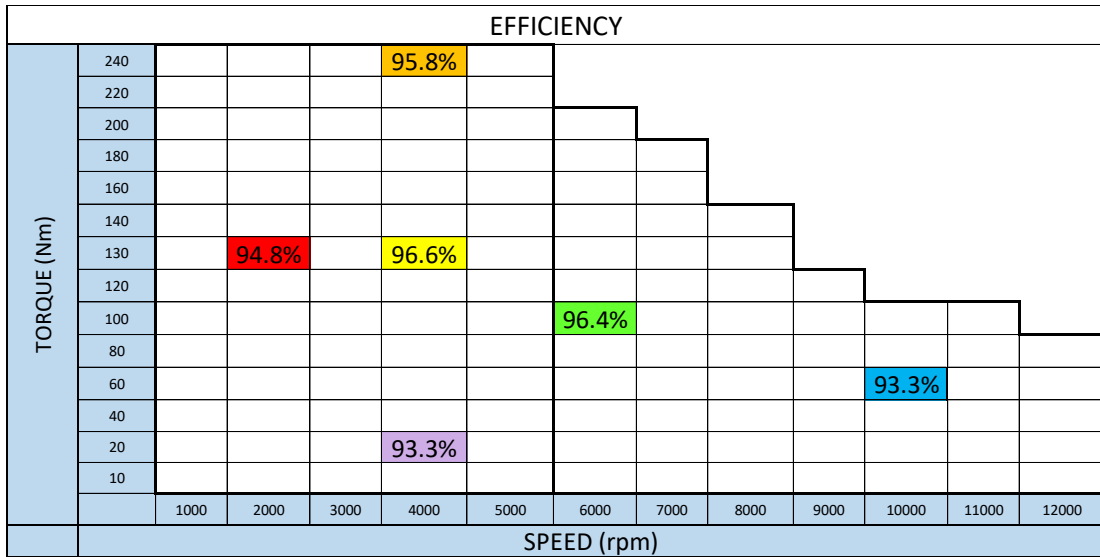


Figure 2.37: Obtained efficiencies of the six simulated working points of the salient pole machine.

The comparison with the values reported in thesis [25] is shown in the following table.

	WPA	WPB	WPC	WPD	WPE	WPF
SIMULATED MOTOR EFFICIENCY	94.8%	93.3%	96.6%	95.8%	96.4%	93.3%
THESIS MOTOR EFFICIENCY	92.6%	93.7%	95.0%	93.5%	95.1%	92.3%
DIFFERENCE	2%	0%	2%	2%	1%	1%

Figure 2.38: Comparison of the obtained efficiencies from FEM simulations to those reported in [25].

# Chapter 3

## Cylindrical Machine

### 3.1 Design Procedure

As discussed in Chapter 1, the goal of this work is to make a comparative analysis of two rotor configurations of a wound field synchronous motor for automotive application, by keeping the same stator. Of the two solutions, one is the salient prototype, that has been analyzed and improved in the doctoral thesis [25], and finally rebuild, in the previous chapter, based on the available information. Now, the other solution, i.e. the cylindrical rotor, needs to be designed and then compared to the salient pole one.

The interest in using a cylindrical rotor in electric vehicles mainly relies on the possibility to increase the mechanical resistance of the motor. It must be noticed that wound field machines have been historically employed as generators, which are a very well-known and established technology. For this reason, the basic principles for the design of the cylindrical rotor are taken from applications as alternators and adapted to this specific utilization. To confirm the advantage that could come from using a cylindrical rotor in traction motors, it should be pointed out that basically all turbogenerators, that need to reach high speeds to increase the efficiency of steam turbines, are equipped with cylindrical rotors. Therefore, although the salient pole design would be easier to make, cylindrical rotor is preferred when it comes to high speeds applications, as electric traction applications are.

As most of synchronous generators design books suggest, it is common to use the cylindrical rotor in 2- or 4-poles machines. Despite this, here a 6-pole machine is designed. The reason why this choice is made can be found on the constraint of not changing the stator, therefore the same number of poles is adopted for the design. Cylindrical rotors are usually slotted over  $2/3$  of the periphery and the slots are radial and open. Consequently, only one third of the periphery is left without slots and forms the so-called large tooth.

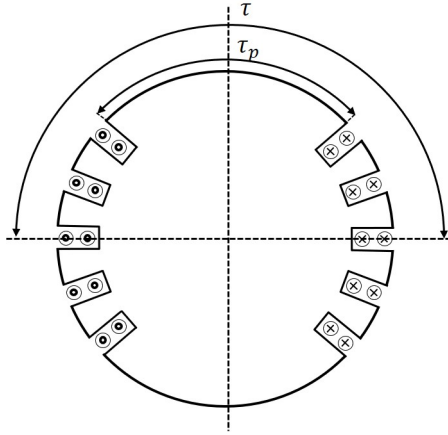


Figure 3.1: Usual design of the large tooth dimension for the cylindrical rotor machine.

Referring to Figure 3.1 and based on what previously said, the ratio between  $\tau$  and  $\tau_p$  is chosen to be  $1/3$ :

$$\frac{\tau_p}{\tau} = \frac{1}{3} \quad (3.1)$$

By fixating the extension of the large tooth, the slotted pitch can be obtained as follows:

$$\tau_r = \frac{\pi \cdot (D_{si} - 2 \cdot \delta_0) \cdot (1 - \tau_p/\tau)}{2p} = 0.057 \text{ m} \quad (3.2)$$

To write equation (3.2), the air gap length and consequently the outer rotor diameter are assumed to be those of the salient pole machine. Hence, the value of  $\tau_r$  represents the available space on the periphery to place the slots. The biggest number of rotor slots per pole that can reasonably fit in the remaining space is 8.

$$N_{rs} = 8 \quad (3.3)$$

In salient pole machines the flux density distribution mainly depends on the shape of the pole, which is usually built as the inverse of a cosine function to reduce the harmonics. Here, since the pole does not project, the flux density distribution depends on the rotor winding arrangement. For this reason it is usual not to make the rotor slots all of the same size. In particular, the two internal slots, i.e. the closest ones to the large tooth, are generally smaller in order to obtain a better shaped resulting magnetic flux density in the air gap. This constructive feature is adopted in the following design. Generally, the shorter tooth is chosen to be  $0.7 \div 0.8$  times the longer one. Referring to Figure 3.2, in which half of the rotor slots per pole are represented, it is chosen:

$$h = \frac{sh}{SH} = 0.8 \quad (3.4)$$

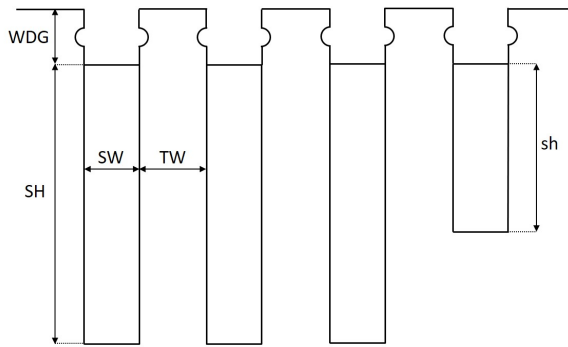


Figure 3.2: Design of the rotor slots of the cylindrical rotor machine.

Further, it is common to make the slot width and the tooth width equal. Again, this approach is thought for cylindrical rotors of alternators, that consequently have bigger dimensions in comparison to this specific one. Hence, it is chosen to increase the tooth width and then reduce the slot width in order not to have a too small dimension of the tooth in the base. In Figure 3.2, a linear transposition of the rotor periphery is showed, so that it is not that evident that in reality the value of TW is not constant but it decreases as coming closer to the machine center. Then all the values in Figure 3.2 have to be thought on the periphery of the rotor. Then the slot width is chosen to be  $2/3$  of the tooth width.

$$SW = 0.4 \cdot \frac{\tau_r}{N_{rs}} = 3 \text{ mm} \quad (3.5)$$

Now that the slot width is found, the missing equation to get the values of the slot heights is linked to electromagnetic requirements. According to [28], to design the excitation winding of synchronous generator cylindrical rotor, the rated field mmf is needed. At this design stage, this value is obviously unknown until the excitation field is designed. So it is generally assumed to be 2-2.5 times the rated stator mmf per pole. Nevertheless, this specific case is different, since the mmf generated by the salient pole rotor is known. Therefore, with the aim of getting similar performances of the two machines, the same rotor mmf of the salient pole is assumed for the cylindrical rotor. In particular, the ampere turns of the WP1 are taken as a reference for the design.

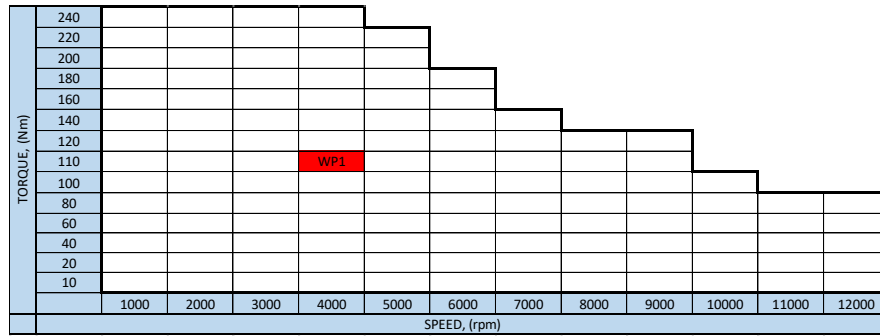


Figure 3.3: Selection of the working point of the salient pole machine used as a reference for the design of the cylindrical rotor machine.

In this working point the rotor ampere turns per pole are 843 At, with an excitation current of 1 A. Then, the current density for the WP1 is reasonably assumed to be 8 A/mm<sup>2</sup>. Then dividing the current in all the slots by the current density, the total surface of all the 8 slots is obtained. Since the excitation current is 1 A, by multiplying by 2 the ampere turns, the required total current is obtained. This has to be divided among the 6 long slots and the 2 short ones, and it can be done as follows:

$$\frac{2 \cdot A_{WP1}}{J} = S_{ls} \cdot (N_{rs} - 2) + 2 \cdot S_{ss} \quad (3.6)$$

Where,  $S_{ls}$  and  $S_{ss}$  are respectively the long slot surface and the short slot surface. These can be expressed as:

$$S_{ls} = SW \cdot SH \quad (3.7)$$

$$S_{ss} = SW \cdot sh = SW \cdot h \cdot SH \quad (3.8)$$

Substituting (3.7) and (3.8) into (3.6), the slot height SH ca be extrapolated.

$$SH = \frac{2 \cdot A_{WP1}}{J \cdot SW} \cdot \frac{1}{N_{rs} - 2 + 2 \cdot h} = 21 \text{ mm} \quad (3.9)$$

Finally, the slots are closed via wedges in order to ensure the conductors in the slots. There are 3mm long, so that the final total length of the slot is:

$$SH_{tot} = SH + WDG = 24 \text{ mm} \quad (3.10)$$

The final geometry is showed in the following figure.

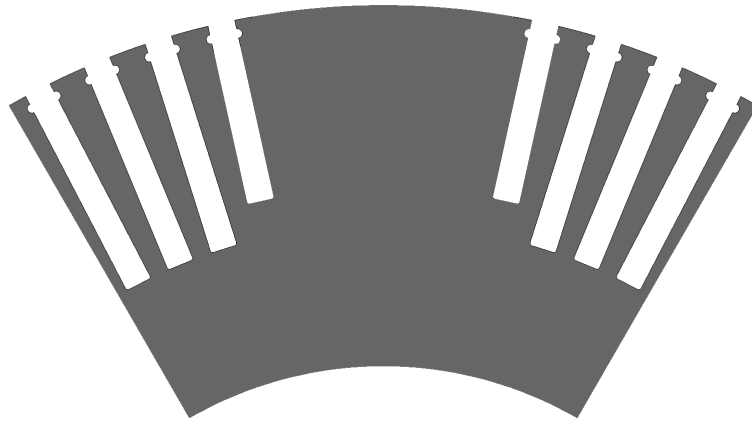


Figure 3.4: Final cylindrical rotor geometry.

### Excitation winding design

Once the rotor geometry project is completed, the excitation winding to be placed in the rotor slots has to be designed. First of all the number of rotor turns need to be found. As a first attempt, it seems reasonable not to change the number of turns in comparison to the salient pole machine. Again, because of the differences in the slot lengths, two different number of turns have to be thought for the two types of slots. Since the width is the same for each kind of slot, it can be said that the number of turns distribute proportionally with the slot height. Therefore, starting from a number of total turns per pole equals to 843, a number of

conductors equals to 843 has to be placed in 4 of the 8 slots. By calling  $N_{r,ls}$  the number of conductors in the long slots and  $N_{r,ss}$  the number of conductors in the short slot, the following expression can be written.

$$N'_r = N_{r,ss} + \left( \frac{N_{rs}}{2} - 1 \right) \cdot N_{r,ls} = N_{r,ls} \cdot h + \left( \frac{N_{rs}}{2} - 1 \right) \cdot N_{r,ls} \quad (3.11)$$

Where  $N_t$  is the number of total conductors in 4 slots. From equation (3.11), it is possible to obtain the number of conductors in each long slot.

$$N_{r,ls} = 221.8 \approx 222 \quad (3.12)$$

Consequently, the number of conductors in the short slot is:

$$N_{r,ss} = h \cdot N_{r,ls} = 177.6 \approx 177 \quad (3.13)$$

Which means that the total number of conductors of half of the slots per pole, and then the number of rotor turns per pole is:

$$N'_r = 3 \cdot N_{r,ls} + N_{r,ss} = 844 \quad (3.14)$$

Since the number of conductor is decided and the geometry too, the conductor diameter can be found. Assuming a rotor filling factor ( $k_{fr}$ ) of 0.45, the surface of one conductor is found.

$$S'_r = \frac{k_{fr} \cdot SW \cdot SH}{N_{r,ls}} = 0.13 \text{ mm}^2 \quad (3.15)$$

So that the diameter of the conductor can be obtained as follows:

$$D_r = \sqrt{\frac{4 \cdot S'_r}{\pi}} = 0.4 \text{ mm} \quad (3.16)$$

### 3.1.1 Check of Mechanical Stress

On high-speed cylindrical rotor machines, the conductors of the excitation winding are subjected to large centrifugal forces. The radial centrifugal forces acting on the field coils within the slots are transferred via wedges to the teeth and resisted by the rotor core yoke [29]. Here a simplified computation of the forces in the base of the teeth is proposed.

First of all, it is assumed that the machine is rotating at its maximum speed (12000 rpm), in order to consider the worst scenario of centrifugal forces. Then it is also assumed that, in the base of each tooth, three different centrifugal forces are acting. The first one is obviously the one acting on the tooth itself. Then, it is supposed that in each slot, the centrifugal forces on the copper are equally shared by the two adjacent teeth. This means that, for each tooth the centrifugal force of one slot has to be considered in the computation (resulting from the sum of the two adjacent slots). What said is explained by Figure 3.5. The third force to be considered is that of the end winding. Again, it can be imagined that one end winding centrifugal force is borne by two different teeth. To examine the worst condition, the longest end winding is computed. At this point, for each tooth, half of the end winding has to be included in the computation. By the way, considering that there are two end winding for each turn, then centrifugal force of a whole end winding is assumed acting on one tooth.

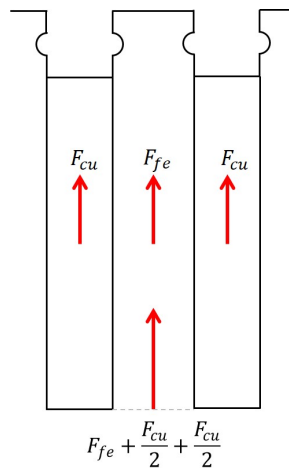


Figure 3.5: Centrifugal forces acting on the base of the tooth.

Generally speaking, the total centrifugal force can be expressed as follows:

$$F_c = m_t \cdot \omega_r^2 \cdot \frac{D_{si} - 2 \cdot \delta_0 - SH_{tot}}{2} \quad (3.17)$$

The total mass to be used in equation (3.17) is the sum of the iron of the tooth, the copper in one slot and the copper of in end winding. To get the values of the masses, the volume occupied by these three elements need to be computed. Since the rotor slots are radial, the surface of the slot itself can be assumed rectangular while the surface of the tooth trapezoidal. It is also assumed that the whole slot height is completely fill with copper. This will lead to a greater value of the centrifugal force but it will allow to have a certain margin of security.

Therefore:

$$m_{fe} = \left( \frac{(tw + SW) \cdot SH_{tot}}{2} \cdot L \right) \cdot d_{fe} \quad (3.18)$$

$$m_{cu,s} = (SH_{tot} \cdot SW \cdot L) \cdot d_{cu} \quad (3.19)$$

Where  $tw$  is the value of the tooth width in correspondence of the base and can be found by geometrical considerations, while  $d_{fe}$  and  $d_{cu}$  are respectively the density of the iron and of the copper.

For what concerns the end winding, the distance between the two external slots of Figure 3.4 is computed. This value ( $d_m$ ) is multiplied by  $k_{ew}$ , again imagining the end winding as the half of a circumference. In this way, the maximum total length of the end winding is computed ( $L_{ew,m}$ ) and therefore:

$$m_{cu,ew} = (SH_{tot} \cdot SW \cdot L_{ew,m}) \cdot d_{cu} \quad (3.20)$$

At this point, the mechanical stress on the base of the tooth is simply computed as:

$$\sigma = \frac{F_c}{L \cdot tw} = (m_{fe} + m_{cu,s} + m_{cu,ew}) \cdot \omega^2 \cdot \frac{D_{si} - 2 \cdot \delta_0 - SH_{tot}}{2} \frac{1}{L \cdot tw} = 80 \text{ MPa} \quad (3.21)$$

Since for a commercial M270-35A, the yield strength is 450 MPa and the tensile strength is 565 MPa, the obtained  $\sigma$  can be considered acceptable. By the way, this calculation

is approximated and further investigation on the mechanical stress should be carried on, possibly with a finite element software. Indeed, some coefficients greater than 1 are generally used in the edges of the slots to increase the value of  $\sigma$ , in order to take into account the correct distribution of the mechanical stress field. These coefficients depend on the shape of the slot and they are not considered in this computation.

## 3.2 FEM Model

Once the design of the cylindrical rotor is finally ended, a finite element model needs to be built up, following the steps of chapter 2. Since the stator is not changed, the same model used for the salient pole machine is used and adapted to the cylindrical rotor. To do it, the salient pole rotor is completely deleted and the cylindrical one is designed point by point, following the values obtained from the design. Once the geometry is drawn, the faces are built and a new rotor mesh is created. For what concerns the circuit and the phase regions, they are not deleted but employed in this new model. Therefore, "FIELD\_P" and "FIELD\_N" are assigned to the rotor slots. A new phase region is created specifically for the rotor wedges. The number of turns of the field coil is changed from 843 to 844.

The complete flux model is showed in the following figure.

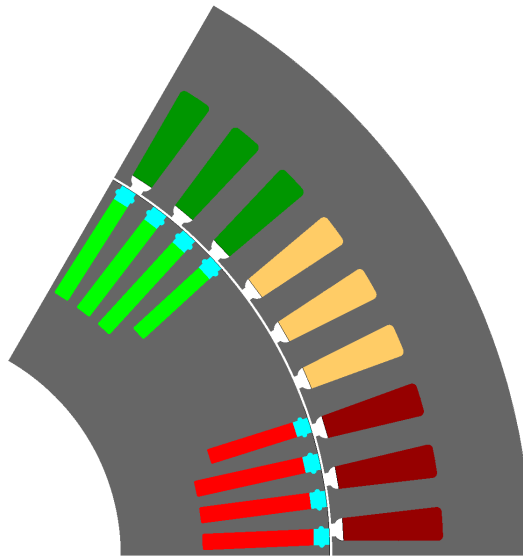


Figure 3.6: FEM model of the cylindrical rotor machine.

### 3.3 No-Load Characteristic

When injecting a continuous current in the rotor winding, the excitation field is created. The direction of the spacial vector of the excitation field coincides with the direction of the magnetic axis of the rotor winding. Hence, when the rotor rotates, so the excitation field does, together with the rotor.

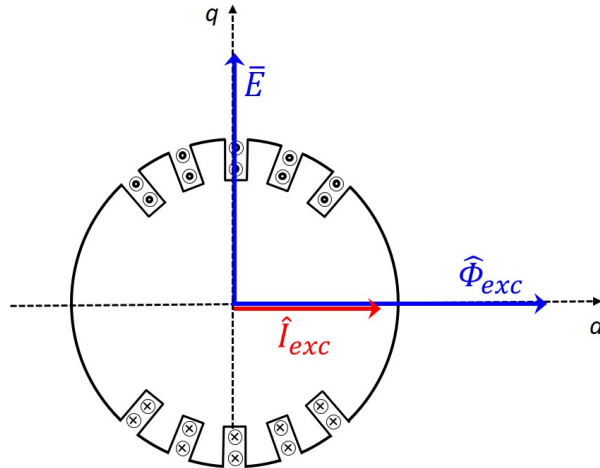


Figure 3.7: Vector diagram at no-load of the cylindrical rotor machine.

This leads to the induction of three sinusoidal emf, displaced of  $120^\circ$ . If the stator winding is left open, the induced emf vector is:

$$\bar{E} = -j(4.44 \cdot N_s \cdot f \cdot \hat{\Phi}_{exc}) \quad (3.22)$$

The value of the emf depends on the excitation current (because the flux is a function of the latter) and on the frequency. As it can be seen, the emf varies proportionally with the frequency, while generally no linearity can be observed with rising of the excitation field. Therefore, it is important to find the function  $E(I_{exc})$ , that is the no-load characteristic. To obtain this characteristic, the rotor is rotating at a given frequency, the stator winding is left open and the excitation current is gradually increased. The no-load characteristic of the cylindrical rotor machine is obtained by means of Flux. As already done for the salient pole motor, in the equivalent circuit of the machine three big resistances are put in series with the stator coils. The speed is set to 2000 rpm, and different values of the excitation current are injected in the rotor coil. Then for each one of them, the voltage in one coil is plotted.

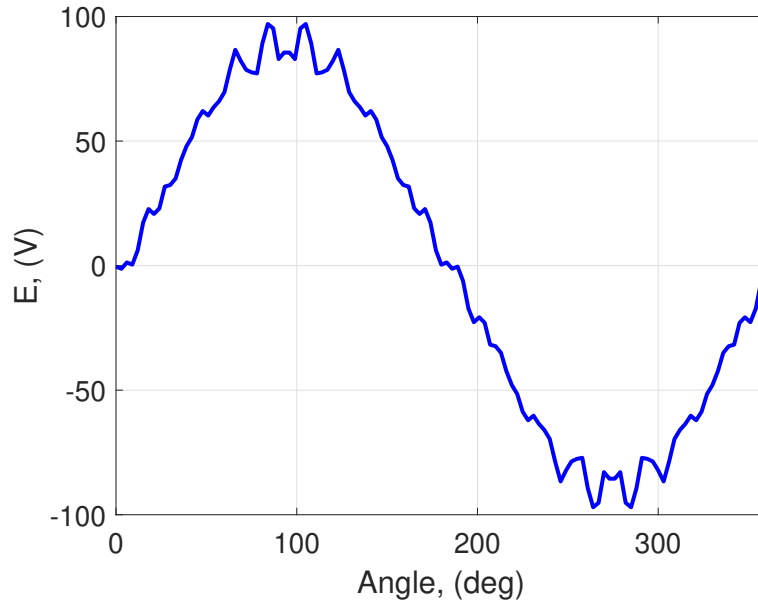


Figure 3.8: Voltage at no-load for  $n = 2000$  rpm,  $I_{exc} = 1$  A.

Then by plotting on the no-load voltages as a function of the excitation current, the no-load characteristic is obtained and showed in the following figure.

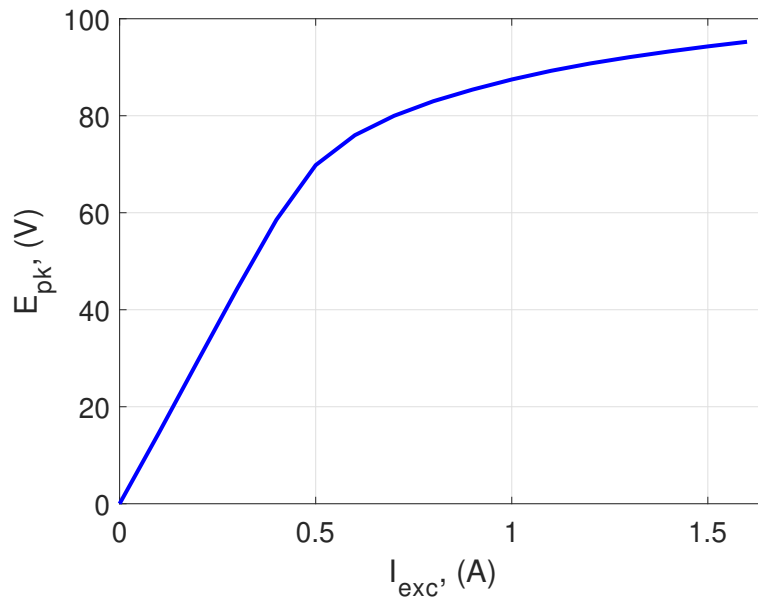


Figure 3.9: No-load characteristic obtained via FEM simulations for  $n = 2000$  rpm for the cylindrical rotor machine.

### 3.4 Simulations at Load

The working point 1 provided by the company is chosen in order to simulate the motor at load. Indeed the design procedure of the cylindrical rotor was based on this specific working point. Hence, the circuit is modified as suggested in Figure 2.23. Again the circuit is not changed with respect to the one used for the salient pole machine. The WP1 is characterized by current only in the q axis, whose value is 246 A. The diagram vector describing this supplying condition is shown in the following figure.

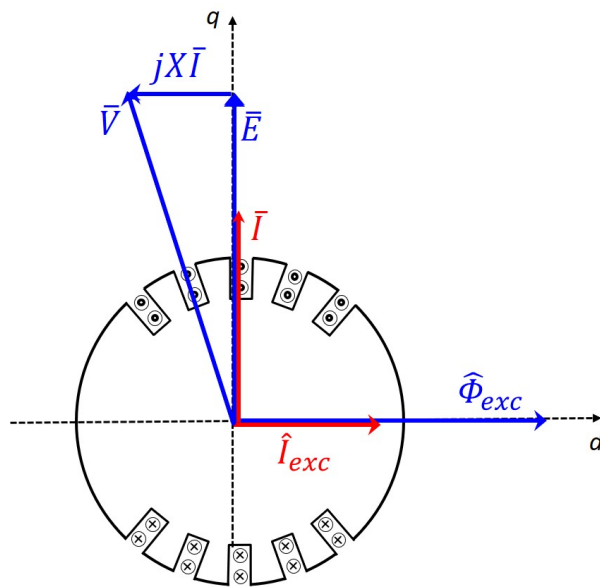


Figure 3.10: Vector diagram at load for working point 1

Where the  $X$  is the reactance of the cylindrical machine, assuming it perfectly isotropic. For what concerns the rotor current, an adaptation should be made since the two rotor configurations do not have the same number of excitation turns. By the way, the difference is of only one turn per pole between the two model. For this reason, from now on the comparison of the two machines is made by keeping the same excitation current. Therefore, supplying the machine as suggested by Table 2.5, the resulting average torque is:

$$T = 94.2 \text{ Nm} \quad (3.23)$$

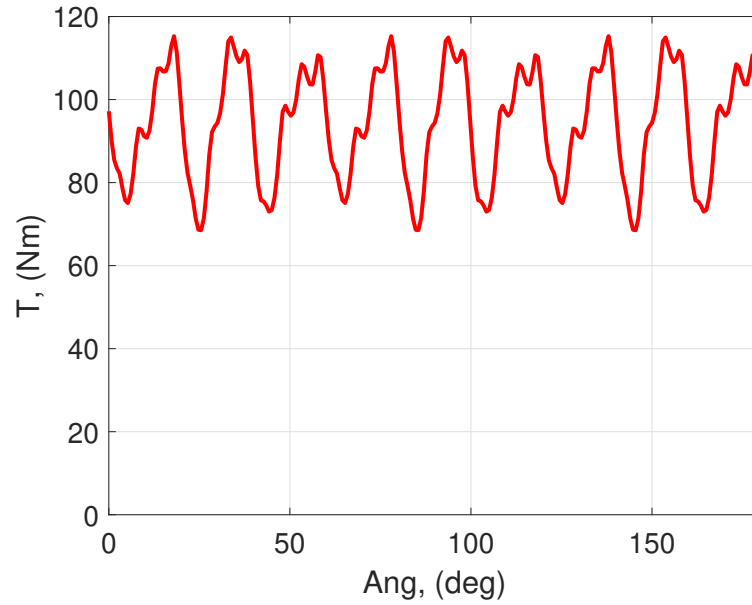


Figure 3.11: Obtained torque from FEM simulations for the working point 1.

In the following figure, the color shade chart of the magnetic flux density is presented, where the armature reaction is clearly visible. A comparison of the two machine is proposed in Chapter 4.

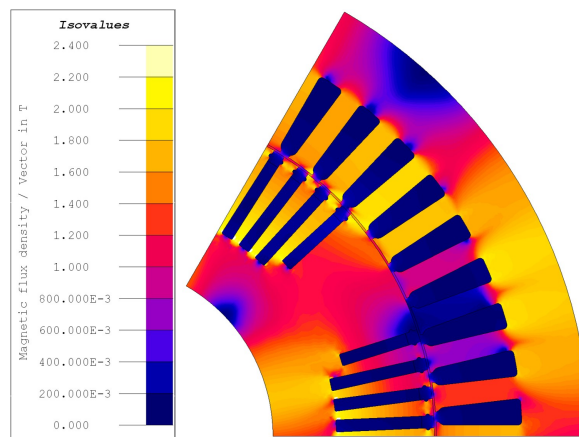


Figure 3.12: Magnetic flux density color shade chart of the cylindrical rotor for the working point 1.

## 3.5 Main Parameters Computation

Since the stator of the two machine is exactly the same, the stator resistance as well as the leakage inductance are already known. The parameters that need to be computed are instead the rotor resistance and the inductance of the machine.

### 3.5.1 Analytical Computation

#### Rotor Resistance

The previously computed values of the surface of one conductor and of the number of rotor turns per pole are used to compute the rotor resistance. For what concerns the length of turns, four different end windings are considered. Since the rotor turns are concentric, one different distance is considered for each couple of slots.

For each end winding the same end winding factor is used. It is actually impossible to physically realize it. Each one of them should have its own coefficient. By the way, in order to obtain a realistic value of the rotor resistance, it does not differ if the same value is used. Therefore, the total length the final expression of the rotor resistance is:

$$R'_r = 4p \cdot [(3 \cdot L + k_{ew} \cdot (D_{ew,1} + D_{ew,2} + D_{ew,3})) \cdot N_{r,ls} + (L + D_{ew,4} \cdot k_{ew}) \cdot N_{r,ls}] \cdot \frac{\rho}{S'_r} \quad (3.24)$$

$$R'_r = 275 \Omega \quad @20^\circ\text{C} \quad (3.25)$$

#### Magnetizing Inductance

A cylindrical rotor machine is approximately isotropic, since the uniformity of the air gap is disturbed only by the stator and rotor slots. The slots in the rotor are placed regularly on its periphery. As previously seen, normally two-thirds of the rotor surface is equipped with slots. This introduces a magnetic anisotropy also in cylindrical machine. Nevertheless, the air gap can be considered equal in all directions.

$$\delta_d \approx \delta_q \approx \delta_0 \cdot k_c \cdot k_{cr} \quad (3.26)$$

In view of the fact that, both stator and rotor are slotted, the Carter factor is applied twice. The value of the stator Carter factor is the one used in the salient pole machine, since the stator is not changed. While the rotor Carter factor is obtained by imagining the rotor all slotted.

$$k_{cr} = \frac{\frac{\tau_{rs}}{SW}}{\frac{\tau_{rs}}{SW} - \frac{\frac{SW}{\delta_0}}{5 + \frac{SW}{\delta_0}}} = 1.3 \quad (3.27)$$

Because of the isotropy of the machine, here only a single magnetizing inductance is computed, even though the slots in the rotor makes the inductance in the quadrature axis slightly smaller. To compute the magnetizing inductance, the air gap showed in equation (3.26) is used in the the formula employed for the salient pole machine (2.51). The obtained value is:

$$L_m = 1.42 \text{ mH} \quad (3.28)$$

Then the total inductance can be computed by adding the leakage inductance:

$$L_d = L_q = 1.46 \text{ mH} \quad (3.29)$$

### 3.5.2 Computation by Simulation of the Inductances

Again, by means of some simulations the values of the inductance is confirmed. To reach the goal, the stator is supplied with different current values  $\hat{I}$ , once in the direct direction and once in the quadrature one, in order to find  $L_d$  and  $L_q$ . Indeed, it is expected to find an even more evident difference between the two values in comparison to what affirmed about synchronous generators, since here the rotor slots dimensions are bigger if compared to the dimensions of the whole machine. The chosen values of the current must avoid to cause the saturation of the machine, since the value of the inductance would be compromised. The same values of the salient pole machine are selected and simulated.

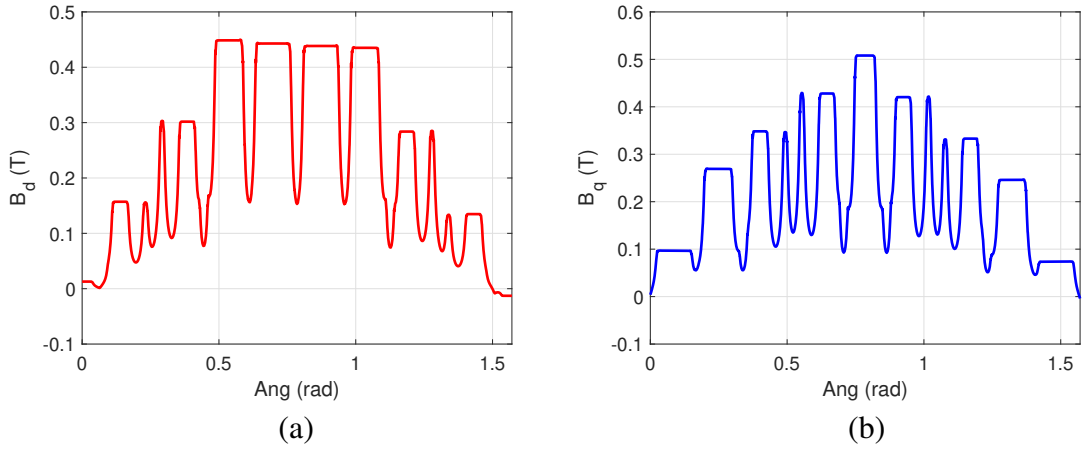


Figure 3.13: Magnetic flux density for a stator current vector of 30 A placed in d-axis (a) and q-axis (b)

Here, half of the simulated currents are shown, for sake of simplicity.

$\hat{I}$ , (A)	10	20	30	40	50	60	70
$\hat{B}_d$ , (T)	0.12	0.24	0.37	0.49	0.61	0.73	0.82
$\hat{B}_q$ , (T)	0.1	0.21	0.32	0.43	0.52	0.60	0.66
$\hat{B}_q/\hat{B}_d$	0.88	0.87	0.87	0.86	0.85	0.82	0.81

Table 3.1: Values of fundamentals of the magnetic flux density in the air gap for different stator currents in the cylindrical rotor machine.

As it can be seen from the third row, the ratio of the fundamental peak of the magnetic flux density in the two directions is not equals to one. This ratio is also the ratio that occurs between the two inductances. Therefore, there actually is a difference between the two parameters  $L_d$  and  $L_q$ , but always less than the one of the salient pole machine.

Finally, by means of the magnetic flux density obtained from each simulation (consistently with the chosen direction of the current), the two inductances are computed as follows:

$$L_d = \frac{2}{\pi} \cdot \frac{k_w \cdot N_s \cdot \tau \cdot L_p \cdot \hat{B}_d}{\hat{I}} \quad (3.30)$$

$$L_q = \frac{2}{\pi} \cdot \frac{k_w \cdot N_s \cdot \tau \cdot L_p \cdot \hat{B}_q}{\hat{I}} \quad (3.31)$$

By averaging the results for each direction, the two inductances are:

$$L_d = 1.60 \text{ mH} \quad (3.32)$$

$$L_q = 1.37 \text{ mH} \quad (3.33)$$

Here, a bigger error occurs on the analytical computation of the parameters. This could be due to two different reasons. First of all, an approximation is made on the rotor Carter factor when considering the whole geometry slotted. This means that a bigger equivalent air gap length is considered, resulting in a lower value of the inductance in comparison to  $L_d$  obtained from simulations. Plus, no anisotropy is taken into account in the analytical computation. This explains also the difference in the value of  $L_q$ .

### 3.6 Losses and Efficiencies

In section 2.7, the supply technique issue of the salient pole machine has been discussed, by assuming to feed the motor with the values of  $I_q$ ,  $I_d$  and  $I_{exc}$  provided by the thesis [25]. On the contrary, at this point of the investigation it is still unknown how to correctly supply the cylindrical rotor machine in order to reproduce the feeding conditions of the salient pole motor. As already mentioned, one of the goal in the salient pole machine supply strategy is to have a high power factor, other than reaching the desired torques and speeds. Then the same criteria should be applied when feeding the cylindrical rotor. Assuming the machine to be perfectly isotropic, the vector diagram at load is showed in the following figure.

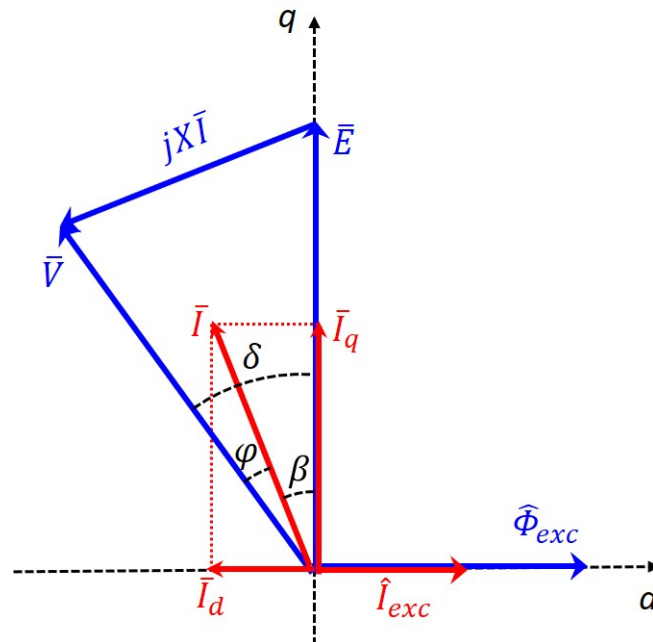


Figure 3.14: Vector diagram at load of the cylindrical rotor machine.

Here, the current vector is placed in the second quadrant as well as for the salient pole motor. The smaller is the angle  $\varphi$  the higher is the power factor. With this basic principle in mind, different combinations of the three currents are considered in order to reach comparable torques and power factors, for the same speed. Nevertheless, since this is a long procedure to accomplish, this is done only for one working point. Among the six working points simulated for the salient pole motor, the WPC is reasonably one of the most crucial and representative. Then only for this point, the currents are computed and the simulation is

run. The values of the currents are reported in the following table.

	WPC
$I_d$ , (A)	-110
$I_q$ , (A)	190
$I_{exc}$ , (A)	1.70
$n$ , (rpm)	4000
$R_r$ , ( $\Omega$ ) @70°C	329.3

Figure 3.15: Supplying conditions for WPC in the cylindrical motor.

Feeding the cylindrical rotor with these currents allows to get the following results.

	WPC
TORQUE, (Nm)	134
PEAK VOLTAGE, (V)	189
$\cos(\phi)$	0.92

Figure 3.16: Obtained results for WPC in the cylindrical rotor machine.

It is worthy to point out again that this feeding condition is not necessary the best one for the motor, and that different combinations of  $I_q$ ,  $I_d$  and  $I_{exc}$  can produce the same torque and power factor. Plus, both the machines reach high values of the magnetic flux density for some working points, resulting in the impossibility of using the computed linear parameters to have a reliable model of them. The only possible way to find the optimal triplets of current values is by mapping the motor, as in the work proposed in [30] suggests.

### Efficiency Computation

The efficiency of the cylindrical rotor for the working point C is computed exactly how explained for the salient pole rotor. Again, the iron losses computation is made thought the Bertotti method using the same coefficients of the salient pole machine, since the employed material is the same. Moreover, when computing the rotor Joule losses, the resistance of

the coil has to be correctly considered as the one computed in section 3.5. Finally, the mechanical losses are considered the same for the two machines.

In these conditions, the efficiency of the motor for the only simulated working point is:

$$\eta = 95.3\% \quad (3.34)$$

# Chapter 4

## Comparison

### 4.1 Comparison at No-Load

In this chapter an overall overview of the two machines is proposed, and the final comparison is carried out. First of all, the performances of the two motors are compared in terms of no-load performances. In this condition only the rotor is fed, while the stator winding is left open. For the same speed (2000 rpm) and for the same range of excitation currents, the two no-load characteristics have been previously computed and here they are plotted in the same graph 4.1.

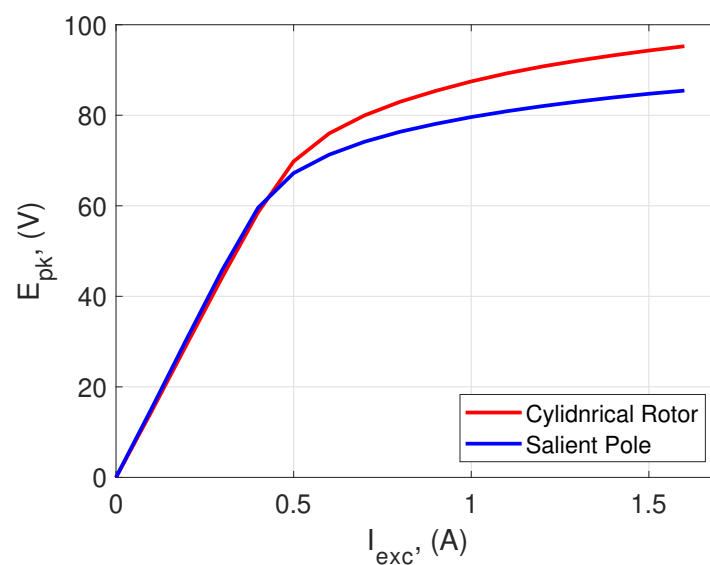


Figure 4.1: No-load characteristics comparison of the salient pole machine and the cylindrical rotor machine for  $n = 2000$  rpm.

Therefore, it can be deduced that in linear conditions the peak of the fundamental of the back electromotive force is basically the same in the two machines. On the contrary, for the same excitation current the cylindrical rotor reaches a higher back electromotive force in the saturation region. Indeed, when representing the color shaded magnetic flux density chart it is visible that the cylindrical rotor is less affected by saturation, as shown in Figure 4.2. This is obtained by setting the same rotational speed (2000 rpm) and an excitation current great enough to make the machine work in the saturation region ( $I_{exc} = 1$  A).

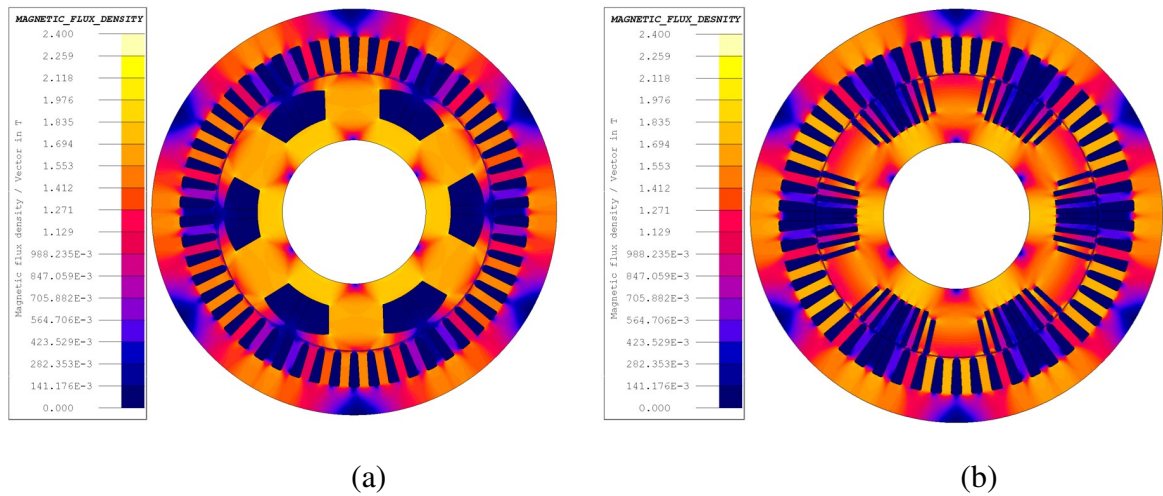


Figure 4.2: Magnetic flux density at no load comparison at 2000 rpm and  $I_{exc} = 1$  A: (a) salient pole and (b) cylindrical rotor.

Here, the obtained voltages at no load for two different excitation currents, (0.2 A and 1.6 A) are plotted.

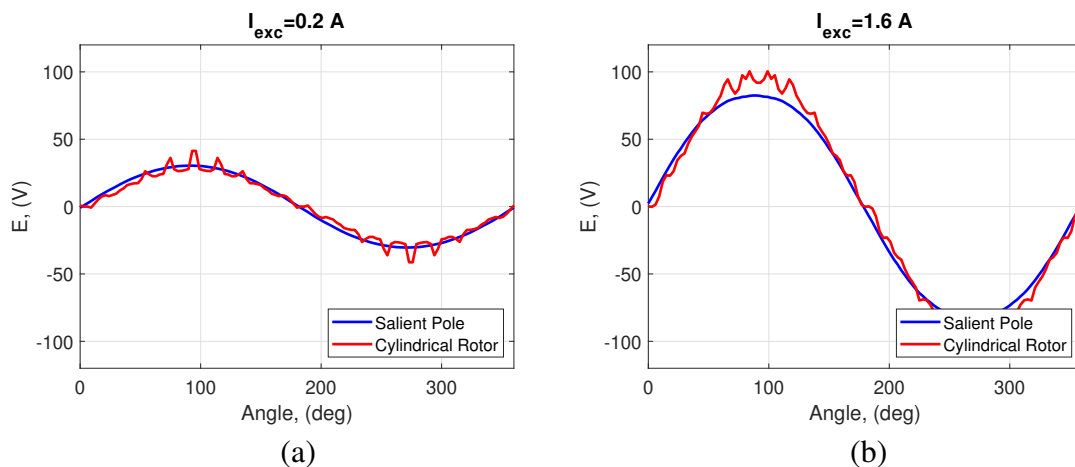


Figure 4.3: No-load voltages for  $I_{exc} = 0.2$  A (a) and for  $I_{exc} = 1.6$  A (b) for the salient pole machine and the cylindrical rotor machine.

Again, it is confirmed the different behaviour of the two machines when passing from the linear region (a) to the saturation region (b) of the no-load characteristic. Anyway, what can be deduced from Figure 4.3 is that the designed cylindrical rotor machine has a worse no-load voltage than the salient pole machine. This is due to the presence of the slots in the rotor that affect the shape of the magnetic flux density in the air gap. Therefore, a spectrum analysis of the latter is made for the two machines, for different excitation currents and always at a speed of 2000 rpm.

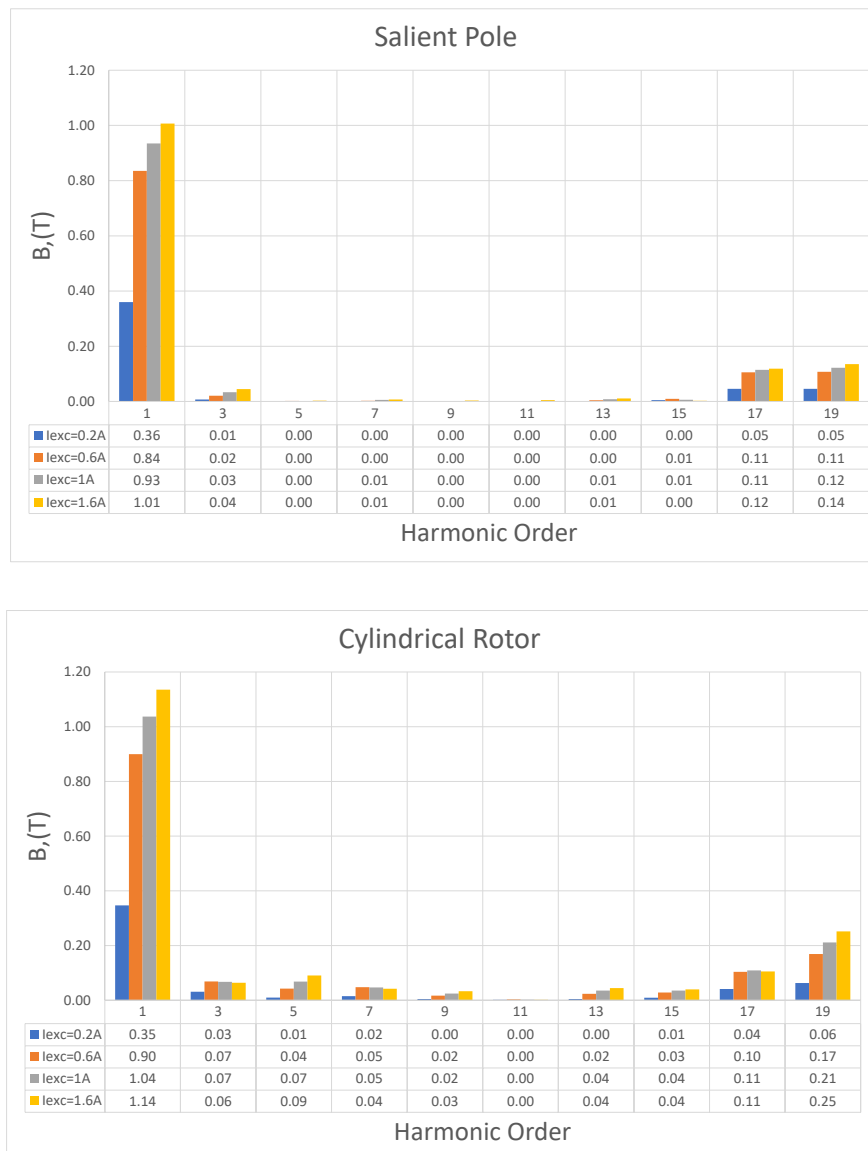


Figure 4.4: Spectrum of the magnetic flux density in the air gap for the salient pole machine and the cylindrical rotor machine for different excitation currents and at a speed of 2000 rpm.

As it can be seen, the harmonic content of the cylindrical rotor machine is higher than in the salient pole machine, but also the fundamentals for high excitation currents values, as expected. For sake of clarity, in a comparison only in terms of fundamentals is shown.

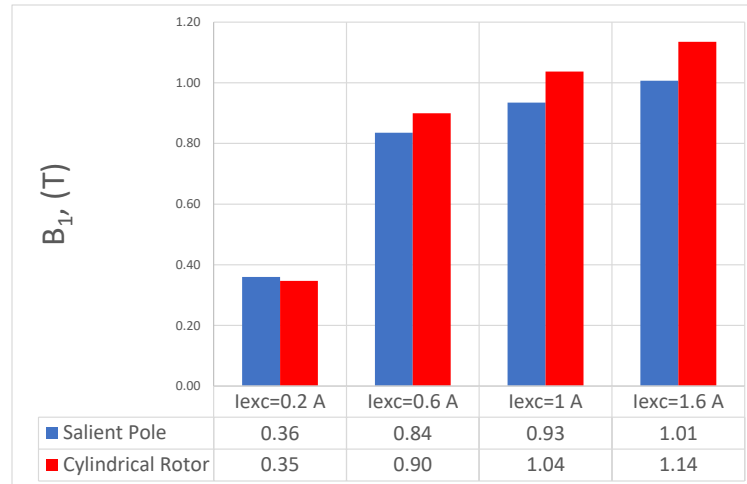


Figure 4.5: Fundamentals of the magnetic flux density in the air gap for the salient pole machine and the cylindrical rotor machine for different excitation currents and at a speed of 2000 rpm.

## 4.2 Parameters Comparison

In section 2.6 and 3.5, the main parameters of both machines have been computed. Since the stator of both machine is the same, so is the value of the stator resistance. On the contrary, the rotor resistance value varies. This is due to the different arrangement of the winding on the two rotors. Indeed, even though almost the same turns per pole are used ( $N_r = 843$  and  $N'_r = 844$ ), the length of each turn is greater in the cylindrical rotor machine, resulting in a bigger resistance.

Concerning the machine inductances, a bigger value of the inductance in the d-axis of the cylindrical rotor was awaited. Indeed, the inductance is inversely proportional to the air gap length. As in the salient pole motor, in the d-axis an equivalent bigger air gap length is present due to the pole shape, a lower value of the inductance is obtained. On the contrary, in the cylindrical rotor machine the air gap length is almost constant and equals to the minimum that can be found in the salient pole machine. Again, the air gap in the cylindrical rotor machine is not perfectly constant because of the presence of the slots, and this is the reason why also a rotor Carter factor was used in the computation of its parameters. The inductances in the q-axis are obviously different because of the different saliency of the two machines. In table 4.1, the values of the parameters obtained via simulations are recollected. The values of the resistances are reported for a temperature of 20 °C.

<i>Parameter</i>	SP	CR
$R_s$ , (m $\Omega$ )	9.2	9.2
$R_r$ , ( $\Omega$ )	142	275
$L_d$ , (mH)	1.5	1.6
$L_q$ , (mH)	0.8	1.4

Table 4.1: Parameters Comparison

### 4.3 Comparison at Load

The next step is to compare the performances of the two machines in terms of torques by means of the simulations at load. For this reason, both machine are supplied with the same excitation current and the same stator current, which is injected only in the q-axis. The chosen values for the comparison are those of the working point 1 suggested by the company. Referring to the no-load characteristics in Figure 4.1, for the same excitation current, a greater back electromotive force is reached by the cylindrical rotor machine. This means that also a greater magnetic flux at no load is developed, hence a higher value of the linkage flux in the d-direction is awaited. In a general feeding condition, the instantaneous value of the torque can be computed by means of the fluxes and the currents in d- an q-direction, by means of equation (2.61), here rewritten.

$$T = \frac{3}{2} \cdot p \cdot (\lambda_d \cdot i_q - \lambda_q \cdot i_d) \quad (4.1)$$

This means that when only the component in the q-axis is used to supply the stator, the torque can be computed as:

$$T = \frac{3}{2} \cdot p \cdot (\lambda_d \cdot i_q) \quad (4.2)$$

Based on this, since current in the d-direction is zero and that in the q-direction is the same for both machines, the torque is expected to be higher in the cylindrical rotor machine if a higher value of the d-axis linkage flux is developed. Despite of this, the two obtained torques are showed in Figure 4.6. The average values of the torques are:

$$T_{SP} = 112 \text{ Nm} \quad (4.3)$$

$$T_{CR} = 94 \text{ Nm} \quad (4.4)$$

Fist of all, a bigger torque ripple occurs in the cylindrical rotor. Again, this is due the harmonic content of the magnetic flux density because of the presence the rotor slots. It is important to bear in mind that the design of the cylindrical rotor is not optimized and

that different solutions can be adopted to overcome the issue, such as to skew the machine. However, a lower value of the torque is provided by the cylindrical rotor, in disagreement to what previously said.

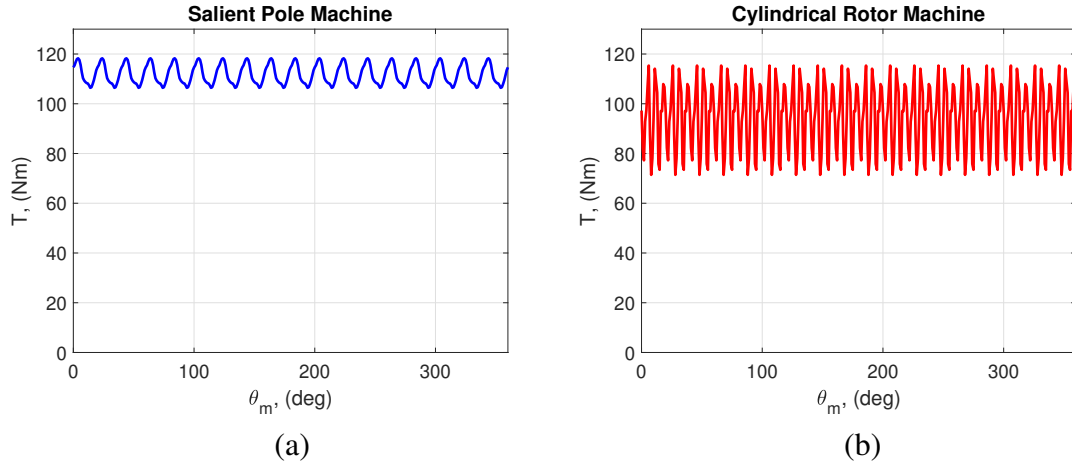


Figure 4.6: Torque comparison for  $I_{exc} = 1$  A,  $I_q = 246$  A and  $I_d = 0$  A of the salient pole machine (a) and of the cylindrical rotor machine (b).

The reason has been investigated and finally correlated to a more pronounced cross saturation phenomenon in the cylindrical rotor machine, as analysed in the following section.

### 4.3.1 Cross Saturation Effect

The cross saturation is the saturation of portion of magnetic circuit associated to the d-axis caused by the current of the q-axis and vice versa.

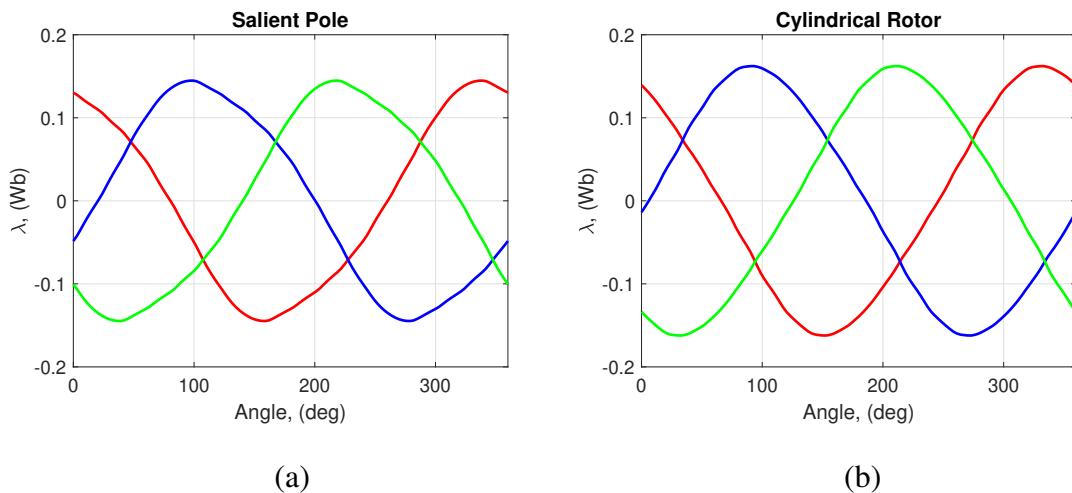


Figure 4.7: Linkage fluxes in salient pole (a) and cylindrical rotor (b).

To find an explanation of the lower torque provided by the cylindrical rotor machine, the linkage fluxes are computed by means of FLUX for the simulated WP1. The values extrapolated from the finite element simulations are the linkage fluxes of the three coils, which are shown in Figure 4.7. To correctly employ formula (4.2), the components of the fluxes in (d,q) frame need to be obtained. Therefore, the three-phase fluxes are translated from the three-phase reference frame to the two-axis orthogonal stationary reference frame  $(\alpha, \beta)$  by means of the Clarke transformation.

$$\begin{bmatrix} \lambda_\alpha \\ \lambda_\beta \\ \lambda_o \end{bmatrix} = \begin{bmatrix} \frac{2}{3} & -\frac{1}{3} & -\frac{1}{3} \\ 0 & \frac{\sqrt{3}}{3} & -\frac{\sqrt{3}}{3} \\ 1 & 1 & 1 \end{bmatrix} \cdot \begin{bmatrix} \lambda_a \\ \lambda_b \\ \lambda_c \end{bmatrix} \quad (4.5)$$

Subsequently, the two-axis orthogonal stationary reference frame fluxes are transformed into rotating frame fluxes using Park transformation.

$$\begin{bmatrix} \lambda_\alpha \\ \lambda_\beta \end{bmatrix} = \begin{bmatrix} \cos(\theta_e + \theta_i) & \sin(\theta_e + \theta_i) \\ -\sin(\theta_e + \theta_i) & \cos(\theta_e + \theta_i) \end{bmatrix} \cdot \begin{bmatrix} \lambda_d \\ \lambda_q \end{bmatrix} \quad (4.6)$$

This procedure is applied for both machines and the values of the fluxes in d- and q- directions are computed. The results are showed in the following table.

	<i>Salient Pole</i>	<i>Cylindrical Rotor</i>
$\lambda_d$ , (Wb)	0.101	0.085
$\lambda_q$ , (Wb)	0.098	0.132

Table 4.2: Linkage fluxes in (d,q) frame for the salient pole motor and cylindrical rotor motor

Since in WP1, the d-component of the current vector is equals to zero , then according to equation (4.2), only  $\lambda_d$  is important when the torque has to be computed. Hence, it is clear that the torque provided by the salient pole motor is greater than that of the cylindrical rotor.

As the exact same value of the current in q-direction is given, but a lower value of the flux in q-axis is obtained in the cylindrical motor, this means that the current in q-direction is

affecting the flux in d-direction, i.e. a stronger cross saturation effect can be detected in the cylindrical rotor. The cause of this phenomenon can be deeper investigated by looking at the magnetic field lines distribution when injecting current only in d-direction or q-direction. If a similar arrangement of the magnetic field lines can be observed when injecting current only in the d-axis (see (a) and (c) in Figure 4.8), a completely different situation occurs when the current vector lies in the q-direction (see (b) and (d) in Figure 4.8). This is due to geometries of the two machine, that are relatively similar when looking at the machines by moving along the radial direction but also different when moving on the perpendicular direction. Indeed the presence of the teeth in the rotor creates a favourable path for the magnetic field lines.

The consequence is that the cylindrical rotor machine is strongly penalized when compared to its counterpart. Indeed, these machines are meant to work at high values of magnetic flux density which enhance the effect of this phenomenon.

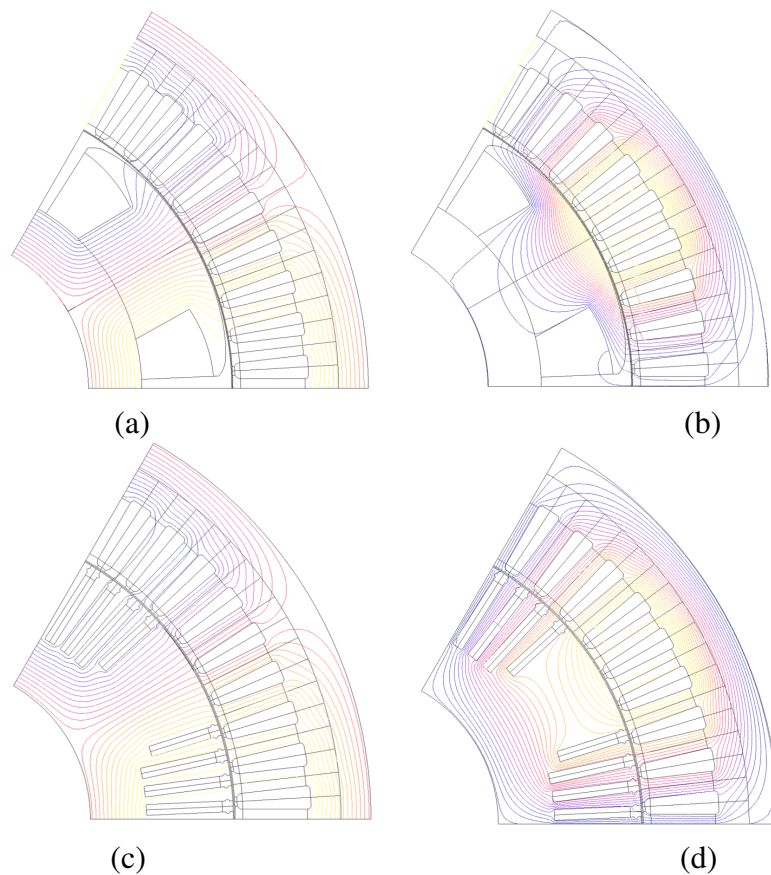


Figure 4.8: Magnetic field lines with stator current in d- and q-axis in salient pole respectively (a) and (b) and in cylindrical rotor (c) and (d).

### 4.3.2 Torques Comparison

In order to compare the performances of the two machines, an analysis of the output torques is made for different values of excitation current, magnitude and phase of the stator current vector, the latter being taken with the convention showed in the following figure.

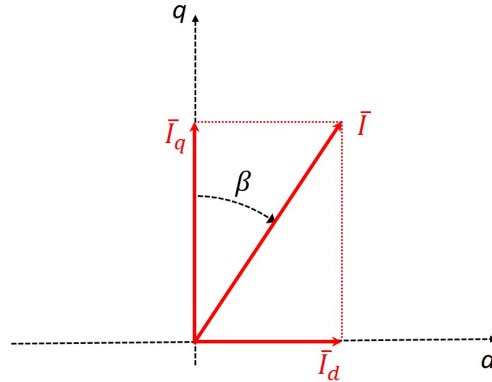
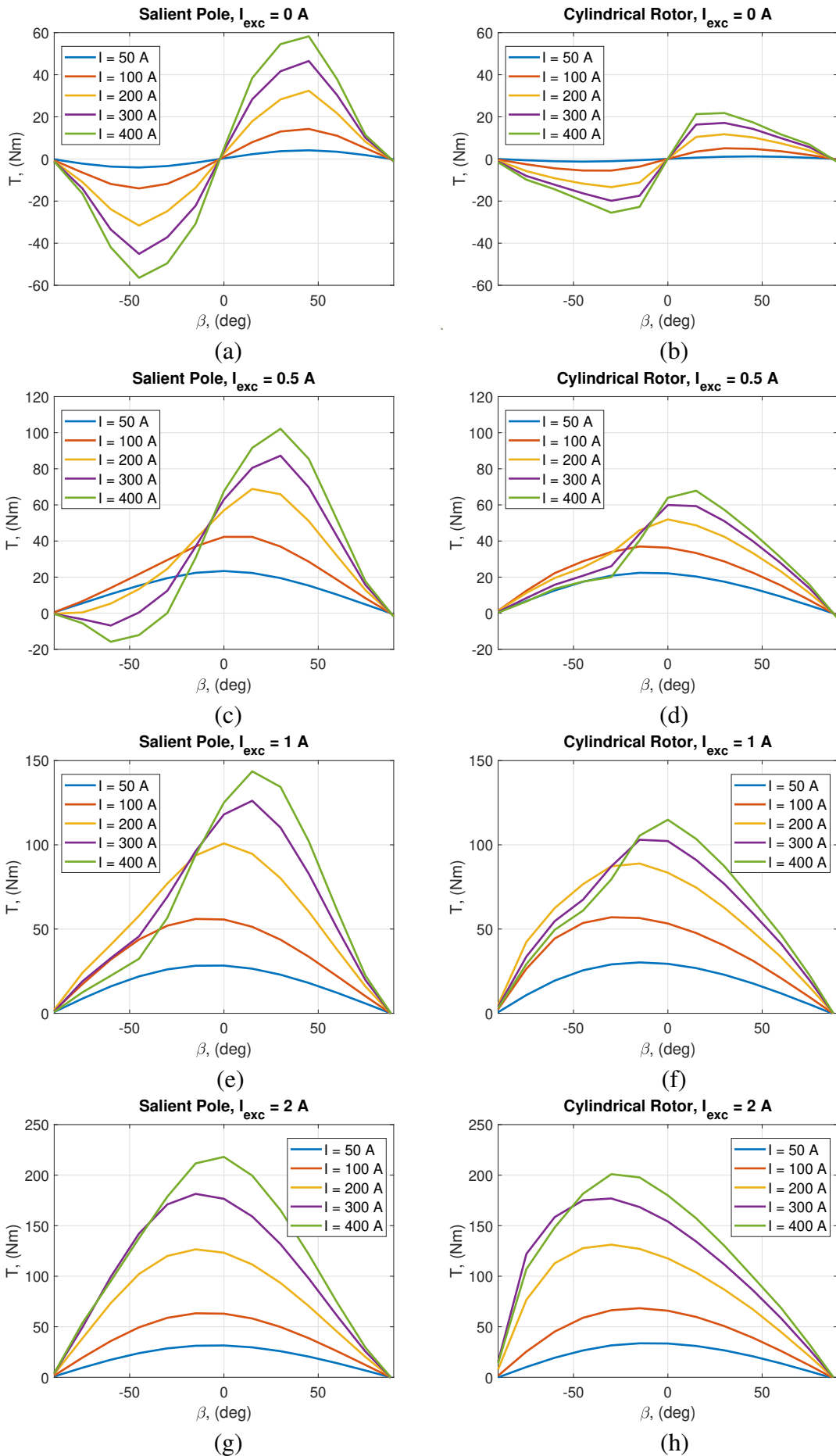


Figure 4.9: Reference for the angle  $\beta$  for the torque comparison.

The excitation current varies from 0 to 3 A, the stator current vector magnitude from 50 A to 400 A and the angle from  $-90^\circ$  to  $90^\circ$ . These values are reasonable taken by looking at the tables in Figure 2.32. For each combination of these, the average value of the torque is computed and, in Figure 4.10, it is shown in function of the angle  $\beta$ , for both machines. In figures (a) and (b), the torques for an excitation current equals to zero are plotted. When the rotor is not powered, the torque is only given by the second addendum of equation (2.26), being  $E = 0$ . Indeed in this condition, the machine torque is given only by the different reluctances in the two axes. Thus, the torque of the salient pole machine is necessarily higher than the one provided by the cylindrical rotor. Moreover, if the cylindrical rotor was perfectly isotropic, the absence of the excitation current would inevitably imply also the absence of the torque. Nevertheless, the little saliency of the cylindrical motor showed by the difference of the  $L_d$  and  $L_q$ , it is confirmed by the presence of the torque. On the contrary, for high values of the excitation current the gap between the salient pole and the cylindrical rotor torques tends to be less pronounced.



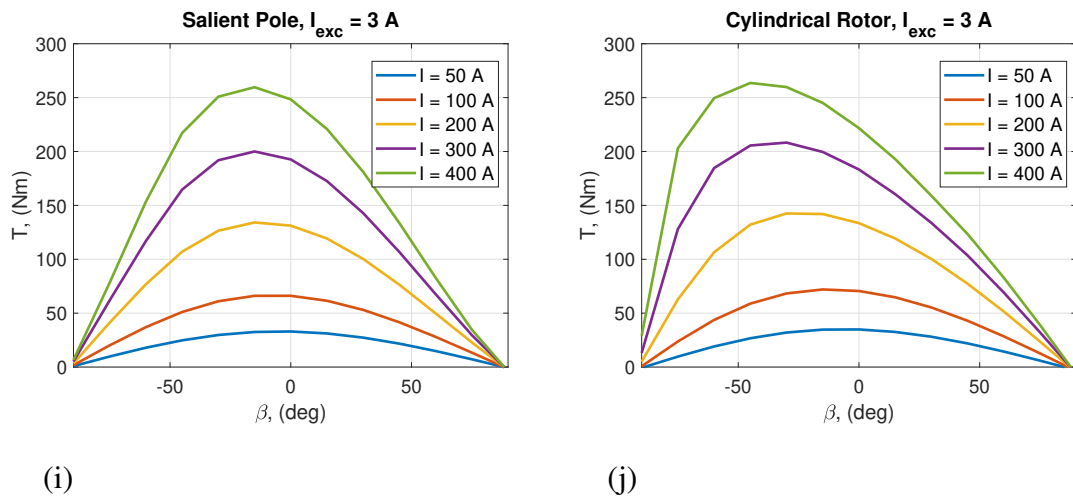


Figure 4.10: Salient pole machine and cylindrical rotor output torque obtained by FEM in functions of the stator current vector angle and amplitude for different excitation currents.

## 4.4 Losses and Efficiencies Comparison

The last comparison of the two machine is made in terms of efficiencies. As previously said, in the work proposed in [25], the supply strategy of the salient pole machine aims to maximize the power factor, other than reaching the desired torque and speed, respecting the voltage limits. While, as stated in section 3.6, the efficiency of only one working point has been computed. The identification of the supply strategy needed to reach the same goals of the salient pole machine, exceeds the goal of this thesis but it might be the object of future works. Hence, at present different combinations of  $i_q$ ,  $i_d$  and  $i_{exc}$  have been considered to simulate the working point C of Figure 2.35. The employed values are shown in the following table, and compared to the supplying conditions of the salient pole machine.

	<i>SP</i>	<i>CR</i>
$I_d$ , (A)	-28	-110
$I_q$ , (A)	231	190
$I$ , (A)	233	220
$I_{exc}$ , (A)	1.5	1.7
$n$ , (rpm)	4000	4000
$R_r$ , ( $\Omega$ ) @70 °C	170	329

Table 4.3: Supplying conditions of the salient pole machine and the cylindrical rotor machine for working point C of Figure 2.35.

Simulations results are shown in the following table.

	<i>SP</i>	<i>CR</i>
$T$ , (Nm)	134	134
$\cos \varphi$ , (A)	0.9	0.92
$V_{pk}$ , (V)	183	189

Table 4.4: Obtained results of the salient pole machine and the cylindrical rotor machine for working point C of Figure 2.35.

Moreover the magnetic flux density map of both machines is obtained and reported in

Figure 4.11. As previously said, it is confirmed that these machines are meant to work at high values of magnetic flux density. Indeed, by looking at the torque-speed characteristic in Figure 2.35, it can be seen that the simulated point is not one of the most challenging for the motors, on the contrary the highest efficiencies are reached in that area.

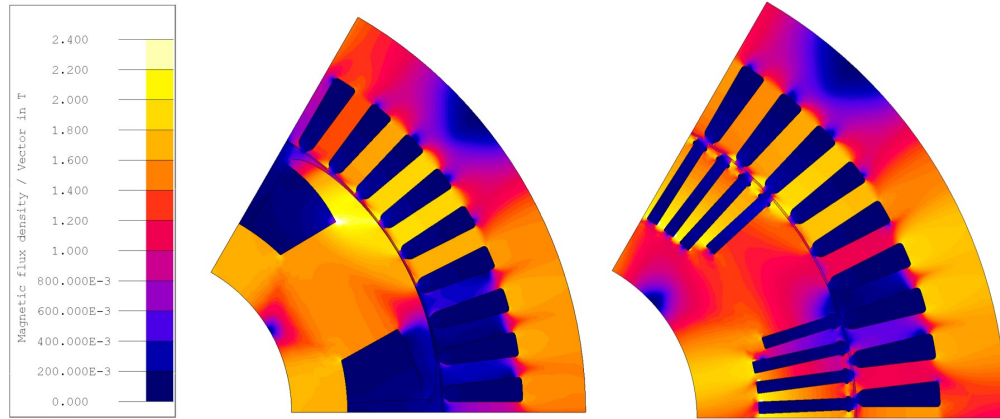


Figure 4.11: Comparison of the magnetic flux density of the salient pole machine and the cylindrical rotor machine for working point C of Figure 2.35.

Finally, the efficiency of the cylindrical motor is computed as described in section 2.7, and compared to that of the salient pole machine.

$$\eta_{SP} = 96.6\% \quad (4.7)$$

$$\eta_{CR} = 95.3\% \quad (4.8)$$

As it can be seen, comparable values are obtained.

# Chapter 5

## Conclusions and Future Work

### 5.1 Conclusions

A comparative analysis of a salient pole motor and a cylindrical rotor motor for traction applications has been carried out in terms of performances. An already existing salient pole prototype for electric traction has been used as the baseline of the study. A preliminary sizing of the cylindrical rotor machine has been accomplished, by keeping the same stator of the salient pole machine and respecting electromagnetic constraints. The comparison has been accomplished by analytical evaluations and FEM 2D simulations. Results have shown that the salient pole motor seems to achieve slightly better performances, especially for low values of the excitation current. This is due to the lack of anisotropy and a more marked cross effect saturation of the cylindrical rotor with respect to the salient pole. On the contrary, as the excitation current increases the gap tends to be less pronounced. Moreover, a bigger torque ripple can be found in the cylindrical rotor machine due to the presence of the rotor slots. Considering that the design of the cylindrical rotor is not optimized, better performances with respect to the salient pole might be accomplished with further improvements both from the electromagnetic design and supply strategy points of view. In conclusion, if the cylindrical rotor represents an undeniable beneficial choice from a mechanical point of view, deeper investigation is needed to make it electromagnetically competitive with its counterpart.

## 5.2 Future Work

In this section, some possible and useful future works are presented. First of all, a fair comparison in terms of efficiencies of the two machine is needed for different and significant working points. The comparison must be held with the aim of getting the same torques and speeds of the salient pole machine, while keeping the same power factor. Indeed, as this has been the supply strategy adopted to obtain the efficiency map of the salient pole motor, it is necessary to reproduce these conditions also in the cylindrical rotor machine. Consequently, a mapping of the cylindrical rotor machine is mandatory to accomplish the goal and it should be included in future works.

Moreover, the constraint of keeping the same stator is not probably the most fortunate solution for the design of the cylindrical rotor machine. In turbogeneratos, cylindrical rotors are usually 2- or 4-poles machines. Here, the number of poles is equal to six since it was already imposed by the salient pole machine. The consequence has been a reduced space in the rotor periphery for each pole, and consequently a low number of rotor slots. This has worsened the harmonic content of the air gap flux density of the cylindrical rotor machine with respect to the salient pole machine, resulting in a bigger torque ripple. Therefore a possible solution to this issue may be to totally redesign the machine, by keeping mechanical and electromagnetic constraints of the salient pole machine, but changing the geometry. In any case, the design must consider not to excessively exceeds the volume and the weight of the salient pole machine, as this is a crucial point when it comes to electric traction motor design.

Otherwise, if the same number of pole is kept, a solution to the torque ripple could be to skew the machine. Some basic computations have been made in order to evaluate the output torque of the eventually skewed cylindrical rotor machine, and the results are shown in Figure 5.1. The showed torques have been computed for  $I_{exc} = 1$  A,  $I_q = 246$  A and  $I_d = 0$  A. The obtained average torque is always the same (94.3 Nm), but the torque ripple has been reduced from 45% to 5%.

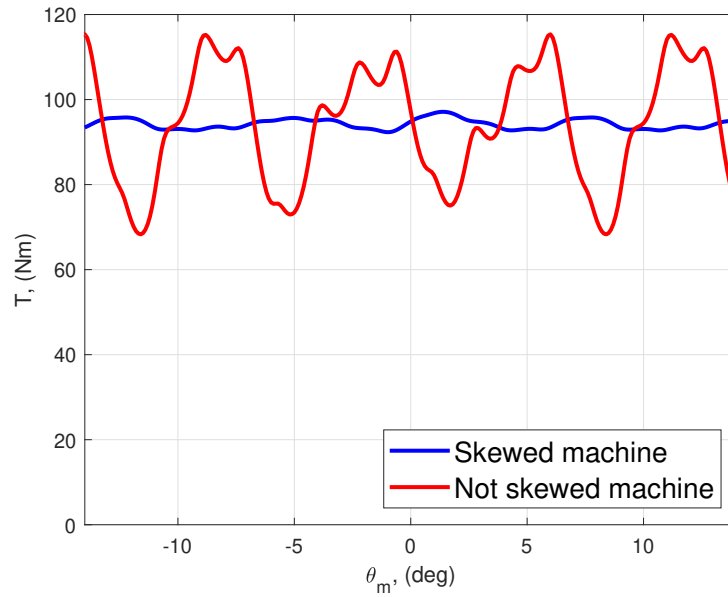


Figure 5.1: Comparison of the torque of the original cylindrical machine with a possible skewed machine.

Another possible solution is to increase the air gap length, in order to make the effect of the rotor slots on the output torque less marked. By the way, this would inevitably imply a lower average output torque. Furthermore, a shortened pitch could be part of future investigation to overcome the issue.

# Bibliography

- [1] Z. Rahman, M. Ehsani, and K. Butler, “An investigation of electric motor drive characteristics for ev and hev propulsion systems,” Tech. Rep. SAE Technical Paper Series pp. 2000-01-3062.
- [2] M. Ehsani, K. M. Rahman, and H. A. Toliyat, “Propulsion system design of electric and hybrid vehicles,” *IEEE Transactions on Industrial Electronics*, vol. 44, pp. 19–27, Feb 1997.
- [3] C. C. Chan, “The state of the art of electric and hybrid vehicles,” *Proceedings of the IEEE*, vol. 90, pp. 247–275, Feb 2002.
- [4] M. Zeraoulia, M. Benbouzid, and D. Diallo, “Electric motor drive selection issues for hev propulsion systems: A comparative study,” *Vehicular Technology, IEEE Transactions on*, vol. 55, pp. 1756 – 1764, 12 2006.
- [5] Y. A. Alamoudi, A. Ferrah, R. Panduranga, A. Althobaiti, and F. Mulolani, “State-of-the art electrical machines for modern electric vehicles,” in *2019 Advances in Science and Engineering Technology International Conferences (ASET)*, pp. 1–8, March 2019.
- [6] J. de Santiago, H. Bernhoff, B. Ekergård, S. Eriksson, S. Ferhatovic, R. Waters, and M. Leijon, “Electrical motor drivelines in commercial all-electric vehicles: A review,” *IEEE Transactions on Vehicular Technology*, vol. 61, pp. 475–484, Feb 2012.
- [7] T. Finken, M. Felden, and K. Hameyer, “Comparison and design of different electrical machine types regarding their applicability in hybrid electrical vehicles,” in *2008 18th International Conference on Electrical Machines*, pp. 1–5, Sep. 2008.

- [8] S. Williamson, M. Lukic, and A. Emadi, "Comprehensive drive train efficiency analysis of hybrid electric and fuel cell vehicles based on motor-controller efficiency modeling," *IEEE Transactions on Power Electronics*, vol. 21, pp. 730–740, May 2006.
- [9] K. Rajashekara, "Present status and future trends in electric vehicle propulsion technologies," *IEEE Journal of Emerging and Selected Topics in Power Electronics*, vol. 1, pp. 3–10, March 2013.
- [10] D. G. Dorrell, A. M. Knight, L. Evans, and M. Popescu, "Analysis and design techniques applied to hybrid vehicle drive machines—assessment of alternative ipm and induction motor topologies," *IEEE Transactions on Industrial Electronics*, vol. 59, pp. 3690–3699, Oct 2012.
- [11] A. Di Gioia, I. P. Brown, Y. Nie, R. Knippel, D. C. Ludois, J. Dai, S. Hagen, and C. Alteheld, "Design of a wound field synchronous machine for electric vehicle traction with brushless capacitive field excitation," in *2016 IEEE Energy Conversion Congress and Exposition (ECCE)*, pp. 1–8, Sep. 2016.
- [12] C. Rossi, D. Casadei, A. Pilati, and M. Marano, "Wound rotor salient pole synchronous machine drive for electric traction," in *Conference Record of the 2006 IEEE Industry Applications Conference Forty-First IAS Annual Meeting*, vol. 3, pp. 1235–1241, Oct 2006.
- [13] D. G. Dorrell, "Are wound-rotor synchronous motors suitable for use in high efficiency torque-dense automotive drives?," in *IECON 2012 - 38th Annual Conference on IEEE Industrial Electronics Society*, pp. 4880–4885, Oct 2012.
- [14] A. Frias, P. Pellerey, A. K. Lebouc, C. Chillet, V. Lanfranchi, G. Friedrich, L. Albert, and L. Humbert, "Rotor and stator shape optimization of a synchronous machine to reduce iron losses and acoustic noise," in *2012 IEEE Vehicle Power and Propulsion Conference*, pp. 98–103, Oct 2012.
- [15] C. Stancu, T. Ward, K. Rahman, R. Dawsey, and P. Savagian, "Separately excited syn-

- chronous motor with rotary transformer for hybrid vehicle application,” *IEEE Transactions on Industry Applications*, vol. PP, pp. 1–1, 09 2017.
- [16] M. Strauch, S. Dewenter, A. Binder, and K. H. Nam, “Calculation of the electromagnetic characteristics of an electrically excited synchronous motor for an ev,” in *2012 IEEE Vehicle Power and Propulsion Conference*, pp. 1086–1091, 2012.
- [17] H. Park and M. Lim, “Design of high power density and high efficiency wound-field synchronous motor for electric vehicle traction,” *IEEE Access*, vol. 7, pp. 46677–46685, 2019.
- [18] M. Kostenko and L. Piotrovsky, *Electrical Machines*, vol. 2, p. 21. MIR Publishers, 1969.
- [19] D. Duricic, Z. E. Khawly, D. Loos, M. Bauer, and A. Mayr, “Rotor for an electrical machine with push-on windings,” May 24 2018.
- [20] C. Stancu, T. Ward, K. Rahman, R. Dawsey, and P. Savagian, “Separately excited synchronous motor with rotary transformer for hybrid vehicle application,” in *2014 IEEE Energy Conversion Congress and Exposition (ECCE)*, pp. 5844–5851, Sep. 2014.
- [21] H. Krupp and A. Mertens, “Rotary transformer design for brushless electrically excited synchronous machines,” in *2015 IEEE Vehicle Power and Propulsion Conference (VPPC)*, pp. 1–6, Oct 2015.
- [22] D. C. Ludois, J. K. Reed, and K. Hanson, “Capacitive power transfer for rotor field current in synchronous machines,” *IEEE Transactions on Power Electronics*, vol. 27, pp. 4638–4645, Nov 2012.
- [23] F. Yao, Q. An, X. Gao, L. Sun, and T. A. Lipo, “Principle of operation and performance of a synchronous machine employing a new harmonic excitation scheme,” *IEEE Transactions on Industry Applications*, vol. 51, pp. 3890–3898, Sep. 2015.
- [24] F. Yao, D. Sun, L. Sun, and T. A. Lipo, “Dual third-harmonic-current excitation principle of a brushless synchronous machine based on double three-phase armature wind-

- ings,” in *2019 22nd International Conference on Electrical Machines and Systems (ICEMS)*, pp. 1–4, Aug 2019.
- [25] E. M. Illiano, “Design of a highly efficient brushless current excited synchronous motor for automotive purposes,” *Doctoral Thesis*, 2014.
- [26] G. Someda, *Costruzione delle macchine elettriche*, pp. 189–190. Riccardo Patron, 1950.
- [27] V. H. Juha Pyrhönen, Tapani Jokinen, *Design of Rotating Electrical Machines*, pp. 390–391. Wiley, 2014.
- [28] I. Boldea, *Synchronous Generators*, vol. Second Edition, pp. 344–346. CRC Press, 2015.
- [29] A. Ivanov-Smolensky, *Electrical Machines*, vol. 2, pp. 229–230. MIR, 1988.
- [30] Q. Wang, H.-H. Lee, H.-J. Park, S.-I. Kim, and G.-H. Lee, “An off-line maximum torque control strategy of wound rotor synchronous machine with nonlinear parameters,” *Journal of Electrical Engineering and Technology*, vol. 11, pp. 609–617, 05 2016.